

IMAGING
ACOUSTICALLY GENERATED MICROBUBBLES WITH
ULTRASOUND

TOM H. SHORROCK

A thesis submitted to the University of London in the
Faculty of Science for the degree of Doctor of Philosophy

THE JOINT DEPARTMENT OF PHYSICS
INSTITUTE OF CANCER RESEARCH
UNIVERSITY OF LONDON

DECEMBER 2014

Climate change affects us all, but it does not affect us all equally. The poorest and most vulnerable - those who have done the least to contribute to global warming - are bearing the brunt of the impact today.

Ban Ki-Moon (Korea Herald 4.2009)

Unless we change direction, we are likely to end up where we are going.

proverb

Abstract

Microbubble contrast agents resonate at the acoustic frequencies amenable to diagnostic imaging (1-5 MHz), and the resulting acoustic response of the bubbles is typically greater than biological tissue. This enhanced acoustic response enables diagnostic ultrasound contrast imaging, for micron sized bubbles injected into the blood enhance the acoustic echo from a tissue that is otherwise echo poor. However, the use is limited to imaging the vasculature because the size of the bubble is too great to be transported across blood vessels. This greatly limits their use, precluding, for example, targeted imaging where a contrast agent is designed to have affinity to a tumour.

To lift this restriction one can either try to create a bubble *in situ* around a targeted nucleating agent, or to better control the size of a bubble within the body so that a bubble small enough to be transported can be temporarily grown to a size appropriate for imaging. This thesis investigates the simultaneous generation and imaging of sub-micron bubbles. Two acoustic waves are used, the first a low frequency (0.5 MHz) wave to generate and manipulate the bubble, the second a higher frequency (20 MHz) wave to image the generated bubble by pulse echo.

This thesis considers:

1. the nucleation of the bubble,
2. the influence of the nucleating wave on the high frequency scattering of the bubble,
3. a two wave technique to localise a bubble interacting with both waves.

These steps are first developed theoretically and are then tested experimentally. In the theoretical study it is shown that a low frequency wave can alter the response of a bubble to a higher frequency pulse and an experimental setup is suggested to maximise this effect. The lower frequency wave, the cavitating wave, pulsates the bubble and induces transitory changes in its response to a higher frequency, imaging pulse. The experimental setup investigates a cloud of bubbles - as would be found in diagnostic applications - but is disappointingly inconclusive.

The acoustically measured response of a microbubble to a sound wave is also investigated. This is done by first considering the process of acoustic measure-

ment more generally. It is found that the use of pulse-echo demands that acoustic measurement be invariant to the Lorentz group, with the sound speed being the limiting velocity. Ultrasound is a relativistic theory, and such corrections are necessary when considering the bubble wall velocities found in ultrasound contrast imaging. A Lorentz invariant model for bubble wall motion is derived that is accurate at high Mach numbers.

A second consequence is that acoustics, when measured acoustically, is an exact analogue of Maxwell's electromagnetism. Sound is a transverse wave of vorticity and Coriolis acceleration and there exists a conserved acoustic current.

CONTENTS

Contents	iv
I Introduction	1
1 Introduction	2
1.1 Ultrasound contrast using two acoustic waves	2
1.2 Thesis Outline	4
1.3 Comparison to other studies	7
II Theoretical	9
2 Bubble Nucleation	10
2.1 Introduction	10
2.2 The critical radius of a bubble	16
2.3 Question 1: A lower bound on the size of a bubble	18
2.4 Question 2: The vapourisation pressure of a perfluorocarbon droplet .	20
2.5 Question 3: The lifetime of a vapour bubble	27
2.6 Discussion	30
3 An acoustic theory of special relativity	47
3.1 Introduction	47
3.2 The acoustic definition of time and space	49
3.3 Acoustics when the measurements are made with ultrasound	58
3.4 Discussion	67
4 The pulsations of a bubble as measured with ultrasound	75
4.1 Introduction	75
4.2 The acoustically-measured Keller-Miksis model	76

4.3	Analysis of the equation	86
4.4	Discussion	93
5	Imaging a bubble influenced by a low frequency driving wave	95
5.1	Introduction	95
5.2	How the parameters influence each other	108
5.3	Exploring the whole parameter space	115
5.4	Discussion	123
III Experimental		125
6	Experimental Design	126
6.1	Introduction	126
6.2	Alignment of the two pulses	126
6.3	The source of bubbles	127
6.4	Parameters under experimental control	130
6.5	Experimental Objectives	131
6.6	Experimental Protocol	133
7	Cavitation of Water	143
7.1	Introduction	143
7.2	The excess pressure	147
7.3	Inferring the bubble size	162
7.4	Discussion	170
IV Discussion		173
8	Discussion	174
V Appendices		178
A	Tensor derivation to Maxwell's equations	179

A.1	Introduction	179
A.2	The acoustics analogue to Maxwell's relation	179
B	Classical nucleation theory	183
B.1	Introduction	183
	Bibliography	186

PREFACE

The seeing commit a strange error. They believe that we know the world only through our eyes. For my part, I discovered that the universe consists of pressure, that every object and every living being reveals itself to us by a kind of quiet yet unmistakable pressure that indicates its intention and its from.

Jacques Lusseyran^[67]

In the mid-nineteenth century Baudelaire introduced the term modernity to describe the fleeting nature of the existence in the large cities of France. For Baudelaire the task of an artist was not to just paint the cities' buildings and their people, it was equally to capture the “transitory, the fugitive, the contingent”^[8] in these cities. The artist was to portray the truth of the moment, even if that meant sacrificing the truth of the visual representation. The sociologist Michel Foucault notes in his essay, *What is enlightenment*^[29], that this marked a change in how artists viewed their role:

Baudelairean modernity is an exercise in which extreme attention to what is real is confronted with the practise of a liberty that simultaneously respects this reality and violates it.

The artist was not to eliminate their trace from their creation, but rather was to embrace the freedom that lies at the interplay between the external world and the world that the artist creates. The modern artist utilises their liberty to “imagine [the world] other than it is ... to transform it not by destroying it but by grasping in it what it is”. The artist is compelled “to face the task of producing himself”^[29].

At about the same time a similar transformation in attitude was occurring in the sciences. Henri Poincaré prefaces *Science and Hypothesis*^[85] by noting that only for the “superficial observer scientific truth is unassailable”, who retain the view that “math-

ematical truths are gained from a few self evident propositions, by a chain of flawless reasonings, ... imposed not only on us, but on Nature itself..." In contradistinction Poincaré and his contemporaries elevated the "position held by hypothesis", not only when validating a model but also in conceiving the world. Within the hypothesis an abstraction should be made that captures a kernel of truth in a particular subsystem of interactions. If idealisations have to be brought to the world to bring out this truth then so be it. In the hypothesis there is the freedom to create a picture of the world and "it was recognised that [hypothesis] is as necessary to the experimenter as it is to the mathematician".

But the scientist is a part of their picture just as much as the artist is. For their hypothesis to have meaning they must be tested against the world. To do so the scientist must define the relation their propositions have to the world by defining their systems of measurement, their notions of time and space, the location of entities within a measurable geometry. The scientist is located in the model through these definitions. And so it is here that we place the charge of Jacques Lusseyran - that the seeing believe that they know the world only through their eyes. The charge to us as individuals, that we miss much of what there is to know in the false sagacity of believing what we see, applies equally to our scientific models. The model and the world we understand as individuals is joined by the choice of measurement system.

Light is certainly the most common experimental probe, and its use was convenience by the redefinition of the metre in 1983 with reference to the speed of light^[13]. There are, however, many ways in which the world can be measured and in this thesis we use sound. One may then ask as to which propositions in science are so rooted in a system of measurement that revision should be expected when reframed in an acoustic basis. By Noether's theorem one might hope that the general principles remain the same: the conservation of energy-momentum, for instance, from the expectation that the spatio-temporal invariance of the underlying space is unaltered by the measurement system. But the actual manifestation of the phenomena must surely be different. The spatio-temporal locations of events will not in general be preserved between different notions

of time and space that are linked to respective measurement systems. The world that is seen and the world that is heard form two different pictures of the same underlying phenomenon. With Jacques Lusseyran's charge in mind, more time than is usual will be devoted to defining our notions of time and space so that they are consistent with our acoustic measure.

But the choice of measurement system is not the only place where the scientist enters their representation of the world. Science is inductive¹. Observations enable us to compare different pictures of the world, allows us to say that one is more likely than another based on a comparison of how the external world presents itself to us in a given form of measurement. While observation can provide evidence in favour or opposed to our deepest held views, our resulting conclusions are not independent of the a priori. To see this let us write the law of inference that dictates how probabilities, our beliefs of the world, should be shifted in the light of new evidence. The law of inference is Bayes Theorem and dates back to Laplace (see Jaynes^[46] for a discussion on its historical development), and has since been derived from the definition of probability^[15;100].

Bayes theorem gives how much credence should be given to a hypothesis of the world, \mathcal{H} , given a piece of experimental data, D , and an a priori view, I ,

$$P(\mathcal{H}|D, I) = \frac{P(D|\mathcal{H}, I)P(\mathcal{H}|I)}{P(D|I)}. \quad (1)$$

Our notation is that $P(a|b)$ gives the probability of proposition a given the proposition b . The comma denotes compound propositions which are always evaluated before the $|$ sign, which separates what is unknown from what is given.

In the numerator on the right-hand-side of equation 1 there are the two terms. Firstly

¹This premise is rejected by Karl Popper^[89] on his opening page: "According to the widely accepted view - to be opposed in this book - the empirical sciences can be characterised by the fact that they use 'inductive methods', as they are called". Popper, as a matter of principle, required science to be fully objective: "a subjective experience, or a feeling of conviction, can never justify a scientific statement, and that within science it can play no part except that of an object of an empirical (a psychological) enquiry." The "demand that scientific statements must be objective [means that] those statements which belong to the empirical basis of science must also be objective". That is, when this criteria of full objectivity is applied to induction infinite regress results. It is this that led Popper to reject inductive methods. (We note further that while methods such as the transformational group of Jaynes^[47] enable notions of ignorance to be defined in an objective way, ignorance is still a subjective notion in the sense used here.)

there is the probability of the data given the hypothesis and the a priori information. This gives the degree to which the experiment agrees with a model that we have dreamt up. Equally important to this, however, is the second term, the probability of the hypothesis given our a priori belief. The data from the experiment demonstrably has no influence on this term at all. Rather it gives the degree to which we believe the hypothesis, and this term is completely personal. It may be that I dislike the individual who suggests the model and that I choose to disbelieve them out of spite. This is not to reject the possibility of a scientific consensus. With sufficient quantities of data our inference goes through many iterations and the importance of our a priori beliefs diminish. To put it another way, a truly obstinate attitude is required to outweigh the validity of good models.

In the denominator of equation 1 is the probability of the data given the a priori view, and this term is a normalisation constraint so that the probability varies between 0 and 1. This normalisation does not depend on the hypothesis being made and so we are free to compare hypothesis' by simply dividing one by the other, the normalisation cancelling,

$$\frac{P(\mathcal{H}_1|D,I)}{P(\mathcal{H}_2|D,I)} = \frac{P(D|\mathcal{H}_1,I)P(\mathcal{H}_1|I)}{P(D|\mathcal{H}_2,I)P(\mathcal{H}_2|I)}. \quad (2)$$

In this way the quantitative degree to which one model should be favoured over a second is found.

From equation 2 we see that the degree of acceptance of a model is a matter for each of us as individuals, for the term $P(\mathcal{H}|I)$ does not vanish. The laws of nature are a personal matter. How we interpret the world with which we interact is a task for us each to perform. The existence of the world is assumed in our ability to collect information, D . We cannot wish away misfortune, but equally the meaning and structure of the external world is for us each to construct. We do create the world, and when we die, so does this world.

And so the scientist, through their measurement system, defines their interaction with

the world. It could be with light or with sound or by some other means. They construct a hypothesis of how their measurement system interacts with the world, and update their model based on the results and their initial views. The scientist can understand only the part of the world with which that they interact. About the rest they cannot speak. Wittgenstein^[117], after carefully detailing the hierarchy of proportions², and the inferences that can be made of them, concludes,

There is no such thing as the subject that thinks or entertains ideas.

If I wrote a book called *The world as I found it*, I should have to include a report on my body, and should have to say which parts were subordinate to my will, and which were not, etc., this being a method of isolating the subject, or rather of showing that in an important sense there is no subject; for it alone could not be mentioned in that book.

The subject does not belong to the world: rather, it is the limit of the world.

And it is in this sense that “The world and life are one, I am my world. (The microcosm)”^[117].

The scientist - as manifested in their model’s and in their inferences - has hitherto been quite a lonely creature. I look forward to the day when it is realised that the manifestation of the world is more social.

²Wittgenstein’s hierarchy of propositions shares much with the modern lattice formulation of probability theory developed by Knuth^[55;56]. For a comparison between Wittgenstein’s *Tractatus* and lattice theory see Wolniewicz^[118]

PART I

INTRODUCTION

INTRODUCTION

1.1 ULTRASOUND CONTRAST USING TWO ACOUSTIC WAVES

Ultrasound uses the *pulse-echo transit time* of a sound pulse - the time interval between the pulse being emitted and returning again - to measure the depth at which an acoustic reflection occurred. The strength of the returned signal is plotted against this depth to form an image of the echo characteristics of the material.

The echoes returned from micron sized bubbles (*microbubbles*) are stronger than from most biological structures. This is because the incident sound wave induces radial pulsations in the gas bubbles which then become acoustic sources themselves. The pulsations are resonant when insonated at diagnostic frequencies (1-10 MHz). When microbubbles are injected into a patients blood they increase the strength of the echo from a tissue-type that is otherwise echo poor. Injected microbubbles thereby act as a contrast agent for diagnostic ultrasound, and have been used in this way since 1994^[28].

The application of microbubble imaging is limited to the blood, however, by the bubble's size. The largest diameters that may be moved across endothelial cells (via *vesiculo-vacuolar transport*) are approximately 150 nm^[40], ten times smaller than the average microbubble. Other trans-cellular transport mechanisms are still more limiting, with potocytosis being able to transfer diameters of approximately 50 nm^[2;53]. Conventional microbubbles are also too large to pass through 'leaky' tumour vasculature, where gaps of between 300-600 nm can be found between endothelial cells^[30;35;40].

The development of a bubble contrast agent much smaller than 0.5 μm has not been

forthcoming. One difficulty is stability. As the bubble is shrunk the Laplace pressure within the bubble, and with it the chemical potential, grows rapidly. The bubble then equilibrates by dissolving. This effect can be mitigated by the use of an encapsulating shell^[27]. However, the difficulty then is that the resulting bubbles tend to be very stiff, and so inducing them to pulsate becomes hard^[10;11;119]. Generating stable 100 nm bubbles that can be used for ultrasound imaging has proven challenging, although there are recent signs of success^[114;119].

Since microbubbles are currently limited to the blood they do not form a good general purpose contrast agent. It is beyond the capabilities of diagnostic ultrasound to image a particular type of tissue, or to image a particular chemical environment within a tissue. To image such biological function other modalities must be used, such as functional MRI^[72], quantum dots^[6] or opto-acoustic imaging with a gold nanoparticle contrast agent^[44]. However, each of these modalities have their own short-comings, be they image resolution, time of image acquisition, invasiveness of the imaging procedure, health risks associated with the contrast agent, or cost. Ultrasound offers real-time imaging with millimetre precision in a safe, cost-effective and relatively uninvasive procedure. Its lack of functional imaging is a real loss.

There is a second problem that is caused by the lack of submicron bubbles. To attain good contrast the frequency of the ultrasound pulse should match the resonance frequency of the bubbles. This increases as the bubbles get smaller^[122]. The lack of submicron bubbles means that there is no adequate contrast agent at the micron-scale resolutions attainable by high-frequency ultrasound imaging (20-100 MHz).

The aim of this thesis is to extend the capabilities of diagnostic ultrasound by using a second acoustic wave. This wave has two roles:

1. generate a bubble in preparation of the imaging wave,
2. temporarily grow or shrink a bubble so that its resonance frequency better matched to the frequency of the imaging pulse.

The term *driving wave* will be used for the pulse that affects this control over the bubble.

The limitations of ultrasound contrast imaging are greatly reduced by being able to control the bubble in these ways. Firstly, a generated bubble can be imaged immediately and so does not have to be stable. The lifetime of a 10-100 nm bubble without a shell is between 1-100 μ s^[65], a temporal resolution that is well within the capabilities of ultrasound. Secondly, by controlling the size of the bubble, the driving wave also controls the bubble's resonance frequency. The high frequency response of conventional microbubble imaging can be extended by ensuring that the bubble is imaged when it has been transitively shrunk by the driving wave.

Two broad approaches to acoustically generate a microbubble will be considered:

1. use the reduction in pressure of the driving rarefactions to free a pocket of gas from a mote within the medium. The mote is the contrast agent in this approach.
2. vapourise an oil based contrast agent.

There are two mechanisms by which the driving wave can induce the vapourisation. The reduction in pressure in the driving rarefactions is one possibility. The heating induced by the driving wave is the other. *Acoustic Drop Vaporisation* has seen a great increase in interest in recent years^[63]. Experiments using long driving pulse trains with perfluoropenatane droplets, a perfluorocarbon with a boiling point of approximately 28°^[1], seem to favour the second explanation. It was found that the vapourisation is more easily induced at higher frequencies^[1], which is the opposite finding to what would be expected if the change was induced by a reduction in pressure. However, other groups favour the first explanation^[1757;92].

1.2 THESIS OUTLINE

The thesis is divided into IV parts. Part II contains the theoretical results of this thesis. Firstly, chapter 2 considers the acoustic generation of a bubble. The two mechanisms are analysed by asking the following questions,

1. as a function of the driving waves peak-negative pressure, what size bubble is expected to be evacuated from a mote?
2. at what pressures are submicron perfluorocarbon droplets expected to vapourise?

The motivation for the first question is the possibility of selecting a driving pressure that evacuates bubbles only in a narrow band of sizes. The driving wave could be then further be used to tune that size for a given imaging wave. The second question relies on the possibility of manufacturing oil droplets within a narrow size distribution, so that their resulting bubbles are sufficiently similar in size for a significant proportion of the bubbles to be resonant or tuned to resonance.

Classical nucleation theory is used to investigate these questions. The capillary approximation enables the critical radius of the bubble to be estimated as a function of pressure. This is the radius at which it is energetically favourable for the bubble to grow. In answer of the first question, the critical radius must be reached for entrapped gas to form a complete bubble and leave a mote. In answer of the second, the critical radius enables the energy barrier to nucleation to be calculated, from which the nucleation probability follows. By setting a threshold probability at which observing a nucleation event is deemed likely, the vaporisation pressure can be calculated. A *density functional approach* is then used to evaluate the validity of the capillary approximation used.

The rest of part II is devoted to evaluating the influence of the driving wave on the higher frequency scattering of a bubble. This is carried out in chapter 5 by using a numerical model of the pulsations of a bubble. This chapter confirms what intuition would predict, that when the driving wave compresses a large bubble towards its high-frequency resonance, or when it expands a small bubble towards the resonance, then the high frequency scatter goes up, with the expected phase change at resonance.

The high-frequency response of the bubble to the driving wave can make two wave images difficult to interpret. In particular, harmonics of the driving wave that are generated before the imaging wave is incident on the bubble break temporal ordering when

only the echo is viewed by the imaging transducer. To restore the temporal ordering a two pulse (no inversion) technique is suggested that will subtract as much of the low frequency response as possible. The result of the subtraction is the excess scatter generated in response to the imaging wave. This quantity is maximised for frequency, pressure and phase of the driving wave to estimate the ‘optimal’ parameters of the two waves.

However, there are number of steps that must be completed before the numerical model of chapter 5. Crucially, the models of a pulsating bubble that are available in the literature are inappropriate for interpreting the echoes received by ultrasound. Ultrasound, by nature of its pulse-echo technique, uses the speed of sound to define the spatio-temporal locations of entities in the world. Since it is impossible to use pulse-echo to measure an entity that is moving away at faster than the speed of sound, the sound speed is a limiting velocity. If translational invariance is also assumed, then acoustical measurements are invariant to the Lorentz group. Ultrasound measurement must, therefore, abide by this relativity that is defined in terms of the speed of sound rather than the speed of light. This theory is described in chapter 3.

There are a number of consequences to introducing an acoustic theory of relativity. Firstly, purely relativistic theories such as electromagnetism must also have an acoustic analogue. This is confirmed in chapter 3 where the full analogue is derived. The result is that the spacetime vorticity takes the role of the field tensor, the spatial vorticity takes the role of the magnetic field and the Coriolis acceleration takes the role of the electric field. These analogies have been suggested before^[31;70;102] but to the author’s knowledge this is the first time that their significance to ultrasound has been recognised.

Chapter 4 applies this acoustical theory of relativity by deriving how the pulsations of a bubble appear when imaged with ultrasound. This is achieved by deriving a Lorentz invariant version of the Keller-Miksis equation, with the differences to the original equation being explored. The Lorentz invariant Keller-Miksis equation is the model that is required to analyse the driving wave’s influence on a bubbles high frequency scattering.

Part III details the attempts at experimental verification of the results in this thesis. Experiments to generate a bubble from motes are carried out. Chapter 6 gives the scope and rationale of the experimental design. Tap water is chosen as a convenient source of motes, and the protocol for the characterising the motes is detailed.

Chapter 7 then presents the results of the experiments. The influence of the driving wave is determined by imaging the motes first with and then without the imaging pulse, the imaging technique suggested in chapter 5. The results are suggestive of the theoretical calculations of chapter 5, although more work is required to confirm the theoretical results.

Finally, chapter 8, the only chapter in part IV, reviews the progress that has been made in this thesis and proposes possible future research directions.

1.3 COMPARISON TO OTHER STUDIES

The goal of extending ultrasound contrast imaging beyond the blood is shared by a number of groups, and recently research has concentrated on the acoustic vapourisation of perfluorocarbon droplets^[1;14;17;25;32;63;92;95;98]. Kripgans^[57-59] was amongst the first to demonstrate the feasibility of the approach by using ultrasound to create large bubbles capable of occluding blood vessels. The results of Kripgans were a source of motivation and inspiration for the current work.

More recently, simultaneously and independently to this study, others have investigated the use of the perfluorodroplets as a drug delivery system: the drug being dissolved within the droplet and released upon vapourisation^[25]. Vapourisation threshold measurements for perfluoropentane have been performed by Schad^[94], and many groups have now demonstrated the vaporisation of submicron bubbles^[1;23;63;95]. Rapoport and Du^[22;92] has already had *in vivo* success with vaporised droplets for targeted drug delivery.

While there is a growing theoretical interest in the acoustic vaporisation of perfluorocarbons^[17;95;98], this thesis still differs from the literature in its theoretical stance. The

emphasis is on understanding the effect of the driving wave on the acoustic signature generated from the bubble. It is hoped that this study will be of use to those who have already taken great strides in acoustically generating bubbles, and who now wish to better understand their signals.

PART II

THEORETICAL

BUBBLE NUCLEATION

2.1 INTRODUCTION

In this chapter we investigate theoretically the use of an ultrasound pulse to generate submicron bubbles. Submicron bubbles are important because they resonate at higher frequencies, enabling imaging at higher resolutions; and because they are more likely to leave the blood than conventional micron-sized bubbles, the crucial first step towards functional diagnostic contrast imaging.

Broadly, there are two approaches to acoustically generating a bubble:

1. produce a bubble from the bulk fluid directly. In medical ultrasound the bulk will invariably be some aqueous solution.
2. introduce a second fluid, immiscible to the bulk, from which to generate bubbles.
This second fluid - an oil in the aqueous bulk - can be chosen with properties to facilitate the acoustic generation of a bubble.

Unfortunately, this division in methodology does not make clear the mechanisms by which a bubble may be generated. The bulk fluid will, unless extraordinary efforts are undertaken, contain small particles of dust that may or may not entrap pockets of gas, contain gas bubbles stabilised with trace amounts of detergent, in addition to containing a host of dissolved gases. Likewise for any secondary fluid that is introduced, with the additional complication of the water-oil interface becoming a rest point for other

impurities in the system and developing a complex chemistry of its own. Bubble generation is extremely sensitive to the surface chemistry of a nascent bubble^[104], while the presence of motes and existing bubbles can change the mechanism of bubble generation entirely. The presence of dissolved gasses is also known to be important in bubble generation^[107], although this case is not investigated in this thesis.

Historically the term *cavitation* has been used ambiguously with respect to the mechanism of bubble formation. It is therefore helpful to instead use the word *nucleation* with the more careful categorisation of Jones^[49]:

Type 1: classical homogeneous nucleation: a bubble is *created* within the bulk medium where no bubbles were present prior to the reduction in pressure,

Type 2: classical heterogeneous nucleation: a bubble is *created* upon a solid particle floating in the medium, or in a crevice in the surface of the container,

Type 3: pseudo classical nucleation: a bubble results from a *pre-existing* but sub-critical gas cavity. The gas cavities may be stabilised by a crevice in a floating particle or by a crevice in the container, or may be bubbles stabilised by a variably permeable skin^[121]. Sub-critical means that their curvature is smaller than the *critical radius*, the radius at which the bubble is in equilibrium with its surroundings. The bubble must still overcome an energy barrier to grow.

Type 4: non-classical nucleation: a bubble results from a *pre-existing* gas cavity but there is no energy barrier to growth. This occurs when the radius of curvature of a crevice is larger than the critical radius. It is the lack of the energy barrier that makes this nucleation non-classical.

With these differing mechanisms in mind our two broad methodologies are revisited. By what mechanism can the bulk fluid (water) be nucleated with ultrasound? Is the mechanism the same in an oil emulsion?

2.1.1 THE NUCLEATION OF WATER

The pressures required for water to undergo type I nucleation are prohibitive for diagnostic ultrasound. Herbert^[37] measured the nucleation probability to be vanishingly small at -20 MPa, with the probability rising to 50% at -26 MPa, a result typical of other measurements^[36]. However, gas can be extracted from water at negative pressures at a few atmospheres^[116]. Such nucleation events must result from another mechanism.

Motes promote nucleation by reducing the surface area of the vapour-liquid interface, thereby reducing the energy required to form the bubble. In the absence of entrapped gas - when the crevices are fully *wetted* with the bulk fluid - type 2 nucleation occurs. The reduction in the energy barrier can be considerable and is greatest when the crevices are deep and narrow^[66]. Herbert^[37], for instance, noted that while tap water has the same 50% cavitation threshold as purified water, tap water has a very long tail of rarer nucleation events at much less extreme pressures. Although not fully determined in the article, it seems reasonable to suggest that these events occur through type II nucleation: Herbert uses repeated pulses that have negative pressures in excess of 15 MPa and at such high pressures it is likely that gas entrapped in motes is removed by earlier pulses. This would be consistent with a 50% cavitation threshold that is identical to purified and degassed water, a result that is hard to reconcile if there is entrapped gas within the system.

Nucleation events in human tissue are relatively rare, and do not become probable until the type I/II nucleation thresholds of water^[113]. Biology, it seems, is very adept at preventing gas pockets from occurring within tissue.

The high cavitation pressures recorded for type I and type II nucleation mean that the nucleation of impure water at diagnostic pressures is believed to proceed via type III and IV nucleation^[5;12;49]. There are two models for type III and IV nucleation. The first is that partially wetted motes trap gas^[5] and the second is that organic impurities stabilise freely floating gas bubbles^[121]. Both suggestions have been observed experimentally^[12;48] and both are thought to be important in practice.

Due to the high cavitation pressures in biological tissues, a medium that introduces Type III and IV nucleation events is a prime targets for developing a contrast agent. These media have traditionally introduced stabilised micron sized bubbles. There is no reason why they should not, alternatively, introduce gas entrapped in motes, such as are found in regular tap water.

2.1.2 THE NUCLEATION OF AN OIL DROPLET WITHIN AN EMULSION

To leave the blood through leaky tumour vasculature the radius of a droplet must be at most 300 nm^[30;35;40]. What is the likely nucleation mechanism for a droplet this small? Let us first estimate the probability that the droplet contains a mote.

The probability that a droplet contains a mote depends both on the purity of the oil used to make up the droplets and the purity of the surrounding medium. We assume that the proportion of oil in the medium is small and that the impurities from the bulk dominate. We also neglect any differences in the affinities of the oil and bulk to the mote. Finally, we suppose that we make no special effort to either clean or dirty the water, but instead take the water straight from the tap. For the mote-density of tap water we shall use Apfel's^[4] suggestion of 10^5 cm^{-3} .

From Apfel's density it follows that for every mote there will be

$$\frac{1}{\text{motes per volume} \times \text{volume per droplet}} = 10^8 \quad (2.1)$$

droplets with a radius of 300 nm. Since a pre-existing gas bubble (stabilised or not) would have to be exceptionally small to be trapped within 300 nm oil droplet, we conclude that the oil droplets of interest are likely to undergo type I nucleation. Indeed, the use of small droplets to avoid the problems of 'dirty' water is a well used technique for experimentally investigating type I nucleation^[4;79;112]. For instance, Turnbull^[112] found that droplets of 2-8 μm bubble are required to homogeneously freeze mercury. Such droplets are already an order of magnitude larger than what is required to leave the blood, and it therefore seems reasonable to suggest that smaller droplets will nucleate

Table 2.1: Boiling points and critical temperatures of various perfluorocarbons

	Boiling Point	Critical Point
	(°C)	(°C)
Perfluoroethane	-78	20
Perfluoropropane	-38	72
Perfluorobutane	-1.7	113
Perfluoropentane	29	149
Perfluorohexane	59	176

homogeneously.

Type I nucleation can be challenging to initiate. For an oil to undergo type I nucleation at conventional ultrasound pressures it must either have a much lower boiling point than water, or be able to dissolve a much greater concentration of gas. In this chapter we consider the perfluorocarbons. This series of oils is characterised by their low boiling points, given in Table 2.1, and their high solubility of many gases. The perfluorocarbons are also chemically inert and have been used before in medical applications^[57;92].

To simplify the discussion further, this chapter assumes that the type 1 nucleation occurs entirely within the perfluorocarbon droplet. The water is neglected. The exceptionally low solubility (a few parts per million^[115]) of the perfluorocarbons in water goes some way to justify this approximation.

The assumption is not without its problems. The small size, potentially, could make a droplet a poor approximation to an ‘infinite thermodynamic system’, with the finite volume errors that this can entail. However, neglecting the nucleation at the interface remains a limitation of our approach. Techniques for lifting the restriction have been considered by others^[45;50], but we do not pursue these here.

2.1.3 STRUCTURE OF THE CHAPTER

During the course of this thesis two contrast media with two differing nucleation mechanisms shall be investigated: the type III/type IV nucleation of a mote found in “dirty water”, and the type I nucleation of an oil droplet. In the first case the driving wave is used to evacuate gas entrapped on motes and to manipulate the size of the resulting (and pre-existing) bubbles. In the second case the driving wave is used to initiate the nucleation of the perfluorocarbon droplet and manipulate the resulting bubble’s diameter.

Three preliminary questions need to be addressed in order to investigate the role of the driving wave in each of these mechanisms:

1. What size of bubble will be generated from each nucleation mechanism?
2. What pressures are required to generate type I nucleation of bubbles?
3. What is the lifetime of the generated bubbles? Is there time for them to be imaged with ultrasound before they redissolve into the fluid?

Each of these questions depend upon the *critical radius* of a bubble - the radius at which it is thermodynamically favourable for the bubble to neither grow nor shrink. In the first case, the critical radius must be reached for a bubble to grow beyond its nascent state, or to free itself rather than shrink back into its crevice. The critical radius therefore provides, as a function of pressure, a lower bound to the size of the bubble. Secondly, the critical radius defines the energy required for the bubble to form. The probability of a type I nucleation event then follows via the Aarenhuis equation. Finally, the critical radius is a limiting radius when calculating the lifetime of a generated bubble.

The evaluation of the critical radius is therefore the first objective of this chapter. It will be discussed in detail in section 2.2 and will directly answer the first of our questions. The pressures required for type I nucleation will be calculated in section 2.4. Finally, the lifetimes of the expected bubbles will be calculated in section 2.5.

2.2 THE CRITICAL RADIUS OF A BUBBLE

2.2.1 THE DEFINITION OF THE CRITICAL RADIUS

When the rarefactional pressure of the acoustic wave exceeds the atmospheric pressure it places the fluid under tension. The creation of a vapour bubble relaxes this pressure but also creates an interface. Creating a small bubble is energetically unfavourable because the energy required to maintain the interface dominates. A large bubble, on the other hand, will grow explosively when placed under tension because the relaxation in pressure caused by the bubble's volume dominates. For a given pressure there exists, therefore, a *critical radius*, a^* , at which the bubble neither grows nor shrinks but is at thermodynamic equilibrium. If spherical symmetry is assumed then the critical radius is such that^[77;78]

$$\frac{d\Omega}{da} = 0, \quad \text{at } a = a^* \tag{2.2}$$

where Ω is the *grand potential* and a is the bubble's radius.

2.2.2 THE CAPILLARY APPROXIMATION TO THE CRITICAL RADIUS

The grand potential is straight forward to evaluate if it is assumed that:

- the density of the liquid,
- the equilibrium vapour pressure and
- the equilibrium surface tension between liquid and vapour

all take their bulk values. This set of assumptions is the capillary approximation: the liquid and bubble are assumed to be separated by a sharp interface and the surface tension is taken to be that of the macroscopic plainer interface. The argument strictly applies only in the thermodynamic limit.

When the nucleating bubble is very small the thermodynamic limit can be a poor approximation^[105]. The distance over which the density changes from liquid to vapour

if often not insignificant and the surface tension is typically reduced from its bulk value^[54]. We shall investigate the validity of the capillary approximation for the case of water and perfluoropentane in section 2.6.2, but for the time being we continue.

If a bubble is created adiabatically then the energy required to form a bubble of radius a is^[16;51]

$$\Delta\Omega = 4\pi\gamma a^2 - \frac{4\pi a^3}{3} (p_v - p_L) + i (\mu_v(p_v) - \mu_L(p_L)). \quad (2.3)$$

Here $\Delta\Omega$ is the change in the grand potential, γ is the surface tension. p_L and p_v are the pressures of the oil droplet and the vapour, $\mu_L(p_L)$ and $\mu_v(p_v)$ are the chemical potentials (per molecule) of the oil droplet and vapour at their given pressures, and i is the number of molecules in the newly created vapour bubble. The first term on the right hand side of equation 2.3 is the contribution from the surface tension. The second is the energy released by the change in volume, the third is the energy generated from the chemical potential by the transport of molecules.

The critical radius is when the energy barrier $\Delta\Omega$ is minimal (equation 2.2). By differentiating 2.3 with respect to a it is found to be

$$a^* = \frac{2\gamma}{p_v^* - p_L}, \quad (2.4)$$

which is the Laplace relation. The pressure, p_v^* , is the critical pressure within the bubble. Due to the bubble's curvature it is not equal to the equilibrium vapour pressure of a flat interface, denoted p_∞ . The two vapour pressures are related by the Poynting correction,

$$p_v^* = p_\infty \exp\left(\frac{V_m (p_L - p_\infty)}{RT}\right), \quad (2.5)$$

where V_m is the molar volume and R is the ideal gas constant. Equation 2.5 is derived, for completeness, in Appendix B.

Substituting 2.4 into 2.3 gives the energy required to create a bubble of critical radius,

$$\Delta\Omega^* \equiv \Delta G|_{a=a^*} = \frac{16\pi\gamma^3}{3(p_v^* - p_L)^2}. \quad (2.6)$$

The chemical potentials have vanished from 2.6 because the bubble is at thermodynamic equilibrium, whence the grand potential equates to the Gibbs free energy, G , because

$$\mu_v(p_v^*) = \mu_L(p_L), \quad \text{at } a = a^*. \quad (2.7)$$

2.3 QUESTION 1: A LOWER BOUND ON THE SIZE OF A BUBBLE

We are now in a position to answer the first of our questions: the size of bubble expected to be cavitated. This is because the critical radius provides a lower bound for vapour bubbles in solution. A bubble smaller than the critical radius will shrink even when placed under tension, and so is very unlikely to be observed.

Figure 2.1a uses equation 2.4 to plot the the critical radius as a function of pressure for water, perfluoropentane and perfluorobutane at 298 K. The capillary approximation predicts that the critical radius is smaller for the perfluorocarbons than for water. This is encouraging, for it implies that type I nucleation is easier to induce for the perfluorocarbons than for water.

At high pressures the critical radii of the two perfluorocarbons converge. This is because the critical radius depends linearly on the surface tension (equation 2.4) and the surface tensions are similar for perfluorocarbons. Using a perfluorocarbon with a lower boiling point will enable smaller stable bubbles only at the more moderate pressures where the vapour pressure plays a greater role. If higher pressures are used then the effect is negated.

It should be noted that the vapour pressure used for perfluorobutane was extrapolated by 29 °C outside of its range of validity^[64] by use of Antoine's equation. Since 25 °C is above the boiling point of perfluorobutane no equilibrium vapour pressure can be

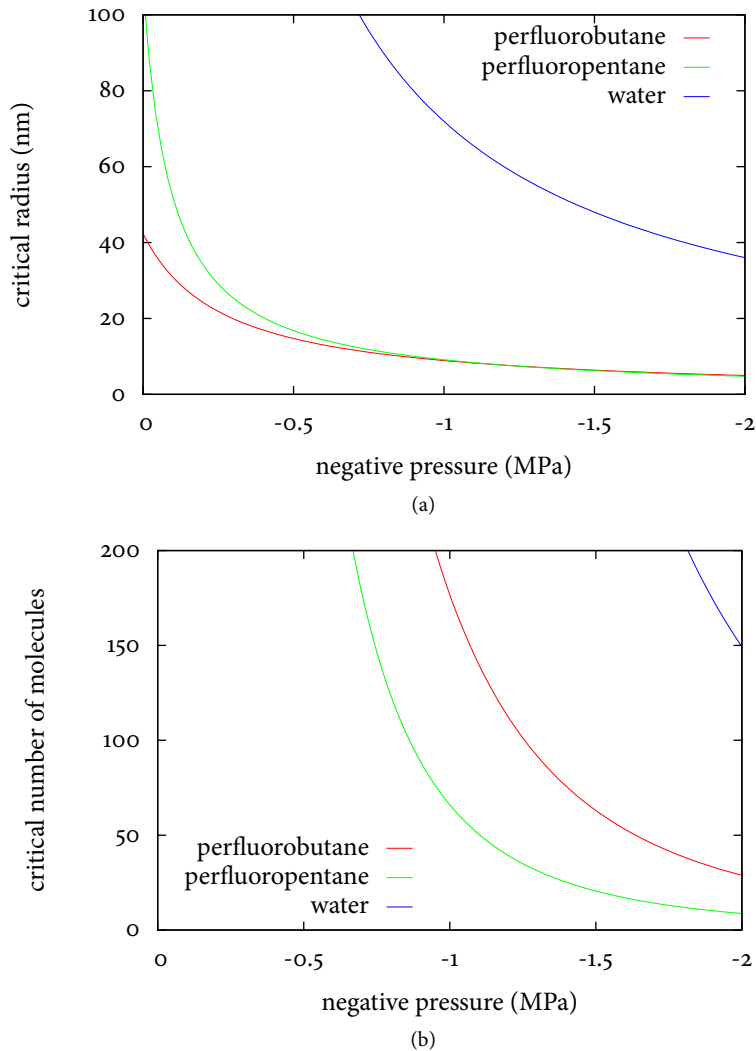


Figure 2.1: Capillary predictions for the critical radius and critical number of molecules for a bubble as a function of the pressure at 298 K. The vapour is assumed to be an ideal gas, with the vapour pressure obtained by experimental fits to Antoine's equation. The coefficients for Antoine's equation are taken from National Institute of Standards Database^[64] (Note that the perfluorobutane data is used outside of its range of validity, see text).

defined. However, since 25 °C is also well below the critical temperature, it is hoped that the predicted pressures within the (super-heated) bubble are still meaningful.

In Figure 2.1b the predicted number of molecules contained within a critical bubble are plotted. Again and as expected the number of perfluorocarbon molecules required to form a bubble are smaller than for water. Figure 2.1b does, however, illustrate the difficulty with the capillary approximation being used. It is highly questionable that a bubble containing tens or even hundreds of molecules behaves like its thermodynamic bulk, with a constant density until the interface.

The capillary approximation predicts that a greater number of molecules are required to form a critical bubble for perfluorobutane than for perfluoropentane. This is again due to the higher vapour pressure of perfluorobutane.

2.4 QUESTION 2: THE VAPOURISATION PRESSURE OF A PERFLUOROCARBON

DROPLET

There are two possible goals that may be set when imaging a bubble generated from a perfluorocarbon droplet:

1. image the actual vaporisation event,
2. image the resultant bubble after it has vaporised but before it redissolves.

Due to the stochastic nature of bubble nucleation, the pressures required to achieve these goals are best expressed in terms of pressures required to achieve a given rate of nucleation, the rate being such that observations are likely in the time frame of a given experiment.

2.4.1 THE RATE REQUIRED TO IMAGE A VAPORISATION EVENT

For a nucleation event to be directly imaged it must occur within the acoustical volume of the imaging pulse - the volume in which the pressure is near its peak. The imaging volume is most simply approximated as a cylinder and the pulse's principle wavelength,

λ , makes a reasonable estimate for the diameter of a focused pulse. If the pulse is n cycles long then the acoustical volume, V , is given as so,

$$V \approx \frac{n\pi\lambda^3}{4}. \quad (2.8)$$

The duration of the pulse is $\tau_p = n\lambda/c$ and so it follows that the rate, R , at which the medium is sampled is

$$R \approx V/\tau_p = \frac{c\pi\lambda^2}{4} \quad (2.9)$$

The sampling rate of a 15 MHz imaging pulse is therefore approximately $10 \text{ cm}^{-3}\text{s}^{-1}$. This gives the minimal rate of nucleation that would be expected to be observed with a single a-line pulse. It is only marginally greater than the limit of observation typically chosen in other nucleation applications: $1 \text{ cm}^{-3}\text{s}^{-1}$ ^[79]. For consistency with other applications, we therefore use this latter definition of $1 \text{ cm}^{-3}\text{s}^{-1}$ as the limit of what can be observed with ultrasound. This corresponds to one nucleation event every 10 pulses.

2.4.2 THE RATE REQUIRED TO IMAGE A GENERATED BUBBLE

If only the bubble resulting from a nucleation event needs to be imaged, rather than the nucleation event itself, then the observable rate of nucleation is much lower. This is because the bubble is potentially observable if the pulse passes within its lifetime and so it is the lifetime of the bubble, τ_b , and not the duration of the acoustical pulse, that defines the observable nucleation rate,

$$R \approx V/\tau_b = \frac{n\pi\lambda^3}{4\tau_b} \quad (2.10)$$

The value of τ_b will be evaluated when we consider the third of our questions in section 2.5.

2.4.3 THE RATE OF BUBBLE NUCLEATION

The rate of nucleation per unit volume is given by the Aarenhuis equation,

$$J = J_0 \exp\left(-\frac{\Delta\Omega}{k_B T}\right), \quad (2.11)$$

where $\Delta\Omega$ is the energy barrier to nucleation (in terms of the Grand Potential, Ω), k_B is Boltzmann's constant, T is the temperature and J_0 is a rate (per unit volume) obtained when $T \rightarrow \infty$ or when $\Delta\Omega \rightarrow 0$.

The rate constant, J_0 , for bubble nucleation is problematic. The reason is that the definition of a very small bubble is not clear conceptually. What is meant, for example, by a bubble of three molecules? And how does one know when a new molecule has joined it? Such uncertainties mean that arguments for J_0 very rapidly lose their precision. In contradistinction, the formation of a liquid droplet from a saturated vapour is clear conceptually: a droplet of three molecules is easy to envisage, a cluster of just a few molecules is easier to define than a void. Collision theory provides plausible arguments for the rate of droplet formation in a saturated vapour^[51]. Be it on the grounds of reciprocity, or simply because a better alternative cannot be found, the rate constant J_0 for bubble formation is usually taken to be the same as that for the formation of a liquid droplet from a saturated vapour^[76].

Rather than repeat a spurious argument we prefer to estimate J_0 by dimensional analysis. The result is the same as that used in the literature and is obtained at a fraction of the effort. In addition, the estimate obtained here does not give the impression of greater accuracy than it deserves, a danger ever present in kinematic derivations.

At high temperatures, or when the energy barrier ΔG vanishes, one would expect the detailed chemistry of the medium to become unimportant with the liquid medium characterised as a collection of point particles of mass, m , and number density, ρ_l . Likewise, a vapour bubble within the medium characterised by its number density, ρ_v , and surface tension, γ . These properties are summarised in Table 2.2 along with their dimensions. There are five variables listed comprising of three dimensions: mass

Table 2.2: Dimensionless groups in the calculation of the nucleation rate constant

	Parameter	Symbol	Dimension
Bubble	Rate of bubble growth	J_0	$[L]^3[t]^{-1}$
	Vapour number density	ρ_v	$[M][L]^{-3}$
	Surface tension	γ	$[M][T]^{-2}$
Fluid	Fluid number density	ρ_l	$[M][L]^{-3}$
Particle	Particle mass	m	$[M]$

$[M]$, length $[L]$ and time $[t]$. It is therefore possible to write down 2 dimensionless groups^[33].

To eliminate the temporal dependence J_0 must be squared and combined with surface tension. The resulting J^2/γ has the units $[M]^{-1}[L]^{-6}$. These dimensions can be cancelled by using the particle mass and the square of a number density. There is a choice as to which of the number densities, ρ_L and ρ_v , should be used. Le Chatelier's principle advises that that denser liquids are more expensive (in terms of energy) to separate, and that denser bubbles are less expensive to maintain. One would expect, therefore, the rate J_0 to be proportional to ρ_v .

$$\Pi_1 = \frac{J_0^2 m}{\gamma \rho_v^2}. \quad (2.12)$$

The second dimensionless group that can then be formed is then simply ratio of the densities,

$$\Pi_2 = \frac{\rho_v}{\rho_L}. \quad (2.13)$$

Writing Π_1 as some function, g , of Π_2 we obtain,

$$J_0 = \rho_v \sqrt{\frac{\gamma}{m}} g\left(\frac{\rho_v}{\rho_L}\right). \quad (2.14)$$

The function g is undetermined but for the reasons just argued we anticipate g to increase with ρ_v and decrease with ρ_L . The simplest such relationship is a linear one and so we guess $g(x) \propto x$. If the constant of proportionality is assumed to be approximately unity, then for bubble nucleation we have

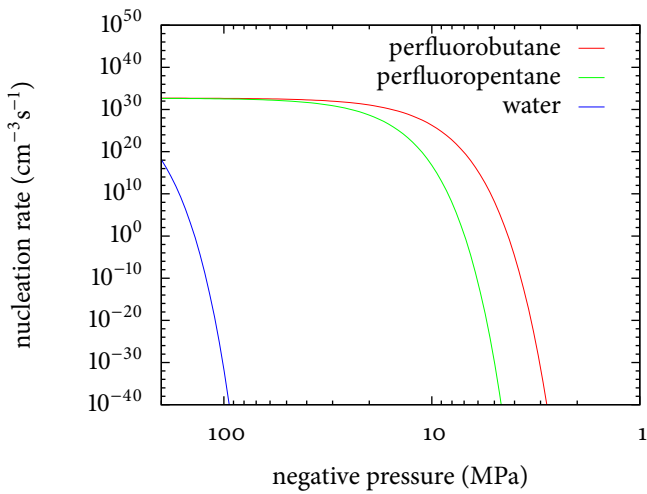
$$J_0 \approx \frac{\rho_v^2}{\rho_l} \sqrt{\frac{\gamma}{m}}, \quad (2.15)$$

This is identical to the result of the collision theory argument of Katz^[50]. For water $J_0 \approx 10^{34} \text{ cm}^{-3}\text{s}^{-1}$ and for perfluoropentane $J_0 \approx 10^{32} \text{ cm}^{-3}\text{s}^{-1}$.

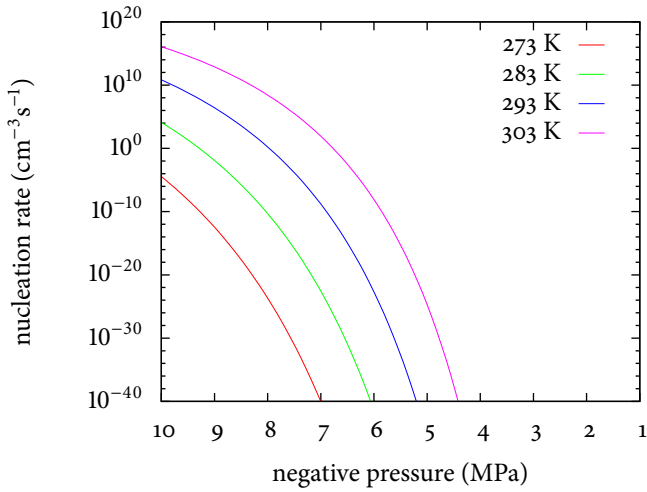
2.4.4 RESULTS

The nucleation rates calculated with the capillary approximation are plotted in Figure 2.2. In Figure 2.2a the rates for perfluorobutane, perfluoropentane and water are plotted. As expected from the plot of critical radii, Figure 2.1a, high rates of nucleation are obtained at lower pressures with the perfluorocarbons than for water, with perfluorobutane being more easily cavitated than perfluoropentane. This is encouraging, for increasing the rate of type I nucleation was the motivation for considering the perfluorocarbons.

However, the pressures given by Figure 2.2 to observe type I nucleation are high for diagnostic ultrasound. Figure 2.2a suggests that perfluorobutane, even when in a super-saturated state, will require a negative pressure in the region of 4 MPa to be observable. Such pressures are used in medical ultrasound, but require the specially engineered transducers of HIFU. To observe perfluoropentane the negative pressure will need to be in the region of 8 MPa, and while Figure 2.2b shows that the temperature is influential, it is not so influential as to shift the pressures back to those obtainable with diagnostic transducers. These pressures are of the same order of magnitude as the experimental values of Schad^[94].



(a) Nucleation rates for water, perfluoropentane and perfluorobutane at 25°C.



(b) Nucleation rates for perfluoropentane at different temperatures.

Figure 2.2: Nucleation rates evaluated from equation 2.11. The NIST Chemistry Web-Book^[64] being used as the source for the required experimental constants.

Table 2.3: Symbols used in the calculation of dissolution times

Symbol	Description	units	Value	
			(Air)	(PFP)
γ	Surface tension	N/m	0.07280 ^[93]	0.0096828 ^[64]
H	Henry's constant	$\text{m}^2 \text{kgs}^{-2} \text{mol}^{-1}$	1.48472×10^{-7} ^[93]	3.54634×10^{-4} ^[103]
D	Diffusivity	$\text{m}^2 \text{s}^{-1}$	2.05×10^{-9} ^[93]	6.409×10^{-10} ^a
P_∞	Ambient Pressure	MPa	0.101325	0.101325

^a Estimated with the Hayduk-Laudie equation

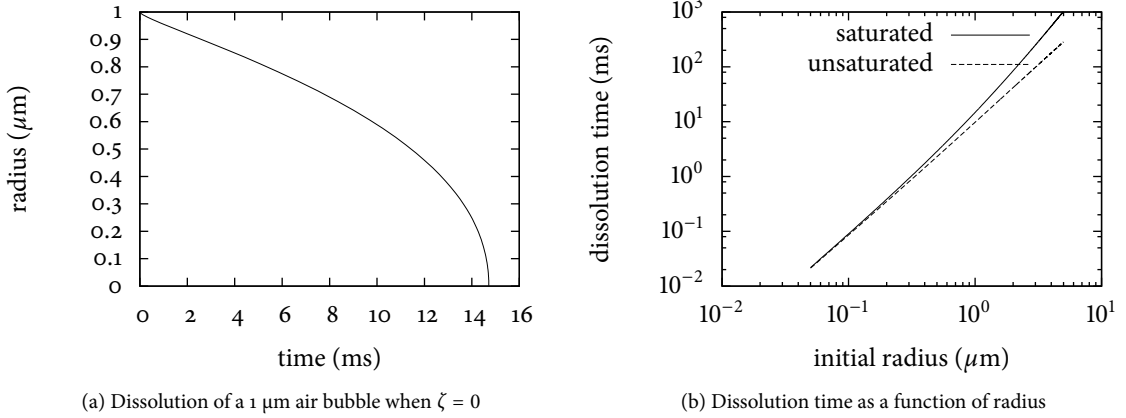


Figure 2.3: Dissolve times of air bubbles. The experimental quantities used in the model are given in Table 2.3.

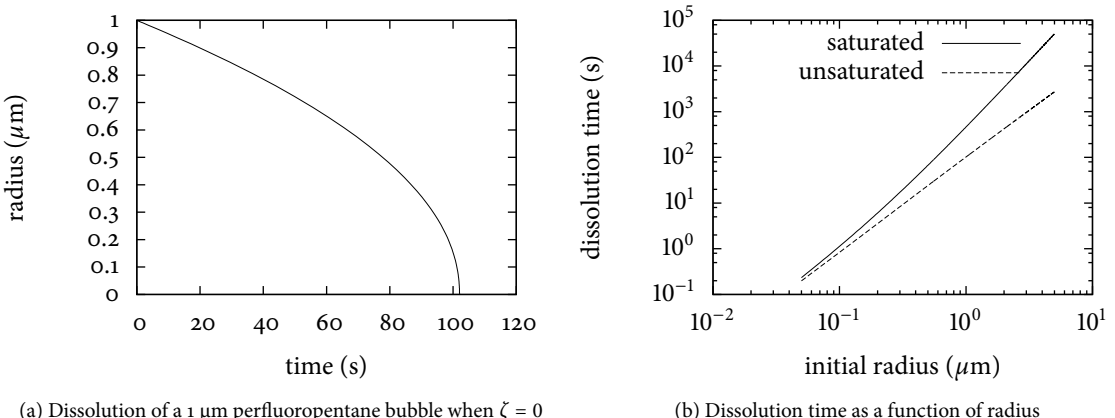


Figure 2.4: Dissolve times of perfluoropentane bubbles. The experimental quantities used in the model are given in Table 2.3.

2.5 QUESTION 3: THE LIFETIME OF A VAPOUR BUBBLE

The third and final question of this chapter regards the expected lifetime of a bubble. In section 2.3 the critical radius was used to give a lower bound on the size of a bubble generated in a perfluorocarbon droplet or evacuated from a moat. It was seen that bubbles in the tens of nanometres can be stable when placed under tension by the rarefactional cycles of an acoustic field. The expected lifetime of the bubble after the rarefaction has passed will now be calculated.

This section uses a very simple model that was first derived by Epstein and Plesset^[21], although we prefer the notation of Gor^[34]. The hope is to obtain only an order of magnitude estimate of the bubble lifetime and so some accuracy can be foregone.

In the model a gas bubble is placed in a fluid of uniform pressure, where the medium in the vicinity of the bubble contains the gas at concentration n_0 . Two gas bubbles will be considered, an air bubble that contains nitrogen and oxygen, and a perfluoropentane bubble. In each case it will be assumed that the bubble contains no water vapour, and that the surface of the bubble is has no stabilising shell¹. The concentration of the medium far from the bubble is denoted n_∞ and is chosen to be the ambient density of the gas in the medium at standard temperature, T , and pressure, p_∞ . While we imagine the bubble to be generated in a rarefaction cycle of an acoustic wave we neither model the generation of the bubble nor the sound pulse.

There are two cases of particular interest

1. when the concentration of dissolved gas in the bubble's vicinity is equal to the ambient concentration,

$$n_0 = n_\infty. \tag{2.16}$$

Such will be the case when a bubble is generated in a medium that is unaltered by the passing of the acoustic wave. This will typically be the case for short pulses

¹See Sarkar^[93] for a recent discussion of the dissolution of a bubble that has a permeable shell.

of low pressure.

2. when the concentration of the gas in the bubble's vicinity is much lower than the ambient concentration. This situation can arise when a previous pulse of a high pressure wave has already evacuated most of the gas in the focal zone. The limiting case is when

$$n_0 = 0. \quad (2.17)$$

It is therefore natural to frame the derivation in terms a dimensionless measure of saturation,

$$\zeta \equiv \frac{n_0 - n_\infty}{n_\infty} \quad (2.18)$$

The two cases of interest are when $\zeta = 0$ and $\zeta = -1$. The solubility of the medium will make a second useful dimensionless quantity^[34]

$$s \equiv \frac{k_B T n_\infty}{P_\infty}. \quad (2.19)$$

Imbalances in the number density of the gas in the medium will prompt diffusion from the vicinity of the bubble to the bulk. Modelling this as Fickian diffusion in a spherical geometry gives,

$$j_D = -D \frac{\partial n}{\partial r} \quad (2.20)$$

where the density is a spherical symmetric function of radius, r . If diffusion transport terms are neglected then 2.20 can be solved to obtain,

$$\frac{\partial n}{\partial r} = (n_R - n_0) \left[\frac{1}{R} + \frac{1}{\sqrt{\pi D t}} \right], \quad (2.21)$$

where R is the bubble radius and n_R is the concentration of dissolved gas at that radius. The details of the derivation were given in Epstein and Plesset's^[21] original paper and

do not need to be reproduced here.

Material conservation requires that the number of particles passing through the radius of the bubble equates to the change in the number of particles in the bubble, N ,

$$\frac{dN}{dt} = 4\pi R^2 j_D \frac{\partial n}{\partial r}. \quad (2.22)$$

Modelling the contents of the bubble as an ideal gas lets the particle number be expressed in terms of the ambient pressure, P_∞ , and surface tension γ of the bubble,

$$N = \frac{4\pi R^3}{3k_B T} \left[P_\infty + \frac{2\gamma}{R} \right]. \quad (2.23)$$

By differentiating 2.23 and equating the result to 2.22 a differential equation for the change in bubble radius is obtained,

$$\dot{R} \left[1 + \frac{4\gamma}{P_\infty R} \right] = Ds \left[\zeta - \frac{2\gamma}{P_\infty R} \right] \left[\frac{1}{R} + \frac{1}{\sqrt{\pi D t}} \right], \quad (2.24)$$

where equation 2.19 has been used, along with

$$\frac{(n_0 - n_R)}{n_\infty} = \zeta - \frac{2\gamma}{P_\infty R} \quad (2.25)$$

which follows from 2.18.

The numerical solution of 2.25 is plotted for a 1 micron air bubble in Figure 2.4. It is seen that the bubble radius decreases fairly constantly until a very rapid final collapse. The lack of a long tail in Figure 2.4 means that the dissolution time is dominated by periods when the bubble is near its starting radius. There is not a long decay during which the bubble is technically existent but is so small as to be unobservable.

The dissolution time for an air bubble as a function of radius is plotted in Figure 2.3b. Both the saturated and unsaturated cases are plotted. The dissolution times for very small bubbles is very similar, but starts to diverge for bubbles of radius 0.5 μm .

The lifetime of a free submicron air bubble is of order 1 ms in both the saturated and

unsaturated cases. The pulse duration of diagnostic ultrasound is typically measured in microseconds and so the bubble would be expected to live throughout the duration of the pulse. However, adjacent alines in a diagnostic pulse are often tens of milliseconds apart. Submicron air bubbles would not be expected to exist in adjacent alines. The short lifetimes of air bubbles mean that care needs to be taken to synchronise the generation and the imaging of a bubble, so that the imaging wave samples the same focal region as the driving wave within a few microseconds of the driving wave passing.

The solubility of the perfluorocarbons in water is much lower than for nitrogen and oxygen. While the dissolution characteristics are very similar to an air bubble (Figure 2.4b) the timescale for dissolution is order of magnitudes larger (Figure 2.4a). This has the advantage that a bubble can be generated at a different time (and therefore at a different location) to where the bubble is imaged. In this case the driving wave and the imaging wave can be considered independently.

2.6 DISCUSSION

2.6.1 SUMMARY OF RESULTS

In this chapter the two broad approaches of generating a bubble with sound for the purpose of imaging are analysed.

On the one hand one may attempt to create a bubble via type I nucleation. The pressures required to do so in water are beyond the capabilities of diagnostic ultrasound and so one may instead focus on creating an emulsion with a second medium that is easier to nucleate. The perfluorocarbons, due to their low boiling points, low solubility and low toxicity make excellent candidates. This chapter has suggested by means of the capillary approximation that very few perfluoro-molecules are needed to create a bubble, and that the nucleating pressure is much reduced - down to 7-8 MPa negative pressure for perfluoropentane. These pressures are still on the cusp of what is used in medical ultrasound and are still beyond what can be achieved with a diagnostic transducer. However, given the questions regarding the approximation's accuracy that are

raised by the calculated number of nucleating molecules - in the tens and low hundreds - the perfluorocarbons still most definitely represent a contrast medium that is worthy of experimental study.

On the other hand one may abandon type I and type II nucleation altogether and focus on extracting gas that is stabilised in impure water. The main difficulties in this approach is to control the impurities in the water so that small bubbles are not overwhelmed by larger bubbles, and to image the generated bubble within its millisecond lifetime. Generating bubbles at diagnostic pressures is not a challenge in this approach. Indeed, great pains are usually gone through in ultrasound experiments to prevent such bubble generation.

A certain degree of control can be exerted on the size of bubble generated in by type III nucleation. From 2.24 the critical radius of an air bubble is found to be

$$R^* = \frac{2\gamma}{\zeta P_\infty}. \quad (2.26)$$

The Laplace relation, 2.4, cannot be used as it focuses solely on vapour bubbles. The saturation, ζ , can be plotted as a function of pressure by using Henry's law, which finds that density a gas in water is proportional to the applied pressure,

$$P = Hn, \quad (2.27)$$

where H is Henry's constant. One finds that

$$R^* = \frac{2\gamma}{n_0 H - P_\infty}. \quad (2.28)$$

Since the critical radius provides a lower bound on the size of the evacuated bubble, equation 2.26 provides an estimated on the size of bubble that is generated in dirty water.

2.6.2 CONCERNS WITH THE CAPILLARY APPROXIMATION

The assumptions of the capillary approximation are problematic when the nucleating bubble is very small^[105] because the distance over which the density changes from liquid to vapour is not insignificant and because the surface tension is typically reduced from its bulk value^[54].

Deviations from the capillary approximation are exponentially important in rate calculations, which follows from the Arrhenius equation. For example, an increase in the surface tension of 15% was calculated^[54] to change the predicted nucleation rate by 10^{17} . Another example is provided by the calculations of Talanquer and Oxtoby^[78;105]. Their density functional calculations, that relaxes the requirement for sharp interfaces between liquid and vapour, predicted that the rates from these calculations were *typically* 20 orders of magnitude different from those of classical nucleation theory.

The version of the classical nucleation theory used here is perhaps the simplest that can be used. There are many modifications that alter in some way the exponential in 2.11, and thereby drastically altering the rate predictions. The problems of the capillary approximation are common to all classical theories, however, and so the simple application here is representative.

Perhaps the most relevant of the modified classical theories is the careful application to bubble nucleation carried out by Delale^[16]. In addition to the problems associated with the capillary approximation, Delale notes that it is unlikely in ultrasound applications for cavitation to proceed on a reversible path, as is assumed. Furthermore, the viscous dampening at the bubble-oil interface, which is known to be important in bubble dynamics, mean that at thermodynamic equilibrium (when the bubble's radius is at its critical size), the bubble is not in mechanical equilibrium. Delale^[16] convincingly argues for a phenomenological term should be added to the Gibbs energy difference to correct for these problems. Unfortunately the terms of this correction are difficult to ascertain far from the critical temperature. It is therefore difficult to apply Delale's theory in this thesis^[16].

2.6.3 TESTING THE VALIDITY OF THE CAPILLARY APPROXIMATION

For small bubbles, the assumption of a sharp interface between the bubble and its medium is open to criticism. Can the width of the interface really be insignificant for a bubble 50 nm wide? In this section we investigate the issue by taking an alternative approach, the density functional programme of Oxtoby and Evans^[78].

Density functional theory relaxes the capillary approximation used in classical nucleation theory. The density of the nucleated bubble is not assumed to be uniform, and the interface is not assumed to be macroscopic and plainer^[77;78]. The density functional approach therefore does much better at modelling the interface than classical nucleation theory. Rather than it being a sharp boundary, there is a finite interval over which the density varies from that of the fluid to that of the vapour. In addition, and as will be shown, the energy barrier to the phase change vanishes at the spinodal. This is as it should be, but marks a second major improvement on the classical theory^[106].

Density functional theory starts by modelling the inter-molecular potentials. Good models for the fluid potential exist and among the most widely used are the Lennard-Jones potential and the Kihira potential. The former describes small spherically symmetric molecules very accurately. The latter is an extension on the Lennard-Jones model to describe larger, less symmetric molecules.

In principle, macroscopic predictions can then be drawn by inserting the intermolecular potentials into the usual thermodynamic potentials of statistical mechanics. While the full multi-particle potentials are in general insolvable and approximations must be made, the density functional approach is one derived from a firm theoretical base^[24]. Unfortunately, when applied to nucleation, the first principles approach has only ever had qualitative success^[76;107], with the predictions being very sensitive to the modelled molecular scale parameters.

The semi-empirical approach of Nyquist^[76] and Talanquer^[107] attempts to temper this sensitivity by fitting the molecular-scale parameters to the experimental data used for the classical theory. By construction, therefore, the bulk thermodynamic predictions

of the model are correct. Thermodynamic arguments can then be used to obtain other quantities of interest, such as the nucleation rate. We shall use this approach to test the width of interface between the bubble and its medium.

The density functional approach models fluctuations about the bulk properties of the fluid. It is therefore a mean-field approach that fails, like all mean field theories, near to the critical temperature. One must be cautious, therefore, only to apply it to nucleation events that occur well away from the critical point. In this thesis attention is restricted to nucleation events that are induced by a reduction in pressure rather than by boiling. The critical temperatures for a number of perfluorocarbons are listed in Table 2.1. It is interesting to note that for the perfluorocarbons the critical temperatures are considerably higher than their boiling points. At 37 °C, for example, perfluoropentane is in a meta-stable state but is still far from being ‘on the cusp’ of vapourisation. Type 1 nucleation events are still likely to occur via a reduction in pressure rather than an increase in temperature. On the other hand, perfluoroethane is above its critical point at room temperature and we consider it to be a little too close to its critical point to be considered in this thesis.

2.6.3.1 *Outline of approach*

The approach we will be taking can be summarised as follows:

1. write down an accurate model for the intermolecular potential (section 2.6.3.2),
2. approximate the model so that it can be solved (section 2.6.3.3),
3. fit the model’s parameters so that it reproduces macroscopic thermodynamics (section 2.6.3.4),
4. predict the shape of the interface between the bubble and its medium and compare it with the capillary approximation (section 2.6.4).

2.6.3.2 The density functional approach

The density functional approach is a statistical theory that attempts to model the grand potential, Ω , at a molecular level. The exact solution is intractable due to the mutual interactions between every molecule in the system.

To overcome this problem the true probability density function, $p_0(\mathcal{H}; \mathbf{r}_1, \mathbf{p}_1)$, that describes the positions of the particles and their momenta, is approximated to a simpler distribution $p(H; \mathbf{r}_1, \mathbf{p}_1)$ that may be solved. Here, \mathcal{H} , is the true Hamiltonian of the system and H is the approximate Hamiltonian with simpler interaction terms. We have also employed the convenient shorthand

$$\mathbf{r}_n \equiv r_n, r_{n+1}, \dots, r_N, \quad \text{and} \quad \mathbf{p}_n \equiv p_n, p_{n+1}, \dots, p_N. \quad (2.29)$$

to describe the positions and momenta of $N - n$ particles.

The *relative entropy* or *Kullback-Leibler divergence* gives the amount of information lost when using the approximate distribution p rather than the correct distribution p_0 , and is defined

$$D_{\text{KL}}(p||p_0) = \text{Tr} p \log \frac{p}{p_0}, \quad (2.30)$$

where Tr is the classical trace operator. The relative entropy has the property that $D_{\text{KL}}(p||p_0) \geq 0$, which follows from Gibbs inequality^[69]. Only if $p = p_0$ does $D_{\text{KL}}(p||p_0) = 0$. Therefore, once the structure of the approximate distribution p has been chosen, it can be varied to match to content of p_0 as closely as possible by minimising $D_{\text{KL}}(p||p_0)$.

Employing this variational procedure to approximate the thermodynamic potentials is ubiquitous in statistical physics^[120]. The point of departure for the density functional method is the realisation that

1. the *density is a functional of the external potential*. This follows because the approximation to the density is related to the single particle probability density

function

$$\rho(\mathbf{r}) \propto \iint d\mathbf{p}_1 d\mathbf{r}_2 p(H, \mathbf{r}, \mathbf{p}) \propto \int e^{-\beta \sum_i^N V_{\text{ext}}(\mathbf{r}_i)} d\mathbf{r}_2 \quad (2.31)$$

where $V_{\text{ext}}(\mathbf{r}_i)$ is the external potential at the position \mathbf{r} of the i^{th} molecule. Here we have extended the shorthand employed in 2.32 so that

$$d\mathbf{r}_n \equiv dr_n dr_{n+1} \dots dr_N, \quad \text{and} \quad d\mathbf{p}_n \equiv dp_n dp_{n+1} \dots dp_N. \quad (2.32)$$

2. *the external potential is uniquely determined by the density.* This converse result is known as the Hohenberg-Kohn theorem. It follows because the external potential is determined by the probability density, p , which is in turn determined uniquely by the density.

It is thereby permissible to work with the mass density rather than the probability density when considering the thermodynamics of the bubble. Since the density is the term of interest, the density functional approach is much more direct. We may therefore define an approximate grand potential, Ω_V , as a functional of the (approximate) density^[24],

$$\Omega_V[\rho] \equiv \beta^{-1} D_{\text{KL}}(p[\rho] || p_0) + \Omega. \quad (2.33)$$

The approximate grand potential approaches the true value when it is minimised with respect to ρ . Furthermore, since Ω is the grand potential at thermodynamic equilibrium, Ω_V is minimal when ρ describes the critical density distribution. The condition of equation 2.2 can therefore be expressed by the functional derivative^[77]

$$\frac{\delta \Omega_V}{\delta \rho} = 0, \quad \text{at } \rho = \rho^*. \quad (2.34)$$

The grand potential is related to the Helmholtz free energy by a Legendre transforma-

tion

$$\Omega_V = F - \mu \int d\mathbf{r} \rho(\mathbf{r}), \quad (2.35)$$

where μ is the chemical potential. The free energy, F , is the sum of internal energy, Φ , and an entropic contribution. The inter-particle interactions are contained within the internal energy.

2.6.3.3 Approximate the model

To simplify F it is noted that the interactions of most fluids are dominated by volume exclusion effects (van der Waal type interactions). Longer range interactions are, in general, only of secondary importance^[77]. If only pair-wise attractions are considered, then the internal energy can then be split into the free energy of a *hard sphere* reference fluid, F_{hs} and a small perturbation, ϕ_{attr} , that incorporates the long range attractions.

Then

$$F[\rho] = F_{hs}[\rho] + \frac{1}{2} \iint d\mathbf{r}_i d\mathbf{r}_j \phi_{attr}(\mathbf{r}_i, \mathbf{r}_j) \rho(\mathbf{r}_i, \mathbf{r}_j), \quad (2.36)$$

where $\phi_{attr}(\mathbf{r}_i, \mathbf{r}_j)$ is the residual two particle potential between a particle at \mathbf{r}_i and \mathbf{r}_j , not incorporated into F_{hs} . $\rho(\mathbf{r}_i, \mathbf{r}_j)$ is the two particle density function. (See Evans^[24] for a formal treatment of the above steps).

Next we model the attractive perturbation. To do so, we begin with a model for the full two particle interaction and then split it into attractive and repulsive parts, according the WCA procedure. For small symmetric molecules the Lennard-Jones 6-12 potential has good accuracy. It is given by

$$\phi_{LJ}(r) = 4\epsilon \left(\frac{\sigma^{12}}{r^{12}} - \frac{\sigma^6}{r^6} \right) \quad (2.37)$$

where $r = |\mathbf{r} - \mathbf{r}'|$, η is the characteristic bond energy and σ the characteristic length. The Kihira-potential does a better job for larger models such as perfluoropentane but greatly complicates the approach. The Lennard-Jones potential is used in this thesis.

The potentials are then separated into attractive and repulsive parts, ϕ_{attr} and ϕ_{rep} , respectively,

$$\phi_{\text{rep}}^{\text{WCA}}(r) = \begin{cases} \phi(r) + \varepsilon & \text{if } r < r_{\min} \\ 0 & \text{otherwise} \end{cases} \quad (2.38)$$

and

$$\phi_{\text{attr}}^{\text{WCA}}(r) = \begin{cases} -\varepsilon & \text{if } r < r_{\min} \\ \phi(r) & \text{otherwise} \end{cases} \quad (2.39)$$

where r_{\min} is the radius at which the potential is minimal.

It is useful at this stage to define the integrated strength of the attractive potential,

$$\alpha = - \iint d\mathbf{r}_i d\mathbf{r}_j \phi_{\text{attr}}(\mathbf{r}_i, \mathbf{r}_j). \quad (2.40)$$

Finally to re-establish contact with the hard sphere approximation the repulsive part of the decomposition is replaced by an infinite repulsion at a distance d . That is

$$\phi_{\text{hs}}(r) = \begin{cases} \infty & \text{if } r < d \\ 0 & \text{otherwise} \end{cases}. \quad (2.41)$$

Equation 2.36 is still exact for two particle potential theories. In order to solve it we first assume that the hard sphere potential is a function only of the local density,

$$F_{\text{hs}}[\rho] \approx \int d\mathbf{r} f_{\text{hs}}(\rho(\mathbf{r})). \quad (2.42)$$

$f_{\text{hs}}(\rho(\mathbf{r}))$ is the potential (per unit volume) of a uniform hard-sphere fluid^[24]. It is obtained from the accurate Carnahan-Stirling equation of state,

$$f_h(\rho(\mathbf{r})) = f_{\text{ideal}} + \rho k_B T \frac{4\eta - 3\eta^2}{(1-\eta)^2} \quad (2.43)$$

where $\eta = \frac{\pi\rho d^3}{6}$ is the packing function and $f_{\text{ideal}} = \rho k_B T (\ln(\rho\lambda^3) - 1)$ is the free energy (per volume) of an ideal gas. λ is the de Broglie wavelength. The approximation 2.42 is known as the *local-density approximation*.

The perturbation may be approximated by assuming that the two particle densities are uncorrelated,

$$\rho(\mathbf{r}_i, \mathbf{r}_j) \approx \rho(\mathbf{r}_i)\rho(\mathbf{r}_j). \quad (2.44)$$

This is known as the *random phase approximation*. If the medium is sufficiently large then this approximation should hold^[24]. The random phase approximation may well need to be refined for very small oil droplet in water, where the oil-water interface cannot be ignored.

Equation 2.35 can therefore be written as an explicit function of ρ ,

$$\Omega_V = \int d\mathbf{r} f_{\text{hs}}(\rho(\mathbf{r})) + \iint d\mathbf{r}_i d\mathbf{r}_j \phi_{\text{attr}}(\mathbf{r}_i, \mathbf{r}_j) \rho(\mathbf{r}_i)\rho(\mathbf{r}_j) - \mu \int d\mathbf{r} \rho(\mathbf{r}), \quad (2.45)$$

where equations 2.36, 2.42 and 2.44 have been used. Minimising 2.45 with respect to $\rho(\mathbf{r})$ gives

$$\frac{\delta f_{\text{hs}}(\rho(\mathbf{r}))}{\delta \rho(\mathbf{r})} \equiv \mu_{\text{hs}}[\rho(\mathbf{r})] = \mu - \int d\mathbf{r}' \phi_{\text{attr}}(\mathbf{r}, \mathbf{r}') \rho(\mathbf{r}'). \quad (2.46)$$

$\mu_{\text{hs}}[\rho(\mathbf{r})]$ is the chemical potential of the hard sphere fluid².

All the terms on in 2.46 can be obtained for a given function density profile. μ_{hs} on the left and the second term on the right hand side have explicit representations, while the chemical potential μ ‘mean field’ is obtained by analysing the bulk properties of the fluid. Equation 2.46 can therefore be solved by iteration. An initial guess as the density profile is given to the right hand side. The chemical potential μ_{hs} is then inverted

²The chemical potential of a hard sphere fluid is given by

$$\mu_{\text{hs}} = \frac{df_h}{d\rho} = k_B T \frac{8\eta - 9\eta^2 + 3\eta^3}{(1-\eta)^3} + k_B \ln(\rho\lambda^3) \quad (2.47)$$

(numerically) to give an improved estimate of ρ .

The density obtained by solving 2.46 is the density that minimises Ω_V , and it therefore gives the best approximation the true equilibrium grand potential. The bubble is only in thermodynamic equilibrium when it is at its critical radius. Therefore the density ρ obtained from 2.46 is the density profile of the critical bubble.

2.6.3.4 Fit the model parameters

To use equation 2.46 we need to define the free parameters in our model. There are four parameters in total, of which three are independent,

1. ε - the energy scale in the Lennard-Jones 6-12 potential (equation 2.37),
2. σ - the length scale in the Lennard-Jones 6-12 potential (equation 2.37),
3. α - the attractive strength of the Lennard-Jones 6-12 potential (equation 2.40),
4. d - The length scale in the hard-sphere model (equation 2.43).

Two of the parameters can be set by considering the bulk fluid. If the density is uniform then equation 2.45 becomes

$$\Omega_V/V = f_{\text{hs}}(\rho) - \frac{1}{2}\alpha\rho^2 - \mu\rho = p_{\text{hs}} + \mu_{\text{hs}}\rho - \frac{1}{2}\alpha\rho^2 - \mu\rho. \quad (2.48)$$

where V is the volume of the system³.

Equation 2.48 can be minimised with the help of the Maxwell relation

$$\frac{\partial p_{\text{hs}}}{\partial \rho} = \rho \frac{\partial \mu_{\text{hs}}}{\partial \rho} \quad (2.50)$$

³The hard sphere pressure is given by

$$p_{\text{hs}} = k_B T \rho \frac{1 + \eta + \eta^2 - \eta^3}{1 - \eta^3}. \quad (2.49)$$

to obtain

$$\mu = \mu_{\text{hs}} - \alpha\rho. \quad (2.51)$$

Substituting 2.51 into 2.48 gives

$$\Omega_V/V = -p_{\text{hs}}(\rho) + \frac{1}{2}\alpha\rho^2 = -p. \quad (2.52)$$

Equation 2.52 depends only on d and α .

Below the critical temperature there will be two phases in bulk coexistence. The number densities of these two phases are ρ_v and ρ_L , where the “ v ” denotes the vapour and the “ L ” denotes the liquid. At equilibrium the chemical potential and the pressures for both phases are equal

$$\mu_v = \mu_{\text{hs}}(\rho_v) - \alpha\rho_v = \mu_{\text{hs}}(\rho_L) - \alpha\rho_L = \mu_L, \quad (2.53a)$$

$$p_v = p_{\text{hs}}(\rho_v) - \frac{1}{2}\alpha\rho_v^2 = p_{\text{hs}}(\rho_L) - \frac{1}{2}\alpha\rho_L^2 = p_L. \quad (2.53b)$$

The solutions of equations 2.53 define the coexistence curve for the fluid, and they may be used to obtain the two parameters d and α .

The final parameter, σ (or equivalently ε) is obtained from the measured surface tension of the fluid. The value of Ω is obtained by iterating 2.46. The surface tension is then calculated by noting that

$$\Omega_V = \Omega_{V_l} + \Omega_{V_g} + \gamma A, \quad (2.54)$$

where Ω_{V_l} and Ω_{V_g} are the potentials of the bulk liquid and gas evaluated at the Gibbs surface, γ is the surface tension and A is the area of the surface. The value of σ is chosen so that the calculated value of γ matches its experimental value.

The code to solve these equations was written by the author of this thesis and is freely available on [github](#)^[97].

2.6.4 RESULTS OF THE DENSITY FUNCTIONAL APPROACH

2.6.4.1 *The coexistence curve*

The coexistence curve for water and perfluoropentane are plotted in Figure 2.5. The experimental values that are used to make the fit are shown with points, and the computed curve is shown with a solid line. The fit for the vapour was used to obtain d and ϵ for the model and so is by definition exact. The quality of the model can be assessed by comparing the experimental values for the liquid with the fit. It is seen to be highly accurate away from the critical point, at which point theory and experiment start to diverge.

The calculated spinodal is also plotted in Figure 2.5. The spinodal defines the point of equilibrium where the energy barrier to the transition vanishes (see Favvas^[26] for an introduction). The region of the spinodal is bound by the curves

$$\mu_v = \mu_{hs}(\rho_v) - \alpha\rho_v = \mu_{hs}(\rho_L) - \alpha\rho_L = \mu_L, \quad (2.55a)$$

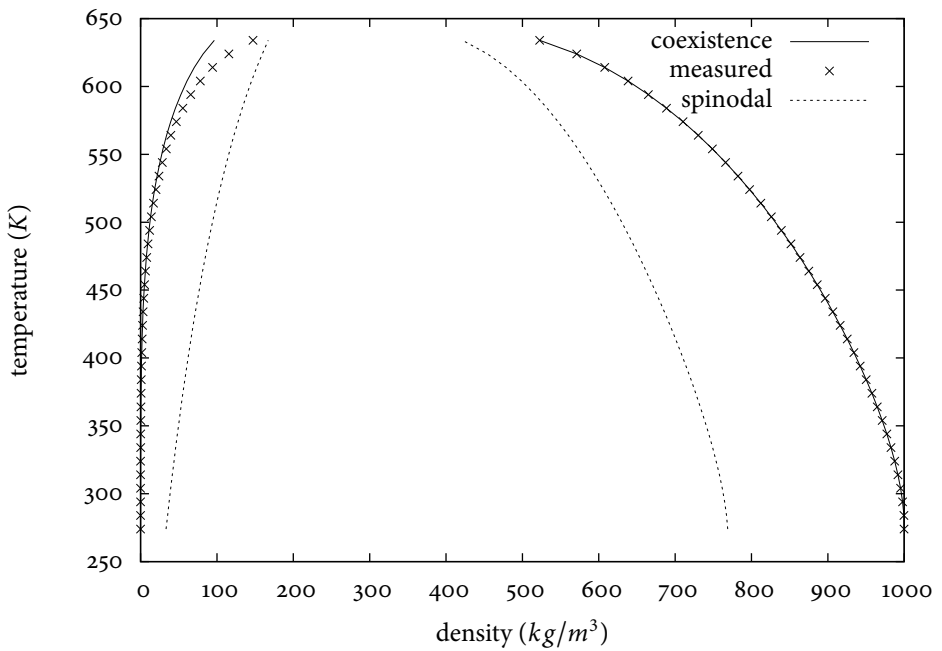
$$\frac{\partial \mu_v}{\partial \rho} = 0 \quad (2.55b)$$

$$\text{or } \frac{\partial \mu_L}{\partial \rho} = 0 \quad (2.55c)$$

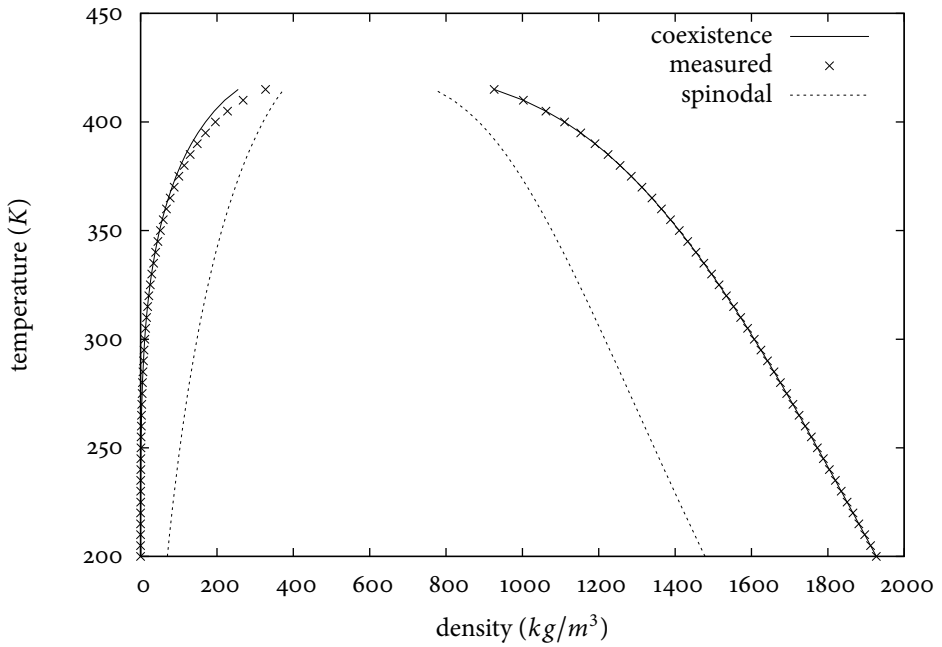
Equation 2.55a demands thermodynamic equilibrium. Equations 2.55b and 2.55c demand that the equilibrium point is a saddle point (where the energy barrier vanishes). While the decomposition of phases past the spinodal is not nucleation - the phases separate throughout the medium rather than forming a bubble - the spinodal nevertheless marks a fundamental and guaranteed change in the medium that is surely detectable.

The fitted values of d and ϵ are plotted in Figure 2.6. The stability of the parameters below the critical point is encouraging for it indicates that the predictive power of the parameters is strong. Near the critical point the curve is starting to be very sensitive changes in temperature. The model is not applicable near the critical point and its parameters are being pulled inappropriately by the changing physics.

The parameters at 20° are plotted in Table 2.4. One notable observation is that the



(a) Coexistence for water



(b) Coexistence for perfluoropentane

Figure 2.5: Coexistence and spinodal curve for water and perfluoropentane. The plot was used to obtain the temperature dependence of the parameters d and ε in the hard-sphere model with Lennard-Jones interactions.

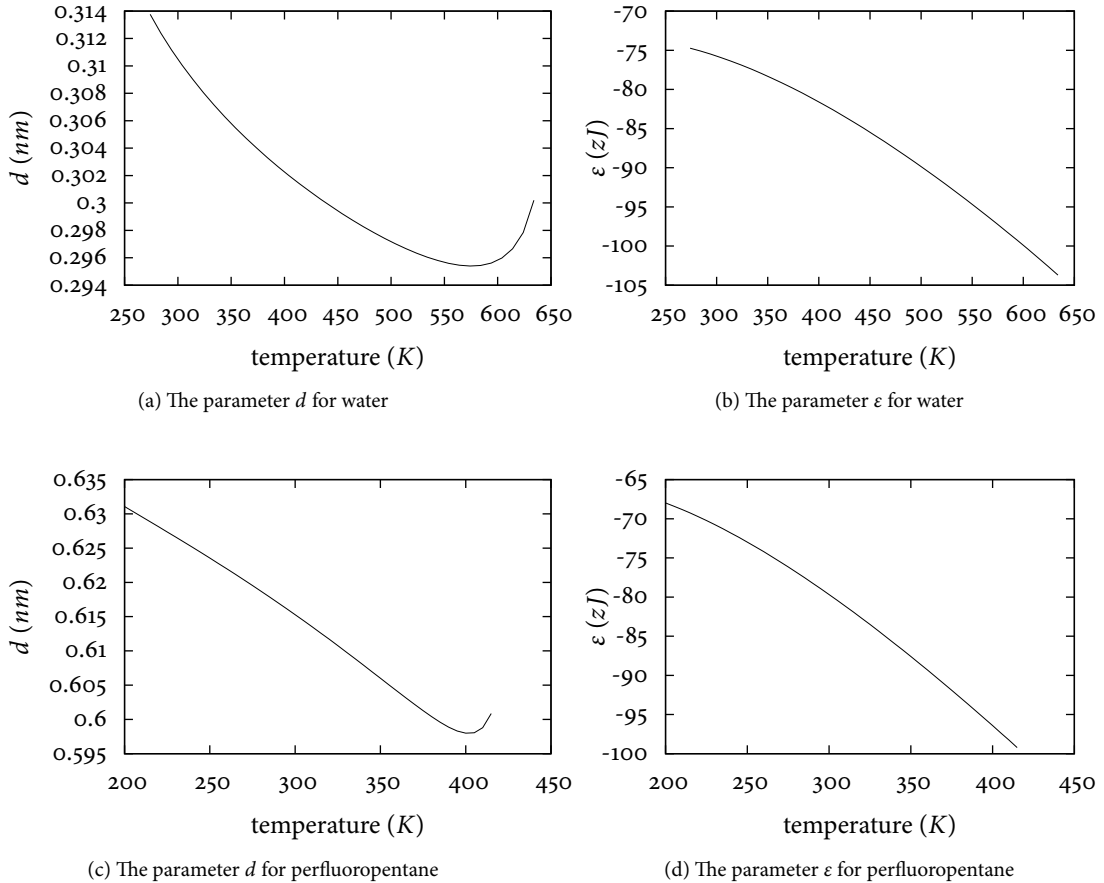
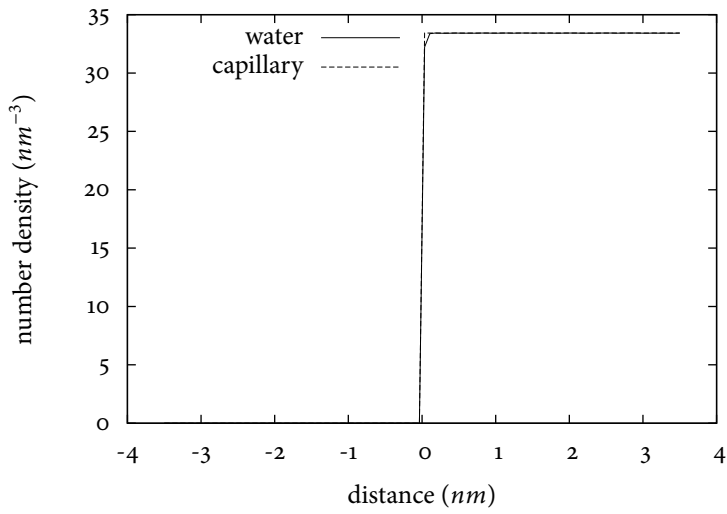


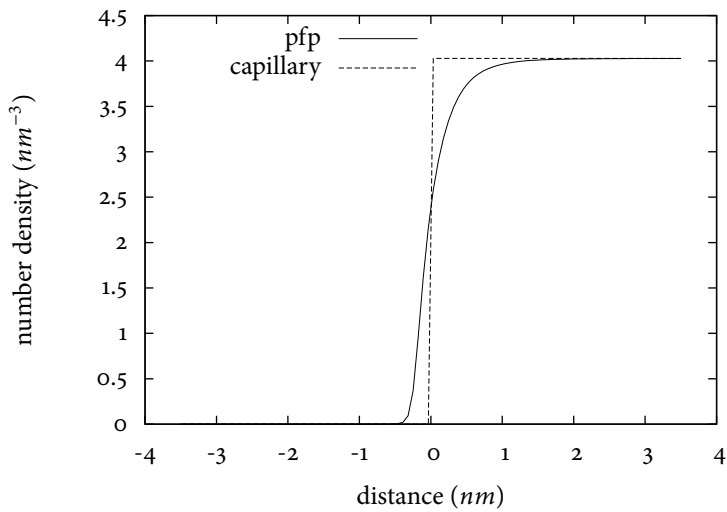
Figure 2.6: A plot of the temperature dependence of the parameters d and ε in the hard-sphere model with Lennard-Jones interactions.

Table 2.4: Density functional parameters for perfluoropentane and water at 20°

	perfluoropentane	water
ε	-80 zJ	-76 zJ
d	0.61 nm	0.31 nm
σ	0.41 nm	0.016 nm



(a) Density profile at the interface of water



(b) Density profile at the interface of perfluoropentane

Figure 2.7: The plainer density profiles of water and perfluoropentane at 293 K.

distance scale in the Lennard-Jones model is very small for water. This indicates a very low interaction length. The reason for this is the highly polar nature of water. Density functional approaches have previously been found to struggle in the presence of highly polar fluids such as water^[76,107], with the same consequence for the value of d .

In Figure 2.7 the density profiles for water and perfluoropentane are plotted. The small value of d for water means that the density profile varies over very rapidly and is essentially indistinguishable from the capillary approximation.

From Figure 2.7b it is seen that the density profile for perfluoropentane varies over a more significant length scale. The 1 nm of Figure 2.7b represents approximately 10% of the critical radius of a perfluoropentane vapour droplet under 1 MPa tension. The use of the capillary approximation for perfluoropentane is therefore highly questionable.

2.6.5 FURTHER WORK

The density profile of perfluoropentane plotted in Figure 2.7b indicates that the density functional approach may have much to offer theoretical studies of perfluoropentane.

In particular, the density functional approach can be extended to binary fluids^[107] to estimate the nucleation rates for various gases dissolved within the perfluoropentane droplet. The perfluorocarbons are remarkable for their solubility of carbon dioxide. It could be that type 1 nucleation can be facilitated by the perfluorocarbons not by their low boiling points, but rather due to the nucleation of their dissolved gases.

AN ACOUSTIC THEORY OF SPECIAL RELATIVITY

3.1 INTRODUCTION

The privileged role of light is perhaps the most mysterious aspect of Einstein's special theory of relativity. What is it about this signal, as opposed to any other method of communication, that makes it so fundamental to the concepts of time and space? The answer, for Einstein, is that light has a constant speed that is independent of the motion of the light source^[20]. This property enables the distance between an observer and a faraway object to be measured by determining the to-fro propagation time of a pulse of light. The measurement is local to the observer and all the observer requires to make the measurement is a light source, a receiver and a clock. Einstein's definition of measurement is then completed with his principle of relativity, which demands that a measuring device at rest with respect to an observer, such as a clock or a metre rule, gauge quantities that are independent of the observer's motion^[20;83].

In Einstein's theory the observer does not need to know their speed relative to the speed of the light medium - the *æther*. The postulates demand that ætherial motion neither alters the speed of light nor alters the units of the measurements used by the observer. The observer can therefore consider herself to be stationary and not consider the æther at all. This elimination of the æther, however, only emphasises the uniqueness of light, for it is the only signal that has a medium with no measurable mechanical properties. Satisfactory definitions of time and space seem to come at the expense of making light an even greater puzzle, more and more distant from the world that we can touch and

hear.

The relativity theory of Poincaré is different. For Poincaré, light does have a medium and all motions can be measured with respect to it; ‘stationary’ means stationary with respect to the æther^[83;87;88]. Unlike Einstein’s theory, the length of a measuring rod used by an observer is affected by the observers motion. Indeed, Poincaré *postulates* that it contracts from its length as measured when stationary with respect to the æther, with the size of the contraction determined by the spatial Lorentz transformation^[83;86]. It follows that the principle of relativity is also different; Poincaré assumes only that there is no absolute reference from which to measure the speed of the æther^[86]. However, Poincaré’s formulation of special relativity is not at odds with any experimental confirmation of Einstein’s theory^[82]. This is because Poincaré, like Einstein, uses the Lorentz transformations to switch between the spatial-temporal measurements of different observers, and because both theories are invariant in the quadratic form; light does have a constant speed in Poincaré’s theory of relativity^[82]. Like Einstein, Poincaré recognises that the constancy of the speed of light is a postulate. In 1898^[84] he notes that when an astronomer measures the speed of light, “He has begun by supposing that light has a constant velocity, and in particular that its velocity is the same in all directions. That is a postulate without which no measurement of this velocity could be attempted.” However, Poincaré’s theory does not depend upon this postulate, for Poincaré uses the postulated Lorentz length contraction as an alternative^[83]. Light is not a privileged signal in Poincaré’s theory but this flexibility is obtained only at the cost of admitting motion dependant deformations. A fundamental explanation for these is missing, however, and this gives Poincaré’s theory an incomplete feel.

Einstein’s theory is, of course, just as incomplete as it does not answer why light should enter, through the concepts of time and space, every physical force. With regard to this question Poincaré^[86] notes that:

Either there is nothing in the world that is not of electromagnetic origin,
or this part [the speed of light], which is common to all physical phenomena, is only an appearance, something stemming from our methods of

measurement.

Modern physical theories do not agree with the first of these options. The consequences of the second, however, are seldom addressed. In any case, when faced with a choice between the relativity theories of Einstein and Poincaré, the community choose Einstein's.

In this thesis we use sound to define time and space in the manner routinely used in medical ultrasound and other sonar-based technologies. It is demonstrated in section 3.2 that in order for ultrasound theory to agree with experiment the Lorentz transformations need to be applied. This is achieved by explicitly considering an acoustic analogue to the Michelson-Morely experiment. Since sound does have a mechanical medium through which it propagates and since ultrasound does not care about the speed of light it is the relativity theory of Poincaré that is recovered in acoustics. It is demonstrated in section 3.2 that Poincaré's motion dependent contraction results from the dependence of the sound speed on the bulk flow of the medium. The contraction is real in the sense that it is measured. However, since the contraction results from the measurement process there is no need to seek some fundamental interaction between material objects and their æther.

In section 3.3 it is demonstrated that when time and space are defined with sound, the acoustics of an ideal fluid obey the same relations as Maxwell's formulation of electromagnetism. Therefore the generation and propagation of sound, when time and space are defined with sound, obey the same physical laws as the generation and propagation of light, when time and space are defined with light.

3.2 THE ACOUSTIC DEFINITION OF TIME AND SPACE

In medical ultrasound distances are measured using the time it takes a pulse of sound to propagate from a transducer to a reflecting object and then to return again. If the sound is emitted from the transducer at a time, τ^- , and the sound returns at a time, τ^+ , then the task is to find from these two numbers the spatio-temporal location, x , of the

point of reflection.

What happens to the sound in between leaving the transducer and returning cannot be known by acoustic measurement. In this ignorance ultrasound practitioners assume that the time at which the echo occurred is the midpoint of τ^- and τ^+ ,

$$\tau(x) = \frac{\tau^+ + \tau^-}{2}. \quad (3.1a)$$

Other choices could certainly be made, but would imply a knowledge of the world beyond that learnt from τ^- and τ^+ alone. To measure distances from the times τ^- and τ^+ a sound speed, c , is required. Assuming, again in ignorance, that the sound returns at the same speed at which it left gives

$$\rho(x) = \frac{\tau^+ - \tau^-}{2} c. \quad (3.1b)$$

These are the definitions of time and space that are used in ultrasound. They are also identical to definitions used by Poincaré^[83;87] and Einstein^[18;20] with the exception that the speed, c , is here the speed of sound rather than the speed of light.

Equation 3.1b requires an *a priori* knowledge of the sound speed for otherwise distances cannot be determined from temporal measurements. In diagnostic ultrasound scanners this speed is usually taken to be 1540 ms^{-1} . The constancy of the speed of sound is identical to Einstein's second postulate for special relativity^[20], except that the sound speed takes the role of the speed of light. However, the speed of sound is here a constant not because of some physical law but because when using sound to make measurements there is no other choice but to assume the sound speeds constancy. As discussed in the introduction, this conforms more to Poincaré's view of the light postulate than to Einstein's.

Ultrasound has inherited from fluid mechanics the principle that it is impossible to determine absolute uniform motions: an object at rest in a laminar flow is equivalent to an object moving uniformly in a stationary fluid. The velocity of an object within a fluid, or even the velocity of parts of the fluid itself, may always be measured with respect to

the bulk flow of the fluid. The notion of a true speed with respect to some absolute reference is never invoked. This is the relativity postulate as envisaged by Poincaré.

3.2.1 PHYSICAL THEORIES THAT ARE TO BE TESTED WITH ULTRASOUND

The measurement rules of equations 3.1a and 3.1b enable two properties of the world as measured by ultrasound to be stated immediately. The first is that an entity that moves away from the transducer at a speed that is faster than the speed of sound (with respect to the bulk flow of the medium) cannot be measured. This is not because such motions are impossible but because the sound will never catch up with the entity and so there will never be an echo to record.

The second is that ultrasound is not capable of measuring variations in the speed of sound. Since the sound speed must be known before any distance can be measured, changes in the sound speed cannot be measured. Changes may only be determined with additional *a priori* knowledge of the structure of the medium. In acoustics, when distances and times are measured with light, fluctuations in a medium's density result in fluctuations in the speed of sound, and since sound is itself a fluctuation in density, non-linear sound speeds result in compressible mediums. But these fluctuations cannot be measured with ultrasound, and it follows that the acoustic medium must be incompressible (in the relativistic sense^[80;81;108]) and that sound must propagate according to a linear wave equation. In section 3.3 it is demonstrated that this linear relation is identical to Maxwell's relation of electromagnetism.

The ultrasound literature does not comply with these remarks. Currently, when modelling an ultrasound experiment, a fluid medium is always described by a Galilean invariant theory such as Euler's equation or the Naiver-Stokes equation. The resulting model is then capable of predicting motions that are faster than the speed of sound and predicts that a sound pulse propagates according to a non-linear wave equation. Both of these predictions are impossible when the world is measured with sound. The ultrasound literature fails to recognise the distinction between two equally valid descriptions of the world - the world that is seen and the world that is heard. Curiously,

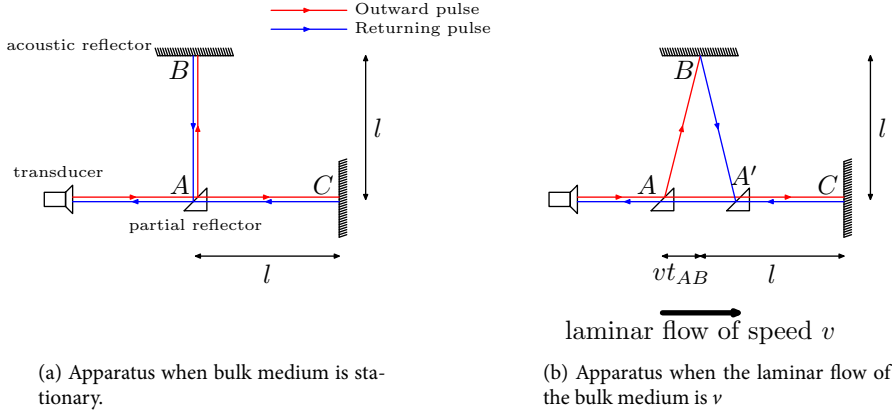


Figure 3.1: A pulse-echo experiment when there is, and is not, a relative laminar flow past the apparatus.

ultrasound physics repeats the fallacy that the world must be seen to be believed.

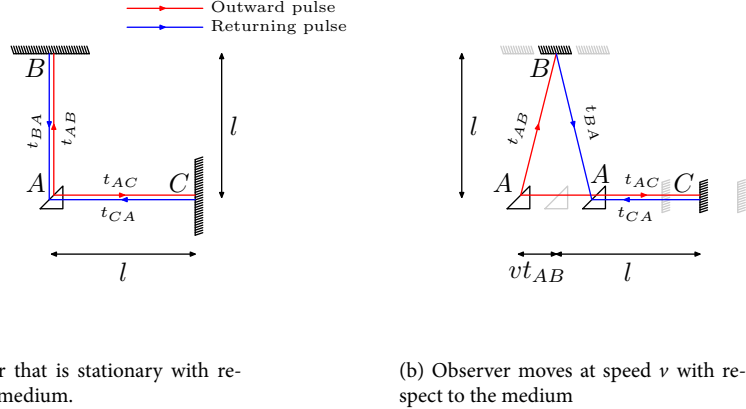
3.2.2 AN ACOUSTIC MICHELSON-MORELY EXPERIMENT.

The discussion so far has been somewhat abstract. To make it concrete it is useful to discuss a simple pulse-echo experiment and compare the two viewpoints - the Galilean¹ world that is *seen*, with the world that is measured with ultrasound.

The first case to be considered is illustrated in Figure 3.1a. This apparatus is appropriate when the equipment is stationary with respect to the bulk flow of the medium. It is analogous to Michelson and Morely's famous experiment: a piezoelectric transducer replaces both the light source and the receiver while a medium that partially reflects sound replaces the semi-silvered mirror. The distance between A and B is denoted l and is the same as the distance between A and C . In the following the time it takes for the sound to propagate from A to B and back again is compared with the to-fro times between A and C .

If the apparatus of Figure 3.1a were not stationary with respect to the bulk flow of the medium then the experiment would fail. This is because the sound would not travel from A to B and return; the motion of the medium would drag the sound pulse with

¹Formally the 'Galilean' measurements are the distances and times that are measured with light signals in accordance to Einstein's method [20]. In ultrasound experiments, however, the Galilean approximation is entirely appropriate.



(a) Observer that is stationary with respect to the medium.

(b) Observer moves at speed v with respect to the medium

Figure 3.2: Observed motion of apparatus for the setup of Figure 3.1a.

it. The setup illustrated in Figure 3.1b gives spirit of the Michelson-Morely experiment for the case when the apparatus is not stationary with respect to the bulk flow. In this case there are two separate partially reflecting surfaces. The time it takes the sound to propagate from A to B to A' is now compared with the time it takes the sound to go from A to C to A' .

When the to-fro times along the two arms are the same, irrespective of the flow of the bulk medium, the result is described as *null*. This is in accordance to the description of the Michelson-Morely result.

3.2.2.1 A Galilean interpretation

First we consider the case of the apparatus being stationary with respect to the bulk flow (Figure 3.1a). If the propagation of the sound pulse were observed by a Galilean observer that is also stationary with respect to the flow then she would observe the sound travelling according to Figure 3.2a. The time, t_{AB} , it takes for the sound to propagate from A to B is the same as the time, t_{BA} , it takes the sound to propagate from B to A . It is given by l/c , where c is the speed of sound of the medium. This time interval is the same for the to and fro paths between A and C ,

$$t_{AB} = t_{BA} = t_{AC} = t_{CA} = l/c. \quad (3.2)$$

An observer for whom both the medium and apparatus flow past at a speed, v , will measure the same time intervals but will witness an altogether more complicated experiment. The acoustic paths that will be observed are illustrated in Figure 3.2b. When the sound travels between A and B the observer will record that the sound travels at an effective speed of

$$c_{\text{eff}}(v) = \sqrt{c^2 + v^2}. \quad (3.3)$$

This is due to the contribution of the laminar flow. Additionally, the measured distance between A and B will be greater by $\sqrt{l^2 + v^2 t_{AB}^2}$. The increased distance and increased speed cancel so that

$$t_{AB} = t_{BA} = \frac{\sqrt{l^2 + v^2 t_{AB}^2}}{\sqrt{c^2 + v^2}} = \frac{l}{c}, \quad (3.4)$$

as before.

The bulk flow will also contribute to the effective speed of the pulse from A to C ($c_{\text{eff}} = c + v$) and hinder the return from C to A ($c_{\text{eff}} = c - v$). However, this is again exactly compensated by changes in the total distance that the moving observer measures. As is illustrated in Figure 3.2b, the total distance from A to C is $l + vt$. When the sound travels from C to A the total distance is $l - vt$. Therefore the measured times are

$$t_{AC} = \frac{l + vt_{AC}}{c + v} = t_{CA} = \frac{l - vt_{CA}}{c - v} = \frac{l}{c}. \quad (3.5)$$

Next, we must check that these timings still hold when the apparatus is moving with respect to the medium (Figure 3.1b). The equivalence of Figure 3.1b and Figure 3.2b demonstrates this. An observer that is stationary with respect to the apparatus (and moving with a speed, v , with respect to the medium) will record,

$$t_{AB} = t_{BA'} = \frac{\sqrt{l^2 + v^2 t_{AB}^2}}{\sqrt{c^2 + v^2}} = \frac{l}{c}, \quad (3.6)$$

and

$$t_{AC} = \frac{l + vt_{AC}}{c + v} = t_{CA'} = \frac{l - vt_{CA'}}{c - v} = \frac{l}{c}. \quad (3.7)$$

Equations 3.6 and 3.7 are exactly the same results as equations 3.4 and 3.5, respectively. If the observer is instead stationary with respect to medium then it is easy to see that equations 3.2 are repeated.

In summary, we find that the time it takes the sound to propagate from A to B and back again is identical to the time it takes the sound to propagate from A to C and back, irrespective of the speed of the observer with respect to the medium. The acoustic Michelson-Morely experiment should yield a *null* result.

3.2.2.2 An acoustic interpretation

Unlike the Galilean observer, the ultrasound physicist cannot directly measure the propagation of sound. The sound path of a pulse-echo experiment must be inferred afterwards from the measurements and the definitions of equation 3.1. In order to predict a sound path the ultrasound physicist must have further *a priori* knowledge, which we assume here to be the dimensions of the apparatus.

Let us again consider the experiment of Figure 3.1a, where all the apparatus is stationary with respect to the bulk flow of the fluid. The sound path illustrated in Figure 3.2a is the simplest through the apparatus and we assume that this path is predicted. To test this prediction the ultrasound physicist measures the to-fro times between A and B and between A and C . Both of these times are equal to $2l/c$ (equation 3.2), which is consistent with the known lengths, l . The predicted sound paths are to this extent confirmed.

Let us now suppose that the same setup is measured by a transducer that moves uniformly at a speed, v , with respect to the medium and apparatus. Again with knowledge of the apparatus, we assume that the ultrasound physicist predicts the simplest path. This is the path illustrated in Figure 3.2b and is the same path that is measured by the

moving Galilean observer. A difference from the Galilean case arises, however, because the predicted path is subject to the rules of the measurement system and, for the ultrasound physicist, sound always propagates at a constant speed, c . For the propagation time between A and B the ultrasound physicist therefore predicts (c.f. equation 3.4)

$$t_{AB} = t_{BA} = \frac{\sqrt{l^2 + v^2 t_{BA}^2}}{c} \implies t_{AB} = t_{BA} = \frac{1}{\sqrt{1 - v^2/c^2}} \frac{l}{c}. \quad (3.8)$$

For the sound pulse between A and C they predict

$$t_{AC} = \frac{l + vt_{AC}}{c} \implies t_{AC} = \frac{l}{c - v} \quad (3.9a)$$

and

$$t_{CA} = \frac{l - vt_{CA}}{c} \implies t_{CA} = \frac{l}{c + v} \quad (3.9b)$$

rather than equation 3.5. Therefore the total to-fro time between A and C is predicted to be

$$t_{AC} + t_{CA'} = \frac{1}{1 - v^2/c^2} \frac{2l}{c}. \quad (3.10)$$

These predictions are of course wrong. Equation 3.8 and 3.10 do not agree with the experimentally measured intervals. The reassignment $c_{\text{eff}} \rightarrow c$ made by the ultrasound physicist has resulted in predicting time intervals for the sound to traverse between A and B and between A and C that are too large by a factor of γ and γ^2 respectively, where

$$\gamma = \frac{1}{\sqrt{1 - v^2/c^2}} \quad (3.11)$$

is the Lorentz factor. Moreover, the to-fro time between A and B is not predicted to equal the to-fro time between A and C , in contradiction to the experimental result. This predicament faced by the ultrasound physicist is, of course, the same as that which faced Lorentz, Poincaré and Einstein at the beginning of the twentieth century.

The error is clear to the Galilean observer: the ultrasound physicist has been forced by the measurement process to set the effective speed of sound to equal c . To solve the problem the ultrasound physicist must compensate for the wrong sound speed by rescaling the temporal and spatial units used when modelling.

The ultrasound physicist, who cannot measure variations in the sound speed, must work a little harder to come to this conclusion. The first explanation that they might try is to doubt the apparatus. If the distance between A and C was actually a factor of γ^2 shorter than the manufacture claimed then the predicted time for that path would match the experimentally measured value. Likewise, all would be well if the distance between A and B was shorter by a factor of γ . However, this explanation can be shown to be incorrect by counting the number of cycles of the sound wave that propagate through each arm of the apparatus. This can be done straight-forwardly with ultrasound, the pulse length is simply increased until the received signal starts to interfere with the emitted signal. The experimental result would be that $n = 2l/(cT)$ cycles fit both between A and B and between A and C , where T is the period of the sound wave. This result implies that the distance between A and C is not simply shorter than between A and B , for then the number of cycles along each path would be different. Rather, it implies that *all* distances are shorter in the A - C direction, including the wavelength of the sound wave. That is, parallel to the motion the *unit of distance* is contracted by a factor of γ .

If the ultrasound physicist incorporates the number of pulses into equation 3.8 then they would predict that the period between A and B is

$$T_{\text{us}} = \gamma \frac{l/n}{c} = \gamma T, \quad (3.12)$$

where T_{us} distinguishes the predicted period from the experimentally measured period T . That is to say, the *unit of time* used in the model must be scaled by a factor of γ in order to agree with experiment.

As before, the equivalence of Figure 3.1b and Figure 3.2b guarantee that the same con-

clusion would be drawn when the apparatus is not stationary with respect to the bulk flow.

The comparison between the Galilean and experimental observer can be summarised as follows: when modelling an ultrasound experiment the unit of distance used in the model must be contracted by the Lorentz factor in order to agree with experimental results, and likewise the unit of time must be reduced by the Lorentz factor. These are the results of Poincaré's special relativity. Poincaré's postulated contraction in length is the manifestation of the dependence of the sound speed upon the flow of the medium. It exists because the speed of a signal that is used to measure distances must be assumed to be a constant, not because the speed is constant but because distances cannot be measured otherwise.

3.3 ACOUSTICS WHEN THE MEASUREMENTS ARE MADE WITH ULTRASOUND

Sound does have a medium through which it propagates. To demonstrate the role of the medium we formulate the acoustics of an ideal fluid that is measured with ultrasound, where the motions of the fluid are understood to be local perturbations to the bulk flow. It is shown in section 3.3.1 that the acoustics obey the same law as Maxwell's equations of electromagnetism. The derivation is direct but the co-variant notation makes the comparison to conventional acoustics difficult. In section 3.3.2 Maxwell's relations are re-derived in the spirit of Lighthill's formulation of aeroacoustics. In doing so the acoustic analogues to the electric and magnetic field are obtained.

A model that is to be compared to ultrasound measurements must be Lorentz invariant. This condition is automatically fulfilled when the equations of fluid motion are obtained from the divergence of the energy-momentum tensor of an ideal fluid. The condition that the sound speed takes the role of the speed of light is enforced by simply equating these two speeds. This further requires that the energy density of the fluid, as measured acoustically, be a function of the pressure only (barotropic), for the sound speed cannot be set equal to the speed of light otherwise^[108].

The complete analogy between an incompressible relativistic fluid and electromag-

netism was first published in French by Garrido^[31] in 1982. The results were unknown to the author of this thesis, who derived the results of the following section independently.

This section makes use of Geometric Algebra^[19;39] for the derivation. However, due to the importance of the section the derivation is repeated in tensor algebra in Appendix A.

3.3.1 THE ACOUSTICS ANALOGUE TO MAXWELL'S RELATION

The energy-momentum tensor of an ideal fluid is^[60;108]

$$T(a) = (\varepsilon + p)a \cdot uu - ap, \quad (3.13)$$

where, $\varepsilon \equiv \varepsilon(p)$ is the barotropic total energy density, p is the pressure and u is the velocity vector of the spacetime path, with the parametrisation chosen such that $u^2 = 1$. That is, the units of length and time are chosen so that velocity of sound is set to unity.

The speed of sound, c , given at constant entropy density, σ , is^[60;108]

$$c^2 = \left. \frac{\partial p}{\partial \varepsilon} \right|_{\sigma}. \quad (3.14)$$

This is the same as the non-relativistic expression except that the energy density has replaced the mass density.

In this chapter we shall consider the equation of state

$$\varepsilon(p) = p, \quad (3.15)$$

which describes an incompressible relativistic fluid. Equation 3.15 was first studied by Taub^[108].

Applying 3.15 to 3.13 simplifies the energy momentum tensor,

$$T(a) = p(2a \cdot uu - a) \equiv \frac{\Xi_0^2}{4} AaA, \quad (3.16)$$

where the geometric dot-product has been used and the vector potential, A , satisfies

$$A = 2\frac{1}{\Xi_0} p^{1/2} u = 2\frac{1}{\Xi_0} \varepsilon^{1/2} u. \quad (3.17)$$

The constant scale-factor, Ξ_0 , is determined from the ambient proper number density of the fluid, n_0 , and the ambient pressure, p_0 , as follows,

$$\Xi_0 = \frac{n_0}{\sqrt{p_0}}. \quad (3.18)$$

The motivation for introducing the 4-vector A is that it represents a potential flow. To demonstrate this, we first note that the relativistic generalisation to the velocity potential, ψ , is defined^[60] by

$$\nabla \psi = -\frac{\varepsilon + p}{n} v = -\frac{2\varepsilon}{n} v, \quad (3.19)$$

where ∇ is the vector derivative and n is the proper particle number density of the fluid. Equation 3.15 has been used to obtain the second equality. To show that this is equal to the negative of the potential A , we use a thermodynamic argument given by Taub^[108]. The internal energy density, ε , is equal to the sum of the rest mass and the internal energy per particle^[60;108], e ,

$$\varepsilon(p) = nm(1 + e(p)), \quad (3.20)$$

where m is the particle mass at rest. From the isentropic thermodynamic relation $mde = -pd\left(\frac{1}{n}\right)$ it follows that

$$nd\varepsilon = \varepsilon dn - n^2 pd\left(\frac{1}{n}\right) = (\varepsilon + p) dn. \quad (3.21)$$

Applying equation 3.15 and integrating we obtain

$$n = \Xi_0 \sqrt{p}, \quad (3.22)$$

where Ξ_0 is the constant introduced in 3.18. With the aid of equation 3.15 it follows that

$$A = 2 \frac{1}{\Xi_0} \sqrt{p} u = \frac{\varepsilon + p}{n} u = -\nabla \psi, \quad (3.23)$$

as asserted.

In the absence of external fields, the equations of motion are obtained by setting the divergence of the energy momentum tensor (equation 3.16) to zero. By projecting the divergence of 3.16 along the timelike component we find

$$u \cdot \tilde{T}(\tilde{\nabla}) = \frac{1}{2} \Xi_0^2 u \cdot A \nabla \cdot A = 0. \quad (3.24)$$

Since, from 3.17, the vector A is parallel to u it follows that

$$\nabla \cdot A = 0 \quad (3.25)$$

and so the vector potential A is conserved. The spacelike projection, $\tilde{T}(\tilde{\nabla}) - uu \cdot \tilde{T}(\tilde{\nabla})$, gives in turn,

$$u \cdot (\nabla \wedge A) = 0. \quad (3.26)$$

The relativistic vorticity bivector, F , is the exterior derivative of the vector potential,

$$F = \nabla \wedge A, \quad (3.27)$$

and so 3.26 implies that the vorticity tensor is orthogonal to the velocity.

By taking the divergence of 3.27 and using 3.25 it follows that

$$\nabla^2 A = \nabla \cdot F = \nabla F. \quad (3.28)$$

The left-hand-side of equation 3.28 is a wave equation and so we interpret the right-hand-side as an acoustic source, a 4-current, J . Therefore

$$\nabla F = J. \quad (3.29)$$

Equation 3.29 is Maxwell's equation. It is the expressiveness of Geometric Algebra enable it to be condensed into a single equation. The two equations familiar from tensor algebra are

$$\nabla \cdot F = J \quad (3.30a)$$

and

$$\nabla \wedge F = 0. \quad (3.30b)$$

Equation 3.25 has specified the Lorenz gauge.

As is well known, Maxwell's relations are invariant to a gauge transformations of the form

$$A' = A - \nabla \psi, \quad (3.31)$$

This transformation is equivalent to the addition of a potential flow to the equations. However, in equation 3.23 the vector potential was already interpreted as a potential flow. The gauge invariance is therefore the very same as the required invariance to the bulk flow of the medium. It is the manifestation of the Poincaré relativity postulate.

3.3.2 THE ACOUSTIC ANALOGUES TO THE ELECTRIC AND MAGNETIC FIELDS

In classical electromagnetism the electric and magnetic fields are 3-dimensional vector fields that are (usually) measured in the laboratory frame. Such spatial vector quantities are denoted in bold in this section.

The most direct method of obtaining the acoustic analogues to the electric and magnetic fields is to project the vorticity tensor, F , into the laboratory frame^[19;38]. The analogue to the electric field can then be defined to be the timelike component, and the analogue to the magnetic field the spacelike component^[38]. The directness of this method, however, comes at the cost of it bearing little resemblance to conventional acoustics.

To demonstrate the similarities and the differences between the ultrasonic and the Galilean formulations of acoustics we re-derive Maxwell's relations using a relativistic version of Lighthill's formulation of aeroacoustics^[62]. The analogues to the electric and magnetic field become clear in this process. To aid the comparison, in this section we revert to S.I. units and so the speed of sound will again be denoted c .

We start by projecting the temporal and spatial equations of motion, equations 3.25 and 3.26, into the laboratory frame. The result is

$$\nabla \cdot \mathbf{A} = -\frac{1}{c} \partial_t \phi, \quad (3.32a)$$

$$\partial_t \mathbf{A} - \mathbf{v} \times (\nabla \times \mathbf{A}) = -\nabla \phi. \quad (3.32b)$$

$\partial_t \equiv \frac{\partial}{\partial t}$ and ∇ is the spatial vector derivative; ϕ/c and \mathbf{A} are the temporal and spatial components of the vector potential A , such that

$$\phi \equiv 2\gamma \frac{1}{\Xi_0} \sqrt{p} \quad \text{and} \quad \mathbf{A} \equiv \frac{1}{c^2} \phi \mathbf{v}, \quad (3.33)$$

where \mathbf{v} is the velocity of the fluid as measured in the laboratory frame and $\gamma = (1 - \mathbf{v}^2/c^2)^{-1}$, as in 3.11.

The potential ϕ may be interpreted as the relativistic total enthalpy multiplied by the

particle mass. To see this we first introduce the non-relativistic enthalpy, h , which is defined by

$$h \equiv e + p/(nm). \quad (3.34)$$

It then follows that

$$\phi = \gamma \frac{\varepsilon + P}{n} = \gamma m (c^2 + h). \quad (3.35)$$

In the non-relativistic limit this becomes

$$\phi \rightarrow \left(1 + \frac{1}{2} \frac{v^2}{c^2}\right) (mc^2 + mh) = mc^2 + \frac{1}{2} mv^2 + mh \quad \text{as } v/c \rightarrow 0. \quad (3.36)$$

The term $h + \frac{1}{2}v^2$ is the usual expression of the total enthalpy. Equation 3.36 multiplies this by the particle mass, m , and adds the rest energy, mc^2 , which is absent from all non-relativistic thermodynamics.

Equations 3.32a and 3.32b are the acoustically measured versions of the continuity and Euler equations. In the non-relativistic limit the equations reduce to Galilean invariant forms,

$$\nabla \cdot \mathbf{v} = 0, \quad (3.37a)$$

$$\partial_t \mathbf{v} - \mathbf{v} \times (\nabla \times \mathbf{v}) = -\nabla \left(\frac{1}{2}v^2 + h\right). \quad (3.37b)$$

Equation 3.37b is the incompressible version of Euler's equation written in Crocco's form^[42] and Equation 3.37a is the continuity equation of an incompressible fluid.

With the continuity and Euler equation that are valid for acoustic measurements now available, we may apply them to the conventional formulations of acoustics. We proceed with Lighthill's acoustic analogy^[42;62]. To do so we differentiate the continuity equation (equation 3.32a) with respect to time and subtract it from the spatial derivative of Euler's equation (equation 3.32b). A wave equation for the total enthalpy results

$$\left(\nabla^2 - \frac{1}{c^2} \partial_t^2\right) \phi = \nabla \cdot (\mathbf{v} \times (\nabla \times \mathbf{A})). \quad (3.38a)$$

Next, a wave equation for \mathbf{A} is obtained by differentiating the continuity equation with respect to space and then subtracting the result from the temporal derivative of Euler's equation,

$$(\nabla^2 - \frac{1}{c^2} \partial_t^2) \mathbf{A} = -\nabla \times (\nabla \times \mathbf{A}) - \frac{1}{c^2} \partial_t (\mathbf{v} \times (\nabla \times \mathbf{A})). \quad (3.38b)$$

For comparison, had we carried out this procedure with the Galilean invariant continuity and Euler equation (not the incompressible versions) we would have obtained^[42],

$$\left[D_t \left(\frac{1}{c^2} D_t \right) - \frac{1}{\rho} \nabla \cdot (\rho \nabla) \right] \left(\frac{1}{2} v^2 + h \right) = -\frac{1}{\rho} \nabla \cdot (\rho \mathbf{v} \times (\nabla \times \mathbf{v})) \quad (3.39a)$$

$$\left[D_t \left(\frac{1}{c^2} D_t \right) - \frac{1}{\rho} \nabla \cdot (\rho \nabla) \right] \mathbf{v} = \frac{1}{\rho} \nabla \times (\rho \nabla \times \mathbf{v}), \quad (3.39b)$$

where $D_t \equiv \partial_t + \mathbf{v} \cdot \nabla$. The equations of 3.39 express Lighthill's analogy in terms of enthalpy and vorticity^[42]. The left hand side of both describe a non-linear wave in homoentropic potential flow^[42].

In keeping with Lighthill's acoustic analogy, we interpret the right hand side of 3.38a and 3.38b as the fluctuations generated by the acoustic sources. If the magnitude of the fluctuations is proportional to the density of the acoustic sources, ρ_q , then we may define the constant of proportionality, ξ_0 , so that

$$\nabla \cdot (\mathbf{v} \times (\nabla \times \mathbf{A})) \equiv -\frac{\rho_q}{\xi_0}. \quad (3.40a)$$

Likewise, we may define an acoustic current, $\mathbf{J} = \rho_q \mathbf{v}$, by

$$\nabla \times (\nabla \times \mathbf{A}) + \frac{1}{c^2} \partial_t (\mathbf{v} \times (\nabla \times \mathbf{A})) \equiv \mu_0 \mathbf{J}, \quad (3.40b)$$

where μ_0 is again the constant of proportionality. If the acoustic current is conserved then it follows that the two constants are related:

$$c^2 = \frac{1}{\xi_0 \mu_0}. \quad (3.41)$$

In the rest of this chapter we assume this to be the case.

This section is completed by noting that equations 3.40a and 3.40b can be simplified by introducing

$$\mathbf{E} = -\mathbf{v} \times (\nabla \times \mathbf{A}) \quad \text{and} \quad \mathbf{B} = \nabla \times \mathbf{A}, \quad (3.42)$$

so that

$$\left(\nabla^2 - \frac{1}{c^2} \partial_t^2 \right) \phi = -\nabla \cdot \mathbf{E} \equiv -\frac{\rho_q}{\xi_0} \quad (3.43a)$$

and

$$\left(\nabla^2 - \frac{1}{c^2} \partial_t^2 \right) \mathbf{A} = -\nabla \times \mathbf{B} + \frac{1}{c^2} \partial_t \mathbf{E} \equiv -\mu_0 \mathbf{J}. \quad (3.43b)$$

The equations of 3.43 are the same as Maxwell's equations of electromagnetism when written in terms of the potentials in the Lorenz gauge^[19] (equation 3.32a). The vector \mathbf{E} is known as the Lamb vector and is proportional to the Coriolis acceleration; it takes the role of the electric field in the analogy. The axial vector \mathbf{B} is the spatial vorticity and takes the role of the magnetic field. The constants ξ_0 and μ_0 are, respectively, the analogues of the permittivity and permeability of free space.

Writing out Maxwell's 4 equations explicitly gives

$$\nabla \cdot \mathbf{E} = \frac{\rho_q}{\xi_0}, \quad (3.44a)$$

$$\nabla \times \mathbf{B} = \mu_0 \mathbf{J} + \frac{1}{c^2} \partial_t \mathbf{E}, \quad (3.44b)$$

$$\nabla \times \mathbf{E} = -\partial_t \mathbf{B}, \quad (3.44c)$$

$$\nabla \cdot \mathbf{B} = 0. \quad (3.44d)$$

The acoustic interpretation of these equations are as follows:

1. Equation 3.44a is the definition of an acoustic source density.
2. Equation 3.44b is the definition of the acoustic current density.
3. Equation 3.44c is the Lorentz invariant version of the vorticity equation.
4. Equation 3.44d is an expression of Helmholtz theorem, which demands the conservation of vorticity.

3.4 DISCUSSION

In the physics community there is a widespread misconception that relativistic corrections only become important when predicting motions that are close to the speed of light. This is due, perhaps, to the explicit reference to light made in Einstein's postulates of special relativity, or due to Einstein's elimination of the æther. There is an impression that the postulated properties of light, its constancy of speed and lack of medium, are unique and enable light alone to be used to define distances.

In this chapter it has been demonstrated that when distances are measured by acoustic pulse-echo, relativistic corrections must be used to correctly predict motions that are close to the speed of sound. Ultrasound, as well as other sonar-based technologies, is a relativistic subject where the speed of sound takes the role of the speed of light. Furthermore, it has been demonstrated that when distances are measured with ultrasound, the generation and propagation of sound in an ideal homentropic fluid obeys

Maxwell's equations, the physical law that describes the generation and propagation of light. This fundamentally relativistic theory is completely unaltered when the speed of sound takes the role of the speed of light.

The implication is that relativistic theories *in general* are not dependant upon the speed of light. That, in principle, *any* propagating signal could be used to make the measurement, and therefore that *all* relativistic theories have an acoustic analogue. This is because to measure distances from the to-fro propagation time of a signal, a constant propagation speed must be assumed. Moreover, the constancy of the speed can never be experimentally refuted: you cannot use light signals to measure fluctuations in the speed of light; you cannot use sound signals to measure fluctuations in the speed of sound; how a signal actually traverses its medium can never be determined without knowing beforehand the world that is to be measured. The Lorentz transformations arise from the difference between the assumed speed of sound that is required to measure distance, and the effective speed of the sound that is altered by motion of the medium. It is wrong to say that motion faster than the speed of light is impossible, just as it wrong to say that motion faster than the speed of sound is impossible. All that can be said is that motions that are faster than the propagating signal cannot be measured.

The æther does have a role in the relativity theory used in this report: sound does have a propagating medium. However, the æther is relativistic in the sense that it does not define a state of absolute rest. Moreover, it was shown that gauge invariance in Maxwell's relations may be interpreted as an invariance to the potential flow of the medium. This global gauge invariance is the same condition as the requirement that the æther be invariant to uniform motions. The relativity theory used in this report is therefore that of Poincaré, rather than Einstein. Indeed, as was noted in the introduction, the central argument of this report, that the constancy of the speed of light and the resulting Lorentz transformations result entirely from the method of measurement, was suggested by Poincaré in 1906^[86]. Unfortunately, however, Poincaré's contribution to the theory of relativity has been largely ignored by the wider community.

3.4.1 ON THE ABSENCE OF NON-LINEAR PROPAGATION

In this report we have demonstrated that when time and space are measured acoustically the propagation of sound is linear. However, this is at odds with the understanding in medical ultrasound that the non-linear propagation of an acoustic pulse is not only measurable but also important. Our task is to explain how the non-linearity found in other measurement systems manifests itself in acoustic measurements. To do so it is useful to frame the discussion around the linear equations of 3.38, which are appropriate when distances are measured acoustically, and their non-linear Galilean forms of 3.39.

The first point to note is that the non-linearity of the Galilean formulation of sound is entirely a matter of *convention*. It would in fact be more appropriate to rewrite equations 3.39 as linear wave equations with everything else interpreted as acoustic sources and currents. Then the sound is defined as the part of an acoustic disturbance that can propagate energy away to infinity; the rest of the disturbance being a ‘local’ source. This is, in fact, the usual final step of Lighthill’s analogy. The reason it is rarely performed when the analogy is written in terms of the total enthalpy and vorticity is because the acoustic source terms become horribly complicated. The split of source and wave in 3.39 is convenient interpretatively, but is nevertheless rather ad-hoc, for it mixes local terms with those that can propagate indefinitely.

The influence of non-linear propagation on what can be measured acoustically is found by comparing the right hand sides of equations 3.38 and equations 3.39. It is seen that the only major difference between the two is the term

$$-\frac{1}{c^2} \partial_t (\mathbf{v} \times (\nabla \times \mathbf{A}))$$

on the right-hand-side of 3.38b. This term is part of the non-linear operator in equation 3.39b. It is, if you like, a ghost of the non-linear operator D_t on what can be measured acoustically. When measured with ultrasound it is interpreted as part of the current. We note that an attempt to re-incorporate the ghost term back into some ‘acoustic

cally measured non-linear operator' would be ill-conceived for it would mean that the acoustic current is no longer conserved: the term most certainly is part of the current.

3.4.2 THE ACOUSTIC LAGRANGIAN

To finish, we introduce some future directions in acoustics that can be explored by means of the analogy. The first is the nature of spin, and the second is acoustic-turbulence interaction.

To do so, it is helpful to introduce the acoustic Lagrangian, which, due to the common description of acoustics and electromagnetism, is the same as the electromagnetic Lagrangian,

$$\mathcal{L} = \frac{1}{2} F \cdot F - A \cdot J. \quad (3.45)$$

In the absence of sources ($J = 0$), the canonical energy-momentum tensor, which expresses invariance with respect to translations, is found to be^[19;61], $T(a) = (a \cdot \nabla A) \cdot F - \frac{1}{2} a F \cdot F$. The explicit dependence on A can be moved to the bounding surface^[61] to leave a manifestly gauge invariant form within the volume,

$$T_{\text{gi}}(a) = -\frac{1}{2} FaF. \quad (3.46)$$

Similarly, the adjoint to the canonical angular momentum of the acoustic field, which expresses the isometry of the acoustic medium, is found from the Lagrangian to be^[61]

$$\mathbf{J}(n) = T(n) \wedge x - A \wedge (F \cdot n) = T(n) \wedge x - S(n). \quad (3.47)$$

The term $T(n) \wedge x$ is the orbital angular momentum and $S(n)$ is the spin of the acoustic field. The spin term is often suppressed by putting its influence in the boundary conditions, but since we are interested in acoustic plain waves we shall not do this.

The existence of the intrinsic acoustic spin raises interpretative issues. In the absence of satisfactory explanation for these the temptation to speculate will be resisted. All that

we say on the matter is to note that the helicity of the sound wave, the projection of the spin on the direction of the momentum, is identical to the hydrodynamic helicity introduced by Moffatt^[73]. This is interesting because the integral of the hydrodynamic helicity is a topological invariant that measures the degree of knottedness of the flow^[73].

To see this, we introduce the helicity,

$$\mathcal{H} \equiv \hat{\mathbf{P}} \cdot S(\gamma_0) = \hat{\mathbf{P}} \cdot (\phi \mathbf{E} - \mathbf{A} \times \mathbf{E}) = \frac{|\mathbf{E}|^2}{|\mathbf{E} \times \mathbf{B}|} \mathbf{A} \cdot \mathbf{B}. \quad (3.48)$$

where $\hat{\mathbf{P}}$ is the unit Poynting vector,

$$\hat{\mathbf{P}} = \frac{\mathbf{E} \times \mathbf{B}}{|\mathbf{E} \times \mathbf{B}|}. \quad (3.49)$$

and $S(\gamma_0)$ is the timelike component of the Spin as measured in the laboratory frame,

$$S(\gamma_0) = \frac{1}{2} \langle A \gamma_0 \gamma_0 (F \gamma_0 - \gamma_0 F) \rangle_2 \quad (3.50)$$

$$= \phi \mathbf{E} - \mathbf{A} \times \mathbf{E}. \quad (3.51)$$

For a sound wave $|\mathbf{E}| = c |\mathbf{B}|$ and so the helicity simplifies to

$$\mathcal{H} = \mathbf{A} \cdot \mathbf{B}. \quad (3.52)$$

The term $\mathbf{A} \cdot \mathbf{B}$ on the right hand side is the same as the relativistic generalisation² to the *hydrodynamic helicity* per unit volume defined by Moffatt^[73]. It is also readily interpretable. $\mathbf{B} = \nabla \times \mathbf{A}$ measures a rotation, and the rotation is projected about \mathbf{A} . The helicity therefore measures the degree to which the fluid streamlines rotate about themselves, that is, the degree to which the streamlines are helical^[73;90]. The contribution to $\mathbf{A} \cdot \mathbf{B} dV \approx \mathbf{A}_0 \cdot \mathbf{B}_0 dV$ is positive or negative depending on the orientation of the helix^[73].

² The relativistic generalisation is accomplished by replacing \mathbf{v} in Moffatt's definition with \mathbf{A} . Notice, furthermore, that Moffatt did not normalise the Helicity, that is $\mathcal{H}_{\text{Moffatt}} = p \cdot S$ rather than $\frac{1}{|p|} p \cdot S$, where p is the momentum. When we make the comparison to $\mathcal{H} = \epsilon_0 \mathbf{A} \cdot \mathbf{B}$, therefore, we implicitly divide $\mathcal{H}_{\text{Moffatt}}$ by a unit momentum, so that dimensionally all is correct.

In this way Moffatt identifies the component of the spin parallel to the momentum with the *orbital angular momentum* of a fluid streamline about its mean trajectory. The equivalence between the two helicities (acoustic and hydrodynamic) suggests that this interpretation of the spin is valid.

Finally we note that the hydrodynamic helicity was introduced by Moffatt because

$$I = \int |dV| \mathcal{H} = \int |dV| \mathbf{A} \cdot \mathbf{B} \quad (3.53)$$

is an invariant that defines the degree of knottiness of the fluid. In the case of two vortex rings, for example, $\mathcal{H} = 2\alpha\kappa_1\kappa_2$ where κ_i are the circulations around the two rings. If they are unlinked $\alpha = 0$, whereas if they are singularly linked $\alpha = \pm 1$. The helicity in a volume, the component of the spin parallel to the momentum, is therefore quantised in accordance with the topology of the streamlines.

The author does not have an interpretation for this fascinating result and so does not comment further. We note, however, that there has been considerable effort in applying the hydrodynamic helicity to electromagnetism, with implications to both the quantisation of the spin and to the quantisation of the charge. We refer the interested reader to the literature^[91;110;111].

3.4.3 INTERACTIONS BETWEEN SPINLESS CHARGES

When an acoustic charge has no spin (or the spin is ignored) the equations of motion can be derived from the manifestly gauge invariant energy momentum tensor in equation 3.46. By taking the divergence and picking out the spatial terms, the force \mathbf{f} is found to be^[19]

$$\mathbf{f} = -(\rho_q \mathbf{E} + \mathbf{J} \times \mathbf{B}). \quad (3.54)$$

If it is assumed that an acoustic charge q is carried by an ‘acoustic particle’ (a vortex tube without swirl, for instance) moving at speed \mathbf{u} , then $\mathbf{f} = -q(\mathbf{E} + \mathbf{u} \times \mathbf{B})$, which is the Lorentz force law. We argue, therefore, that turbulent sources of sound interact

according to the Lorentz-force law when measured acoustically.

Whether this result could be used to model bubble-bubble interactions remains an open question.

3.4.4 OTHER SIMILAR STUDIES

By using a relativistic version of Lighthill's formulation of aeroacoustics it was demonstrated that the acoustic analogue to the electric field is the Lamb vector (proportional to the Coriolis acceleration), and that the acoustic analogue to the magnetic field is the vorticity. An analogy in this form has been presented before by both Marmanis^[70] and Sridhar^[70;102]. However, both these attempts were constructed from Galilean fluid mechanics and so the analogy was only partial. A complete analogy, using a relativistic incompressible fluid, was first published by Garrido^[31] long before the studies of Marmanis and Sridhar. Unfortunately, this article was missed by the wider community, and has only come to the attention of the author since completing this thesis.

Relativistic fluids where the sound speed equals the speed of light have been studied many times before as theoretical curiosities^[80;81;108]. For example, Pekeris found that Hick's spherical vortex conserves angular momentum if and only if the sound speed equals the speed of light^[81]. The importance of such fluids, however, has not to the author's knowledge been recognised. Such fluids represent *what can be measured* when distances are obtained by echo-location.

An alternative analogy between acoustics and special relativity is found in the 'acoustic analogue gravity' literature (see Barceló, Liberati and Visser^[7] for a review). An *acoustic* metric is constructed that describes sound carried in bulk flow. While the description of space and time in this formulation is Euclidean, the acoustic metric turns out to be pseudo-Euclidean, and therefore obeys the Lorentz transformation. This results because sound carried away by a supersonic flow will never reach us and so the speed of sound is a limiting velocity in transformations. The analogue gravity literature then goes on to study the gravitational implications of the acoustic metric. The acoustic metric, albeit Lorentzian, is not the same as Minkowski's metric used here, but is a

function of the bulk flow. Analogue gravity does not consider the measurement process and operates within a world characterised by two metrics, the Lorentz invariant acoustic metric and the Galilean invariant spacetime metric. The correspondence of analogue gravity with relativity theory is therefore partial. The acoustic analogue to special relativity presented here is complete, the only difference is that the speed of sound takes the role of the speed of light.

THE PULSATIONS OF A BUBBLE AS MEASURED WITH ULTRASOUND

4.1 INTRODUCTION

Current models that describe the pulsations of a bubble in an acoustic field do not account for how measurements are made with ultrasound. In particular, how the finiteness of the sound speed influences the spatio-temporal locations attributed to echo sources, and limits the maximum velocities that can be measured. Measurements made acoustically with ultrasound differ from those made optically with a microscope due to the differing speeds of sound and light. When a model is proposed for the pulsations of a bubble the system of measurement that is to be used to test that model must also be specified. In this chapter the Keller-Miksis model - taken to be representative of current bubble pulsation models - is altered to predict for the first time the pulsations that are measured with ultrasound.

To do so it is recognised that measurements in ultrasound should be subject to the considerations of special relativity, where the speed of sound rather than the speed of light takes the role of the limiting velocity. This is because the pulse-echo definitions of time and space that are used in ultrasound are identical to the radar definitions used by Einstein. Furthermore, since all ultrasound measurements are temporal, a fixed and constant speed of sound is necessary before anything can be said regarding distance. Einstein's second postulate *must* be assumed for ultrasound to measure anything at all. The only assumption made is an insistence upon invariance to inertial motions

(Einstein's first postulate). It would be perverse for such a fundamental symmetry to be dependent on the choice of imaging modality.

Simulation results for the new model are presented and compared with the results from the original Keller-Miksis equation. The acoustically-measured-Keller-Miksis equation presented here correctly predicts that motions of the bubble wall that exceed the speed of sound cannot be observed with ultrasound. The radial response of the two models is similar when the harmonic response of the bubble is not strong - otherwise the pulsations are quite different when measured acoustically and optically.

4.2 THE ACOUSTICALLY-MEASURED KELLER-MIKSIS MODEL

4.2.1 THE ORIGINAL FORMULATION

The Keller-Miksis model^[52] assumes that a gas bubble is located within a stationary and vorticity free fluid medium. The fluid particles are described by the velocity potential, ψ . The bubble is assumed to remain spherical, with a time dependent radius, $a \equiv a(t)$, and assumed to remain at the origin. From the spherical symmetry of the model only radial components of the velocity need to be considered.

Keller and Miksis retain perturbations in density only up to first order, from which it follows that variations in the sound speed, c , are neglected and that the velocity potential obeys the linear wave equation,

$$\left(\partial_r^2 - \frac{1}{c^2} \frac{\partial^2}{\partial t^2} \right) \psi = 0. \quad (4.1)$$

The notation $\partial_r \equiv \frac{\partial}{\partial r}$ is used to denote the radial derivative while both $\partial_t \equiv \frac{\partial}{\partial t}$ and the over dot notation will be employed to denote the differential with respect to time.

The solution to 4.1 is

$$\psi = \frac{1}{r} \left(f_1 \left(t - \frac{r}{c} \right) + f_2 \left(t + \frac{r}{c} \right) \right), \quad (4.2)$$

where r is the radial distance from the centre of the bubble and f_1 and f_2 are functions

to be determined.

Since equation 4.1 is second order two boundary conditions are required. The first is that the radial velocity of the fluid, v , is equal to the velocity of the bubble wall. That is

$$v = \dot{a}(t) \text{ at } r = a. \quad (4.3a)$$

The second boundary condition is that the pressure in the liquid adjacent to the surface of bubble, $p(a, t)$, must equal the pressure on the bubble wall, p_b ,

$$p(a, t) = p_b. \quad (4.3b)$$

We will consider explicit expression for p_b section 4.2.5 and in section 4.2.6.

To apply these boundary conditions Keller and Miksis eliminated the spatial derivative of ψ by using its definition,

$$\partial_r \psi = v, \quad (4.4a)$$

and used Bernoulli's equation to eliminate the temporal derivatives,

$$\partial_t \psi = -\frac{1}{2}v^2 - h. \quad (4.4b)$$

h is the enthalpy of the fluid.

The completes the specification of the model that was setup and solved by Keller and Miksis^[52].

4.2.2 ALTERATIONS REQUIRED WHEN MAKING MEASUREMENTS WITH ULTRASOUND

Equations that describe measurements made with ultrasound require, via special relativity, Lorentz invariance. Equations 4.4a and 4.4b do not have this property and so do not apply to acoustical measurement. To fix 4.4a and 4.4b the relativistic generalisation

to the velocity potential^[60] must be used,

$$\nabla \psi = -\frac{w u}{n c} \equiv -A. \quad (4.5)$$

Here w is the heat function per proper volume and n is the particle number per proper volume. The velocity u and the vector potential, A , are spacetime vectors and ∇ is the spacetime derivative. This is the same as equation 3.23 used in chapter 3. The heat per proper volume can be written in terms of the total energy density, such that^[19;60]

$$w = \varepsilon + p = nmc^2 + nme + p, \quad (4.6)$$

where e is the thermodynamic energy and m is the proper mass. The second equality uses equation 3.20 from chapter 3. Spacetime vectors are sometimes referred to as 4-vectors, although this terminology will not be used here. The spacetime velocity, u , is parametrised so that $u^2 = c^2$ where c is the speed of sound. The symbol u has been used to avoid confusion with the radial component, v , of the spatial velocity (a 3-vector).

The temporal and spatial projections of 4.5 in the laboratory frame are

$$\partial_r \psi = \frac{\gamma w v}{n c} \equiv \frac{\phi v}{c} \quad (4.7a)$$

and

$$\partial_t \psi = -\frac{\gamma w c}{n} \equiv -\phi c \quad (4.7b)$$

where $\gamma = (1 - v^2/c^2)^{-1/2}$ is the Lorentz factor and the potential

$$\phi \equiv \frac{\gamma w}{n} \quad (4.8)$$

has been introduced for convenience. The heat function per particle is related to the

enthalpy by the proper mass,

$$w/n = (mc^2 + me + p/n) = m(c^2 + h). \quad (4.9)$$

The thermodynamic relation $h = e + p/(nm)$ has been used in the second equality.

The potential ϕ is the relativistic generalisation to the total enthalpy (multiplied by the proper mass). In the non-relativistic it becomes,

$$\phi \rightarrow \left(1 + \frac{1}{2} \frac{v^2}{c^2}\right) (mc^2 + mh) = mc^2 + \frac{1}{2} mv^2 + mh \quad \text{as } v/c \rightarrow 0. \quad (4.10)$$

The right hand side is the energy contributed by the rest mass plus the standard non-relativistic expression for the total enthalpy (multiplied by the mass), as claimed.

By replacing equations 4.4a and 4.4b with equations 4.7a and 4.7b the derivation of Keller and Miksis can be used without further alteration. The resulting equation will be Lorentz invariant and therefore satisfy the constraints imposed by using pulse-echo to define the spatio-temporal locations of the echo's source.

4.2.3 THE DERIVATION OF THE ACOUSTICALLY-MEASURED-KELLER-MIKSIS EQUATION

Differentiating equation 4.2 with respect to time obtains

$$r \partial_t \psi = f'_1 + f'_2, \quad (4.11)$$

where the prime denotes differentiation with respect to the argument, while differentiating with respect to the radius gives,

$$r^2 c \nabla \psi = r(f'_2 - f'_1) - c(f_1 + f_2). \quad (4.12)$$

Equations 4.11 and 4.12, evaluated at $r = a$, are combined to eliminate f'_1 ,

$$a^2 (\partial_t \psi + c \partial_r \psi) - 2af'_2 + c(f_1 + f_2) = 0. \quad (4.13)$$

By using equations 4.7a and 4.7b in 4.13 (rather than 4.4a and 4.4b) we obtain

$$a^2 (\phi \dot{a} - \phi c) - 2af'_2 + c(f_1 + f_2) = 0. \quad (4.14)$$

Differentiating 4.14 with respect to time and reusing 4.11 and 4.7b gives

$$a \frac{\phi}{c^2} \ddot{a} + 2\dot{a}^2 \frac{\phi}{c^2} - \phi \left(1 + \frac{\dot{a}}{c} \right) - a \frac{\dot{\phi}}{c} \left(1 - \frac{\dot{a}}{c} \right) - \frac{2}{c^2} f''_2 \left(1 + \frac{\dot{a}}{c} \right) = 0 \quad (4.15)$$

The driving acoustic pressure comes from the converging acoustic wave, f_2 . To evaluate this term, following Keller and Miksis, we assume that the incident wave is planar and decompose it into spherical harmonics. By assumption, however, the bubble pulsates purely radially and so only the zeroth harmonic interacts with the bubble. The potential of the incoming wave, $\psi_i(r, t)$, is accordingly $\psi_i(r, t) = \frac{1}{r} (f_2(t + r/c) + f_3(t - r/c))$. Requiring that the potential is finite at the bubble's centre implies that $f_2 = -f_3$ and so

$$\psi_i(r, t) = \frac{f_2(t + r/c) - f_2(t - r/c)}{r}. \quad (4.16)$$

The bubble is small in comparison to the wavelength and so the velocity potential of the fluid near the origin satisfies

$$\psi_i(a, t) = \frac{f_2(t + a/c) - f_2(t - a/c)}{a} \approx \frac{2}{c} f'_2(\tau). \quad (4.17)$$

The differential on the right-hand-side of 4.17 is a function of the proper time, τ , of the bubble. This is because the equation holds only in a frame of reference where the bubble is stationary and at the origin. Differentiating 4.17 with respect to the proper

time we obtain

$$\frac{d}{d\tau}\psi_i \equiv \gamma(\partial_t + v\partial_r)\psi_i = u \cdot \nabla\psi = \frac{2}{c}f''. \quad (4.18)$$

Using equation 4.5 this gives

$$\frac{2}{c}f'' = -\frac{wc}{n} = -\frac{\phi_i c}{\gamma}, \quad (4.19)$$

where ϕ_i is the incident potential. Substituting 4.19 into 4.15 and using equation 4.8 in the form $\phi = \gamma m(c^2 + h)$ we obtain

$$a\ddot{a}\gamma\left(1 + \frac{h}{c^2}\right)\left(1 - \frac{\dot{a}}{c}\gamma^2\left(1 - \frac{\dot{a}}{c}\right)\right) + 2\dot{a}^2\gamma\left(1 + \frac{h}{c^2}\right) - [\gamma(c^2 + h) - (c^2 + h_i)]\left(1 + \frac{\dot{a}}{c}\right) - \gamma\dot{h}\left(\frac{a}{c}\right)\left(1 - \frac{\dot{a}}{c}\right) = 0 \quad (4.20)$$

Equation 4.20 is the final answer. The enthalpy contains the pressure terms, and with them the boundary condition of equation 4.3b

The non-relativistic limit (with $\gamma \approx 1 - \frac{\dot{a}^2}{2c^2}$), equation 4.20 reduces to

$$a\ddot{a}\left(1 - \frac{\dot{a}}{c}\right) + \frac{3}{2}\dot{a}^2\left(1 - \frac{1}{3}\frac{\dot{a}}{c}\right) - (h - h_i)\left(1 + \frac{\dot{a}}{c}\right) - \dot{h}\left(\frac{a}{c}\right) = 0, \quad (4.21)$$

which is the original Keller-Miksis equation^[41].

The acoustically-measured-Keller-Miksis model therefore reduces to the original when the maximum speed of the bubble wall is small in comparison to the sound speed. In the non-relativistic approximation made to obtain equation 4.21 discards terms of order M^2 , where $M = |\frac{\dot{a}}{c}|$ is the Mach number of the bubble wall. Therefore, the original Keller-Miksis model approximates the acoustically measured motion when M^2 is small. I.e. up to about $M = 0.4$.

4.2.4 THE APPLICABILITY OF THE EQUATION

In the original derivation Keller and Miksis linearised the density. The consequence of this is that fluctuations in the sound speed are ignored. This enabled our starting point, the linear wave equation of 4.1, to be derived. The discarded second order terms become important when M^2 is not small. The approximation holds, therefore, up to about Mach 0.4. Interestingly, the optical and acoustical observer agree over the range of speeds to which the original Keller-Miksis equation is applicable.

When the measurements are made with ultrasound, however, no approximation is made to obtain equation 4.1. The reason is that ultrasound is not capable of measuring variations in the speed of sound. Second order fluctuations in the density can therefore play no role when ultrasound is used to describe the world.

When deriving the Keller-Miksis equation potential flow in the fluid was assumed. This implies that the vorticity tensor vanishes, for $F = \nabla \wedge A = -\nabla \wedge \nabla \psi = 0$. Therefore the acoustic sources vanish and the wave equation $\nabla^2 A = 0$ is satisfied. This was the starting equation in the derivation of the Keller-Miksis model, equation 4.1. Notice that other than potential flow, no approximation has been made to derive 4.1. The acoustically-measured-Keller-Miksis equation is exact.

4.2.5 THE PRESSURE ON THE SURFACE OF THE BUBBLE

When introducing the original Keller-Miksis model in section 4.2.1 the pressure on the surface of the bubble was not specified (equation 4.3b). In this section and the next we fix this boundary condition for the cases with and without viscosity.

The gas within the bubble may be modelled with a polytropic exponent, κ . The pressure within the bubble is then $p_e \left(\frac{a}{a_e} \right)^{-3\kappa}$ where p_e is the pressure of the gas within the bubble at equilibrium, and a_e is the radius of the bubble at equilibrium^[41]. The contribution of the vapour pressure has been neglected for simplicity. Within the bubble pressure exceeds the pressure of the fluid at the surface, $p(a, t)$, due to the contribu-

tions of the surface tension, σ . The pressure boundary condition is then

$$p_b(a) = p_e \left(\frac{a}{a_e} \right)^{-3\kappa} - 2 \frac{\sigma}{a}. \quad (4.22)$$

To write the boundary condition in terms of the enthalpy we use the thermodynamic relation $dh = \frac{1}{mn} dp$. Substituting in $n = \frac{n_\infty}{\sqrt{p_\infty}} \sqrt{p}$, equation 3.22, gives

$$h(a) = \int_{p_\infty}^p \frac{1}{mn} dp = 2 \frac{\sqrt{p_\infty}}{mn_\infty} (\sqrt{p} - \sqrt{p_\infty}) = 2 \frac{p_\infty}{mn_\infty} \left(\sqrt{p/p_\infty} - 1 \right) \quad (4.23)$$

In the non-relativistic limit $p_\infty = \varepsilon_\infty \approx n_\infty mc^2 \approx 1 \text{ GPa}$ ^[41]. This is much larger than any pressures reached in ultrasound and so we may write the pressure in terms of a fluctuations, p' , around the ambient pressure at the surface of the bubble, p_0 ,

$$p = p' - p_0 + p_\infty. \quad (4.24)$$

Then

$$h(a) = 2 \frac{p_\infty}{mn_\infty} \left(\sqrt{1 + \frac{p' - p_0}{p_\infty}} - 1 \right) \approx \frac{p' - p_0}{mn_\infty} \quad (4.25)$$

The acoustically-measured-Keller-Miksis equation is now complete. We emphasise that for an free polytropic gas bubble pulsating in ideal vortex-free fluid, the model is exact.

4.2.6 ACOUSTICALLY-MEASURED VISCOSITY

Viscous fluids have so far been excluded from our analysis. Viscosity usually plays a minor role in medical applications - an ideal fluid does a fairly good job for modelling propagation. However, the viscosity does play an important role in dampening the oscillations of the bubble. In ultrasound contrast physics, therefore, the viscosity is usually incorporated into the pressure boundary condition of equation 4.3b. To model the viscous dampening it is assumed that the fluid is Newtonian; only the *dynamic*

viscosity, η , is considered. Then the stress tensor measured with ultrasound is^[60],

$$\sigma(a) = ap - c\eta \left(a \cdot \nabla u + \nabla u \cdot a - a \cdot uu \cdot \nabla u - uu \cdot \nabla u \cdot a - \frac{2}{3} \nabla \cdot u (a - a \cdot uv) \right). \quad (4.26)$$

The derivative with respect to the vector a yields the trace^[39],

$$\text{Tr } \sigma(a) \equiv \partial_a \cdot \sigma(a) = 4p. \quad (4.27)$$

We wish to evaluate the radial component of the stress tensor, $\sigma_{rr} \equiv \hat{r} \cdot \sigma(\hat{r})$, where \hat{r} is the radial unit vector. This is because in our spherically symmetric model it is this component that dampens the oscillation. From 4.26 this is evaluated to be

$$\sigma_{rr} = -p + 2\eta \left[\partial_r v + \frac{\gamma^2 v}{c} \frac{cu \cdot \nabla}{\gamma} \left(\frac{\gamma v}{c} \right) - \frac{1}{3} c \nabla \cdot u \left(1 + \frac{\gamma^2 v^2}{c^2} \right) \right], \quad (4.28)$$

where v is the radial component of the velocity. To keep the expressions short the inner products $u \cdot \nabla = \frac{\gamma}{c} (\partial_t + v \partial_r)$ and $\nabla \cdot u = \frac{1}{c} (\partial_t \gamma + \partial_r (\gamma v))$ have not been expanded.

Equation 4.28 can be simplified by noting that $\left(1 + \frac{\gamma^2 v^2}{c^2} \right) = \left(1 - \gamma^2 \left(1 - \frac{v^2}{c^2} \right) + \gamma^2 \right) = \gamma^2$.

Using a similar trick we find,

$$\frac{\gamma^2 v}{c} \frac{cu \cdot \nabla}{\gamma} \left(\frac{\gamma v}{c} \right) = - \left(1 - \gamma^2 \right) \frac{cu \cdot \nabla}{\gamma} \gamma + \frac{\gamma^3 v}{c^2} \frac{cu \cdot \nabla}{\gamma} v = \gamma cu \cdot \nabla \gamma. \quad (4.29)$$

The relation $d\gamma = \frac{\gamma^3}{c^2} v dv$ has been used to obtain the second equality. Equation 4.28 then simplifies to

$$\sigma_{rr} = -p + 2\eta \left[\partial_r v + \gamma cu \cdot \nabla \gamma - \frac{1}{3} \gamma^2 c \nabla \cdot u \right]. \quad (4.30)$$

To make further progress we re-evaluate the trace using 4.30 and the other components

of the diagonal of the stress tensor,

$$\sigma_{tt} = p - 2\eta \left[\partial_t \gamma - \gamma c u \cdot \nabla \gamma - \frac{1}{3} (1 - \gamma^2) c \nabla \cdot u \right] \quad (4.31)$$

$$\sigma_{\theta\theta} = \sigma_{\phi\phi} = -p + 2\eta \left[\frac{\nu}{r} - \frac{1}{3} c \nabla \cdot u \right], \quad (4.32)$$

and find that

$$\text{Tr } \sigma(a) = 4p - 2\eta \left[2\frac{\nu}{r} + \partial_r \nu - \partial_r(\gamma \nu) \right]. \quad (4.33)$$

Equating 4.27 with 4.33 implies that

$$\partial_r \nu = -2\frac{\nu}{r} + \partial_r(\gamma \nu) \quad (4.34)$$

and so

$$\sigma_{rr} = -p - 4\eta \left[\frac{\nu}{r} - \frac{1}{2} (1 - \frac{1}{3} \gamma^2) \partial_r(\gamma \nu) - \frac{6\gamma^2}{5c^2} \nu \partial_t \nu \right]. \quad (4.35)$$

In the non-relativistic limit this equals

$$\sigma_{rr} = -p - 4\eta \left[\frac{\nu}{r} - \frac{1}{3} \partial_r \nu \right], \quad (4.36)$$

which is the standard expression for the radial stress exerted on a bubble^[41].

The spatial derivative $\partial_r(\gamma \nu)$ in 4.35 may be evaluated from the relation $\partial_r(\phi \nu) = -\partial_t \phi$, obtained from the spatial projection of 3.25 in the laboratory frame. However, the resulting equation is complicated to evaluate and contributes of order c^{-2} compared to the first term of 4.30, which of itself is small if the viscosity of the fluid is low. Therefore, for analytic simplicity, we neglect the small terms on the right of 4.35 and write

$$\sigma_{rr} \approx -p - 4\eta \frac{\nu}{r}. \quad (4.37)$$

Equation 4.37 is of adequate accuracy for our purposes and is used in the numerical studies that follow. It has the additional virtue in that it is identical for both acoustical and optical measurement.

The pressure boundary condition is then

$$p_b(a) = p_e \left(\frac{a}{a_e} \right)^{-3\kappa} - 2 \frac{\sigma}{a} - 4\eta \frac{\dot{a}}{r}. \quad (4.38)$$

4.3 ANALYSIS OF THE EQUATION

We finish by briefly examining the non-linear response of the two models to an incident sound pulse. The strongly non-linear response of bubbles is important in medical applications because it is a property not shared by the surrounding tissue, and therefore provides a means of identifying the bubble.

To start, we compare the response of the two models for 3 different pressures: 100 kPa, 300 kPa and 500 kPa. The equilibrium radius of the bubble is chosen to be 2 μm , which, like the pressures, is typical for diagnostic ultrasound applications. The pressure applied is a sinusoidal with a frequency of 500 kHz. The pulse consists of 10 cycles and the first and last quarter of the pulse is tempered with a cosine function. The radial and velocity response of the bubble is plotted in Figure 4.1.

For the low incident pressure of 100 kPa the radial response of the bubble is essentially identical in the two models (Figure 4.1a). This is as would be expected, for as Figure 4.1b shows, at this pressure the velocity of the bubble wall is always a small fraction of the sound speed.

At the higher pressure of 300 kPa the original Keller-Miksis model predicts that the bubble wall collapses at very high velocities, even surpassing the speed of sound on some occasions. It is obvious that ultrasound measurements cannot measure the speed of a bubble wall undergoing supersonic collapse, and so the predictions of the original Keller-Miksis equation is contrary to what is measured acoustically. Figure 4.1d illustrates what ultrasound would measure when a bubble responds to the pulse. The acous-

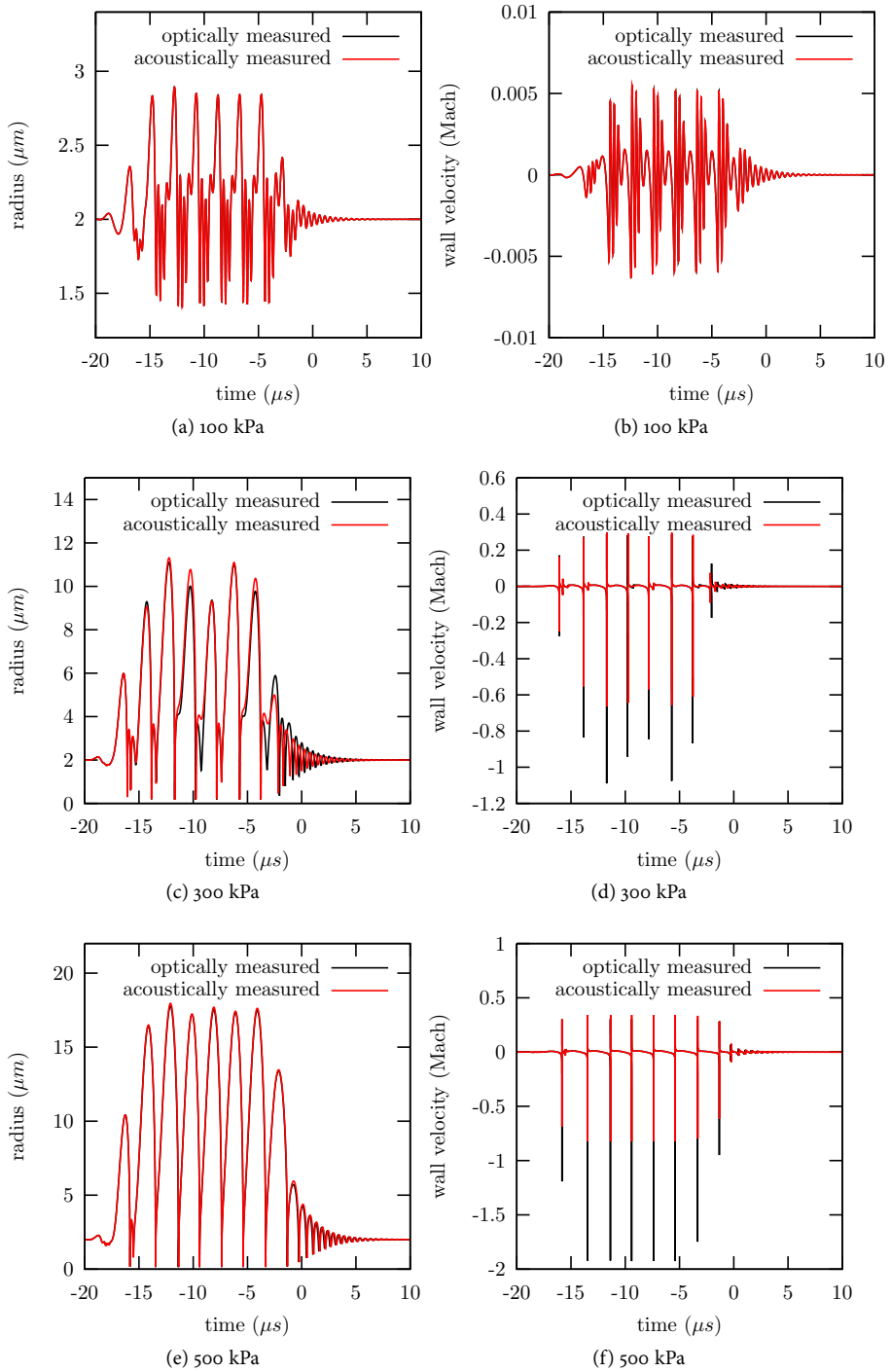


Figure 4.1: The calculated response of a two micron bubble to a 1/2 MHz wave at various pressures as measured optically (using the Keller-Miksis model) and acoustically (using the acoustically-measured-Keller-Miksis model). The radial response is shown in the figures on the left, the velocity response on the right.

tically measured velocity is always slower than the sound speed. The radial response as measured by ultrasound is predicted to be different to the response as measured optically, as is shown in Figure 4.1c.

At the yet higher pressure of 500 kPa there is a small surprise. As before the original Keller-Miksis model predicts that the bubble wall will collapse at speeds that cannot be measured acoustically, and as before the acoustically-observed-Keller-Miksis model assigns the spatial and temporal locations according to the pulse-echo definitions. The surprise, however, is in Figure 4.1e. In Figure 4.1e the predicted radial response of the bubble looks very similar with both models; the maximal radii are in good agreement, as are the times at which the bubble reaches its minimal radii. All this despite the large differences in the predicted velocity, Figure 4.1f.

A clue as to why the radial response at some pressures looks very similar for both models (Figure 4.1a and Figure 4.1e), while at other pressures it looks very different (Figure 4.1c) - apparently without any obvious correlation with the speed of the bubble wall - is found in the predicted scattering cross section of the two models.

4.3.1 THE SCATTERING CROSS SECTION

The scattering cross section, σ , is found from the ratio of the emitted acoustic power to the incident intensity,^[99]

$$\sigma(\omega) = 4\pi r^2 \oint \frac{(p(r,t)a(t))^2}{p_i(r,t)^2} dt, \quad (4.39)$$

where p is the emitted pressure, p_i is the incident pressure (a plain wave of frequency ω , and a is the bubble radius. In the acoustic far field the pressure emitted by the bubble^[43] is

$$p(r,t) = \frac{a^2 \ddot{a} + 2a\dot{a}^2}{r^2}, \quad (4.40)$$

and so the r^2 dependence of 4.39 and 4.40 cancels. The scattering cross section may be normalised by dividing out the area of the bubble at equilibrium, $4\pi a_e^2$.

The scattering cross section is only well defined for an incident planar wave. The period of the emitted wave can be different from period of the incident wave. The integral is carried out over the time period where both incident and emitted waves are stable - the closed integral sign being an mnemonic of this. This occurs when both the imaging and emitted wave oscillate an integer number of times within the period. However, this can make the scattering cross section hard to evaluate, for such a period may not exist (the ratio of the periodicity of the incident and emitted waves may be irrational), or else may be very long, and hence hard to find numerically.

Since the temporal and spatial dependence of the scattering cross section are integrated out, the scattering cross section is not expected to be dependant upon the measurement process. On the other hand, however, the scattering cross section is dependent upon the bubble wall's measured radius, velocity and acceleration in 4.40 - and therefore the two models will give different answers when M^2 is not small. We note, however, that the original Keller-Miksis model, unlike the acoustically measured version, never claimed to be accurate in presence of high velocities. The scattering cross section should therefore be computed using the acoustically measured theory.

To find the scattering cross section numerically a finite incident sinusoid must be used to drive the oscillation, and the incident number of cycles must be sufficient for the transient response to dampen. In this chapter, we use 750 cycles. To evaluate whether the response has stabilised a 12 cycle section of the radial response (i.e. from cycle 738 to 750) is chosen as a reference and the cross-correlation of the this 12-cycle segment is evaluated with previous 12-cycle segments. When the average of the cross-correlation coefficients is to within 0.1 % of the average of the autocorrelation coefficients, we consider that the bubble response is sufficiently stable and that the ratio of the periodicities of the incident and driving wave are sufficiently close to being integer. The scattering cross section is then evaluated over the segment. This procedure will fail if

1. the transient response has not been sufficiently damped.
2. the ratio of the periodicities of the incident and driving wave cannot be

expressed in 12 cycles (i.e. the super-harmonic ratio is not $1/6$, $1/3, 1/2$, $2/3$, 1 , 2 , $3/2$, 3 , 6).

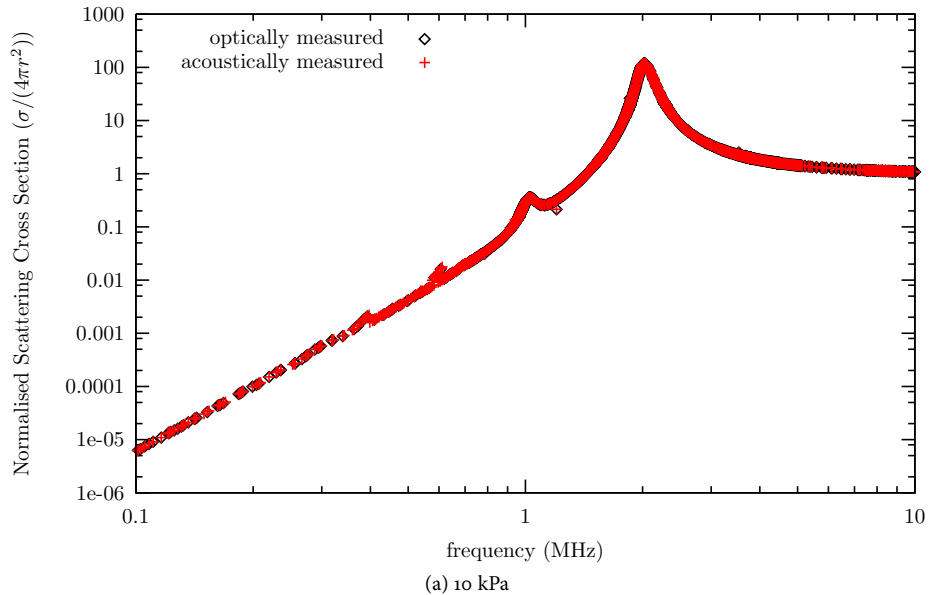
If the procedure fails then the search is abandoned and the scattering cross section is not given. While it is possible for more super-harmonics to be searched for, this process cannot go on forever, for irrational super-harmonics will never be found.

The normalised scattering cross section of a two micron bubble as a function of the incident frequency is plotted in Figure 4.3. Below the figures it is plotted where the scattering cross section could not be evaluated.

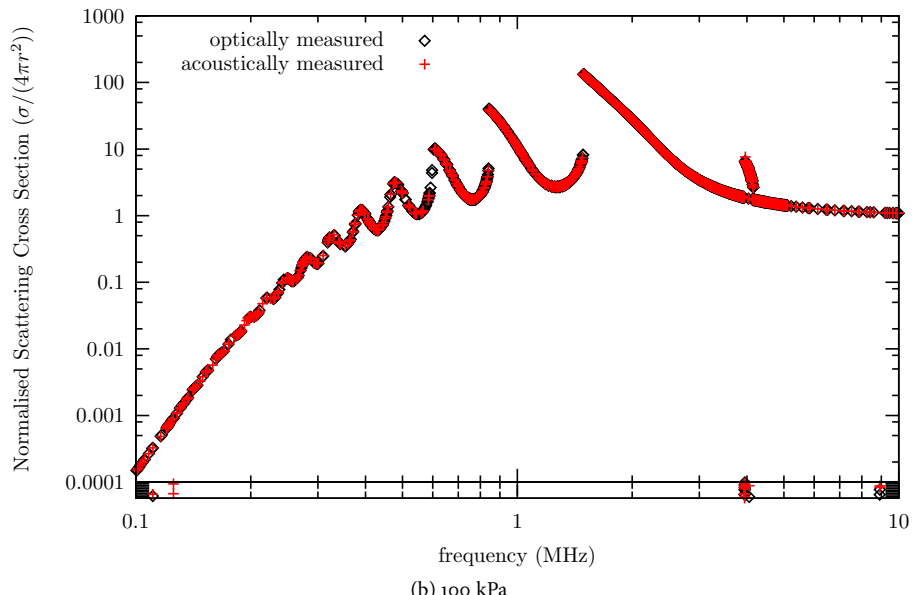
At 10 kPa the bubble's response is nearly linear when evaluated with both models, and Figure 4.2a exhibits a large resonance peak near to 2 MHz- which is familiar from linear studies on bubble response^[41]. At the higher pressure of 100 kPa, drawn in Figure 4.2b, the fundamental resonance occurs at lower frequency, the bubble also responds when pulsated at the first harmonic and at fractions of the fundamental. The response of the two models at 100 kPa is essentially identical, as was seen for the same pressure in Figure 4.1a and Figure 4.1b.

At the higher pressures shown in Figure 4.3 differences do emerge between the responses predicted by the two models. Considering Figure 4.3a first, we find that the fundamental again occurs at a lower frequency. Above this resonance the scattering cross section predicted by the two models is essentially identical. Near the resonance it becomes hard to evaluate the scattering cross-section, and there is a large drop-out in returned values. Such dropouts occur when unusual harmonics are present (or developing) within the bubble's response. Below the resonance the scattering cross section for both models becomes more stable (with few dropouts) but the scattering cross section evaluated using the acoustically-measured model is systematically lower than for when the scattering cross section is evaluated from the original model. These observations are repeated in Figure 4.3b, except that the discrepancy seems to begin at a harmonic of the fundamental.

Figure 4.3 may now be used to give an explanation the observations of Figure 4.1. The

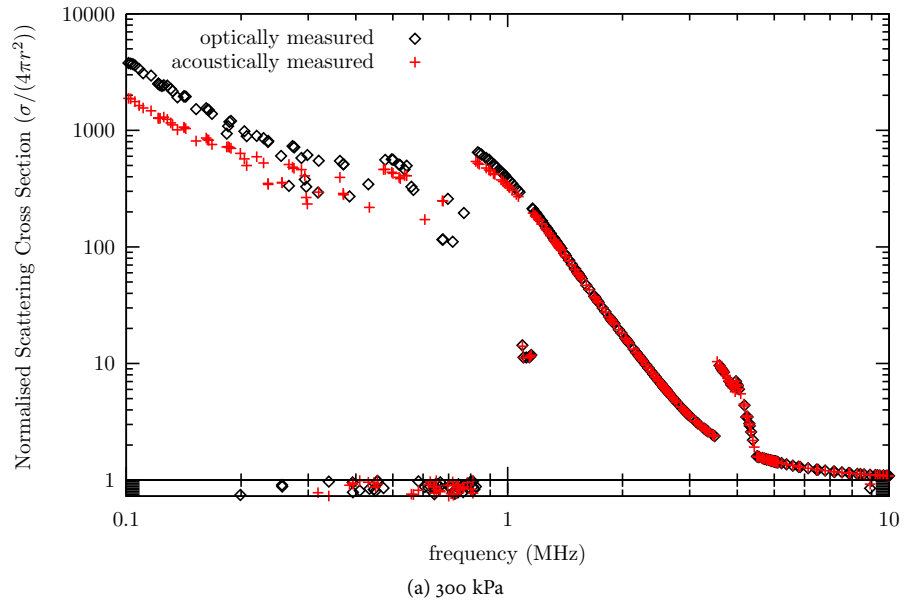


(a) 10 kPa

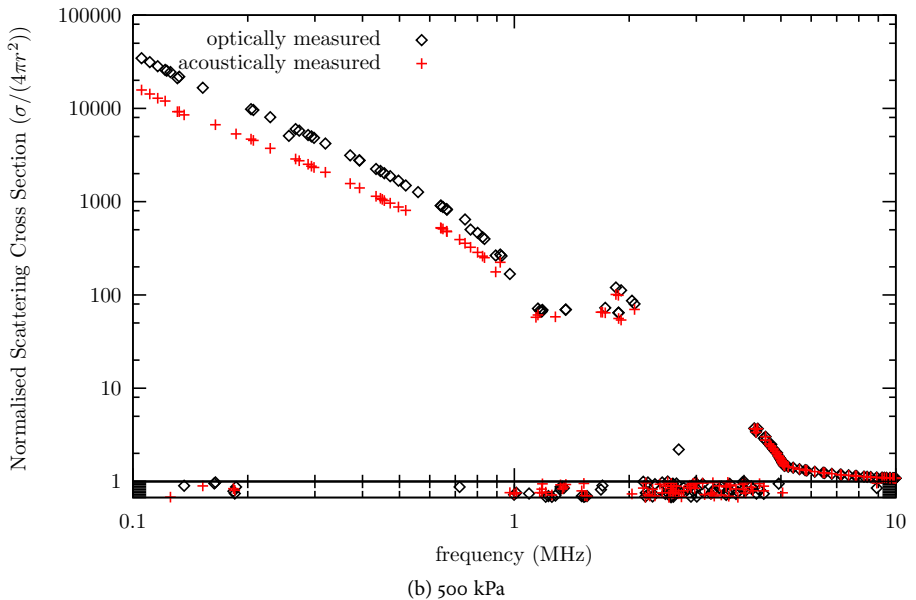


(b) 100 kPa

Figure 4.2: The calculated normalised scattering cross section as a function of frequency evaluated at various pressures as measured optically (using the Keller-Miksis model) and acoustically (using the acoustically-measured-Keller-Miksis model). The bubble has an equilibrium radius of $2 \mu\text{m}$. Below the graphs the frequencies at which the scattering cross section could not be evaluated is plotted. The small vertical axis of this plot is meaningless, it is used to help convey the density of points.



(a) 300 kPa



(b) 500 kPa

Figure 4.3: The calculated normalised scattering cross section as a function of frequency evaluated at various pressures as measured optically (using the Keller-Miksis model) and acoustically (using the acoustically-measured-Keller-Miksis model). The bubble has an equilibrium radius of 2 μm . Below the graphs the frequencies at which the scattering cross section could not be evaluated is plotted. The small vertical axis of this plot is meaningless, it is used to help convey the density of points.

divergence in the predicted scattering cross-section occur near resonance, where the role of harmonics (and therefore the dropout) is strong.

4.4 DISCUSSION

In this chapter we have derived for the first time the pulsations of a bubble as they would be measured with ultrasound. The model is based upon the Keller-Miksis model, but is exact. Indeed, the original Keller-Miksis equation can be obtained by approximating the acoustically-measured version - valid for when velocity of the bubble wall is small in comparison to the sound speed.

The derivation followed from noting that for ultrasound to measure distances (using pulse-echo) the sound speed in the medium must be known *a priori*, with no possibility of measuring variations in this sound speed. This has two consequences:

1. The sound speed must be measured to be a constant.
2. The sound must be measured to be propagating linearly.

If invariance to inertial translations is also assumed, then the constancy of the sound speed implies that ultrasound is subject to the considerations of special relativity, with the sound speed taking the role of the speed of light. This invariance has been assumed here.

Finally, the response of the acoustically-measured-Keller-Miksis equation to an acoustic wave has been simulated, and the results compared to the original Keller-Miksis equation. The radial pulsations observed by the two models is similar when the harmonic response of the bubble is not strong - otherwise the pulsations become quite different. The velocity response for the two models diverges when the bubble wall speed is high. The acoustically-measured-Keller-Miksis equation correctly maintains that ultrasound cannot measure supersonic bubble collapse, and predicts what is measured acoustically when such collapses do occur.

When the bubble wall moves at speeds close or exceeding the sound speed, differences are found between the scattering cross section obtained from the two models. The acoustically-measured-Keller-Miksis model claims accuracy in this regime. The original does not. The scattering cross section predictions therefore provide a means of testing the acoustically-measured-Keller-Miksis equation directly.

IMAGING A BUBBLE INFLUENCED BY A LOW FREQUENCY DRIVING WAVE

5.1 INTRODUCTION

Bubbles are generated at lower pressures at lower ultrasound frequencies^[116] but the resolution is poor for imaging. To overcome this problem two ultrasound waves are used in this thesis; the first, the *driving wave*, is used to generate the bubbles; the second, the *imaging wave*, is a short pulse at a much higher frequency that is used for imaging. The lifetime of the generated bubbles can be short and so the two waves are timed so that they are incident upon the bubbles simultaneously. This means that although the driving pulse arrives first, the imaging pulse arrives before the driving pulse has completed.

The limited frequency response of ultrasound transducers usually necessitates that the pulses are generated by two different transducers. We assume that this is the case here. The imaging wave therefore filters out most of the pressure generated by the bubble in response to the driving wave.

However, the driving wave does still influence the remaining high frequency scatter. It controls the phase-space¹ trajectory of the bubble prior to the arrival of the imaging pulse. The time delay between the arrival of the two waves determines which portion of the phase-space trajectory is *sampling* by the imaging pulse. The driving wave and the time delay can therefore be used together to manipulate the radius and velocity of

¹The phase-space of a bubble is comprised of the bubble radius, a , and the bubble wall velocity, \dot{a} . The phase-portrait is the two dimensional trajectory of a and \dot{a} in phase-space.

the bubble when imaged. One immediate application of this is to temporarily shrink a conventional microbubble so that it may resonate at a higher frequency.

This chapter studies the influence of the driving wave on the high frequency response of a bubble. Our final application is the imaging of small (sub-micron) bubbles that can be created with the driving wave. However, since the two wave technique is an important one, we broaden our discussion to include micron sized bubbles and a driving wave of more conventional (lower) pressures.

The aims of the study are two fold. The first is to understand how the high frequency response of the bubble depends upon the portion of the phase-space trajectory sampled by the imaging wave. For this we study the following five parameters that influence the trajectory:

- the frequency of the driving and imaging waves, f_d and f_i , respectively,
- the amplitude of the two waves, A_d and A_i ,
- the radius of the bubble, a .

in addition to the temporal offset between the arrival of the two waves. The second aim is to explore this parameter space to find the ‘optimum’ parameters for imaging a nucleated bubble.

This chapter begins by detailing in section 5.1.1 the simple linear model used for the incident pulses in this chapter.

Second, in section 5.1.2, we distinguish the notions of phase that are used in this chapter: the phase of the driving pulse, ϕ_d , and the phase of the bubble’s phase-space trajectory, ϕ_b . The latter is more physically relevant, the former we have better control over. The phase (driving or bubble) at which the incident wave arrives is denoted with a subscript o, that is ϕ_{d0} and ϕ_{b0} , respectively.

Third, in section 5.1.3, we describe how we characterise the high frequency scatter that returns in two wave imaging. To avoid imaging the higher harmonics induced by the driving wave a two pulse technique is introduced. First the bubble is imaged with both

the driving and the imaging wave and from this the response to just the driving wave is subtracted. The result we call the *excess pressure*. The *excess scattering cross section*, calculated from the excess pressure, is taken to be a measure of the effectiveness of the two wave technique.

With these preliminaries completed we consider in section 5.2 how the excess scatter varies with the sampled driving phase, ϕ_{d0} . We confirm the behaviour that would be expected: that a bubble that is smaller than its resonant radius (given the imaging frequency and amplitude) has a stronger scatter when it is grown by the driving wave and that a bubble that is larger than its resonant radius scatters more strongly when it is shrunk; and that the phase relationship with ϕ_d breaks down when the bubble starts to resonate under the influence of the driving wave,

Finally in section 5.3.1 we explore the full parameter space to find the ‘optimum’ values of the driving and imaging pressure, frequency, and the phase ϕ_{d0} for imaging a 100 nm-radius bubble. In choosing this radius we are restricting our attention to the nucleation application. To explore the parameter space a Markov-chain random walk is employed.

In this chapter all bubbles are modelled with the acoustically-measured-Keller-Miksis equation. The gas within the bubbles is assumed to be air and obey adiabatic thermodynamics. The surrounding medium is modelled as water and the dynamic viscosity for the water-gas interface is taken to be 1×10^{-3} Pas. Since we are interested in nucleated bubbles no encapsulating shell is modelled, and the bubble has an air-water surface tension of 0.07280 Nm^{-1} . The ambient pressure p_0 is taken to be 0.1013 MPa. The parameters, unless otherwise stated, will take their values from Table 5.1

We restrict the imaging wave to short pulses of 3 cycles. This is considered to be the shortest - and therefore with the greatest resolution - that is realisable; transducer ringing making shorter waves difficult to attain.

We want the driving wave to be able to set up a near stable phase-space trajectory for the bubble. This requires, in our experience, at least 5 or 6 cycles. Long pulses are no

Table 5.1: Parameter values unless otherwise stated

Default		
driving frequency	f_d	0.5 MHz
imaging frequency	f_i	20 MHz
driving amplitude	A_d	0.1 MPa
imaging amplitude	A_i	0.5 MPa
driving cycles		20 μ s ^a
imaging cycles		3

^aThe number of driving cycles depends on the frequency. It is chosen to be the first integer number complete after a duration of 20 μ s.

good because with many cycles the wave will substantially change the bubble through processes such as rectified diffusion (which are not modelled). We therefore limit the duration of the imaging pulse to be the shortest pulse greater than 20 μ s with an integer number of cycles.

5.1.1 THE INCIDENT PULSES

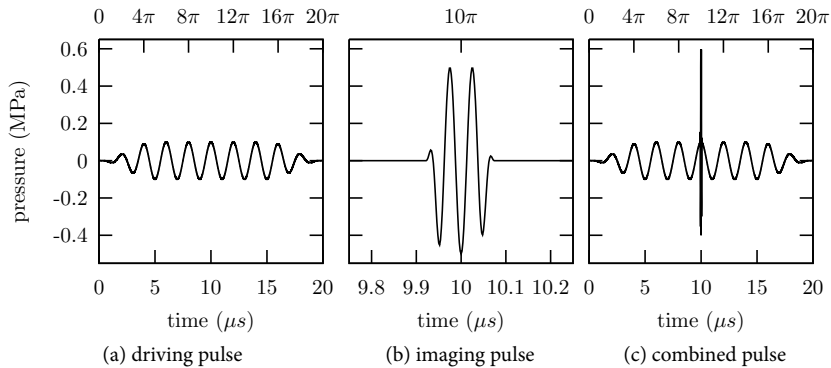


Figure 5.1: Examples of the incident pulses used in this thesis. The lower axis is the time at which a bubble experiences the incident wave. The upper x-axis is the phase of the driving wave. In (b) it is seen that the peak negative pressure of the incident wave occurs at the phase of 10π . The driving frequency used is 2 MHz.

The model used for the driving and imaging pulses in this thesis is kept simple. The

waves are assumed to be linear sinusoids that are tempered into finite durations with a half-wavelength cosine. The first and last quarter are tempered, with the middle 50% being pure sinusoid. A few examples are shown in Figure 5.1.

It would be possible to include greater complexity into the incident sound waves. For example, including non-linear propagation of the pulse from the transducer to the bubble - in accord with the conserved current - would perhaps improve the correspondence with experiment. However, including such complexities only serves to hide the current investigation of two wave imaging within a huge parameter space. We feel that a cosine-modulated sinusoid is the simplest yet still plausible model for an ultrasound pulse.

5.1.2 THE WORD PHASE IN THIS THESIS

In this thesis we refer to two different phase angles: the phase of the driving wave, ϕ_d , and the phase of the bubble's pulsation, ϕ_b .

The driving pressure is a modulated sinusoid and ϕ_d is simply the phase of the underlying sinusoid with respect to a cosine-wave. It is shown on the upper axis to the plots in Figure 5.1.

The phase of the bubble parametrises the bubble's trajectory through phase-space so that every clockwise cycle encircling the equilibrium position contributes 2π . We define ϕ_b to be the angle of the bubble's location in phase-space with respect to the equilibrium position, $(a_e, 0)$,

$$\tan \phi_b = \frac{\dot{a}(t)}{a(t) - a_e}. \quad (5.1)$$

Three phase-portraits are shown in Figure 5.2 to illustrate 5.1.

In Figure 5.2a the bubble's response is dominated by the fundamental. The phase changes by 2π for every period of the driving wave. On the other hand, at a higher pressure of 125 kPa the response is dominated by a harmonic. The phase changes by 4π for every period of the driving wave. As was noted in chapter 4, the resonance frequency decreases as the incident pressure increases, and so at the still higher pressure of

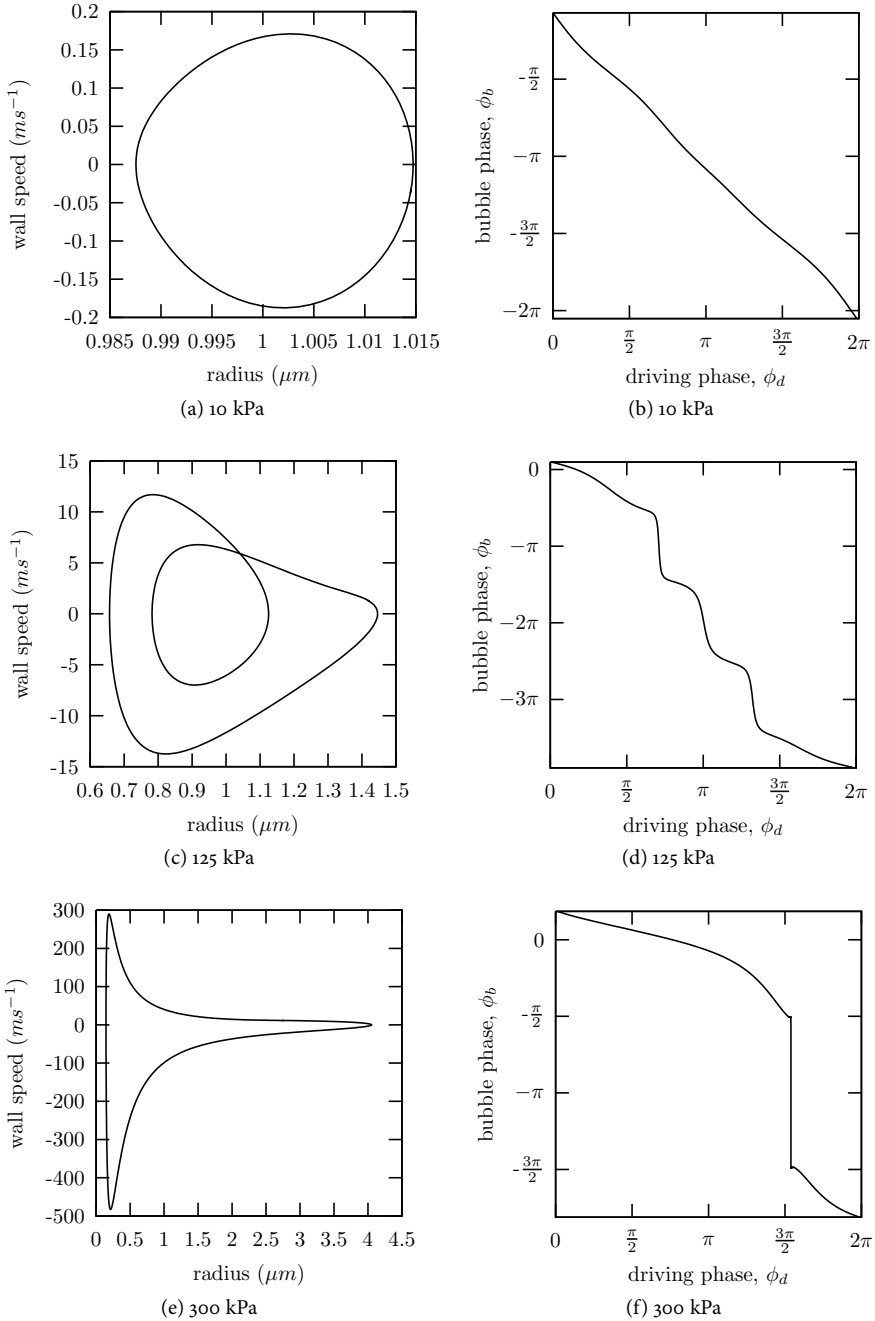


Figure 5.2: The phase-portraits and ϕ_b as a function of ϕ_b for driving waves of three amplitudes. In (a) and (b) a 10 kPa 2 MHz driving wave was applied to a 2 μm -diameter bubble. In (c) and (d) the driving pressure was 125 kPa. In (e) and (f) the driving pressure was 300 kPa.

300 kPa, the response is again dominated by fundamental. The phase relation between ϕ_d and ϕ_b at this high pressure is once again fairly simple, albeit not linear (Figure 5.2f).

5.1.2.1 The incident phases

The scattered pressure from a bubble is a function of its phase-space trajectory, which is parametrised by ϕ_b . The driving wave, irrational super-harmonics excepted, will (eventually) put the bubble into a stable orbit, such as those illustrated in Figure 5.2. The response of the bubble to the imaging wave will depend upon its existing orbit imposed by the driving wave. The response of the bubble to the imaging wave can therefore be characterised as a function of ϕ_{b0} , the phase of the *bubble* when the imaging pulse is first incident upon the bubble.

Unfortunately, the bubble's phase is not a parameter that we have direct control over. All we can control is the time lag between the driving and incident waves upon the bubble. This gives the phase, ϕ_{d0} , of the *driving wave* when the imaging pulse is first incident upon the bubble.

When the duration of the imaging pulse is short in comparison to the driving period, such as in Figure 5.1c, the imaging wave covers a short range of driving frequencies. The imaging wave can therefore be said to *sample* the driving phase at ϕ_{d0} . Since the bubble's phase can change a great deal over very short time periods (Figure 5.2f), it is not generally true that the imaging wave samples a particular value of ϕ_b . However, it is mostly true, particularly when the harmonic response is not too strong. The proposition that the imaging wave samples a particular ϕ_b becomes truer the greater the ratio between imaging and driving frequencies.

5.1.2.2 The relationship between ϕ_d and ϕ_b

When the bubble responds linearly to the driving pressure the relationship between the phase of the driving wave and the phase of the bubble can be determined analytically. By linearising the acoustically-measured-Keller-Miksis equation (equation 4.20

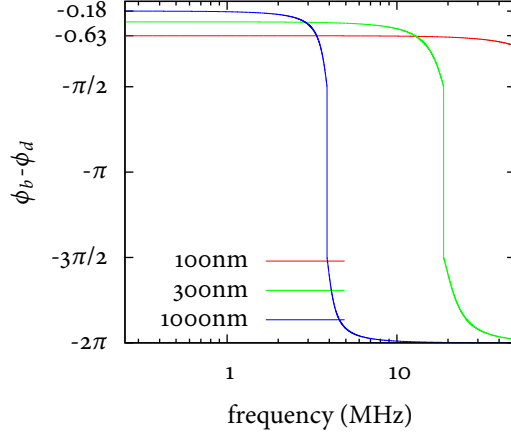


Figure 5.3: The difference between ϕ_b and ϕ_d with respect to frequency for bubbles of different radii.

on page 81) so that $a(t) \rightarrow a_e + \varepsilon$ we obtain

$$m\ddot{\varepsilon}(t) + \lambda\dot{\varepsilon}(t) + \omega_r^2\varepsilon(t) = A(t), \quad (5.2)$$

where

$$m = a_e \left(1 + \frac{4\mu}{a_e n m c} \right) \quad (5.3)$$

$$\lambda = \frac{3\kappa}{n m c} \left(p_0 + \frac{2\sigma}{a} \right) + \frac{4\mu}{a_e m n} - \frac{2\sigma}{a_e n m c} \quad (5.4)$$

$$\omega_r^2 = \frac{1}{a_e n m} \left(3\kappa \left(p_0 + \frac{2\sigma}{a_e} \right) - \frac{2\sigma}{a_e} \right) \quad (5.5)$$

and

$$A = -\frac{1}{n m} p_i, \quad (5.6)$$

where n is the equilibrium number density, m is the mass per particle, μ is the dynamic viscosity, σ is the surface tension and $\kappa = 1.4$ is the adiabatic polytropic index. We suppose in this subsection that the incident pulse is a pure sinusoid, with $p_i \propto \cos(\omega(t))$.

Equation 5.2 is the equation for a damped simple harmonic oscillator with solution

$$\varepsilon \propto \cos(\omega t + \beta). \quad (5.7)$$

The angle β is the desired phase difference between ϕ_b and ϕ_d and is equal to

$$\beta = \tan^{-1} \left(\frac{\lambda\omega}{m\omega^2 - \omega_r^2} \right). \quad (5.8)$$

As examples, Figure 5.3 plots β as a function of phase for a 100 nm, 300 nm and 1 μm -radius bubble. The phase difference drops rapidly at resonance.

5.1.3 CHARACTERISING THE SCATTER IN TWO WAVE IMAGING

The scattering cross section, the quotient of the scattered power to the incident intensity, was used in chapter 4 as a measure for the effectiveness of a contrast agent. The definition is repeated here for convenience,

$$\sigma(\omega) = 4\pi r^2 \oint dt \frac{p^2 a^2}{p_i^2}, \quad (4.39)$$

where, p is the emitted pressure, p_i the incident pressure, and a is the bubble radius. The integral is carried out over the time period where both incident and emitted waves are stable - the closed integral sign being an mnemonic of this. The incident pressure wave is an infinite plane wave and is therefore not applicable to the short pulses that are used in diagnostic ultrasound.

Equation 4.39 may be generalised to pulses by simply integrating over the whole pulse. This is represented by an open integration sign,

$$\sigma_{wp} = 4\pi r^2 \int p^2 a^2 dt \quad (5.9)$$

In general the bubble continues to ring after the driving pressure has stopped. The two integrals in 5.9 are therefore not over equal time periods.

When two different transducers are used to generate the two waves, however, equation 5.9 is no longer appropriate, for it does not incorporate the limited frequency response of the imaging transducer. The emitted pressure in 4.39 section should be Fourier filtered. In this thesis we model the response of the transducer with a Gaussian-shaped filter with a standard deviation on 25% of the central frequency, μ . That is the Fourier filter, \mathcal{F} , on the emitted pressure, $p = p(r, t)$, is,

$$\mathcal{F}[p] = \text{FFT}^{-1} \left[e^{\frac{-8(\omega-\mu)^2}{\mu^2}} \text{FFT}[p] \right] \quad (5.10)$$

where FFT is the Fourier transform and FFT^{-1} is its inverse.

The effect of the filter on a highly non-linear response is shown in Figure 5.4. The filtered pressure in Figure 5.4d does not retain only the response to the imaging wave, but also the high frequency component of the bubble collapse and rebound.

The ‘breakthrough’ of the response of the bubble to the driving wave causes a difficulty in interpretation. The imaging transducer measures the location of the bubble from the time at which the imaging pulse returns. The first possibility is that the breakthrough signal that arrives before and after the imaging pulse will be attributed to different spatial locations. The imaging transducer will then measure *phantom bubbles* in the image. Alternatively, if we know a priori through experimental setup that we are imaging just one bubble, then the signal that arrives prior to the bubble breaks temporal ordering; the bubble scatters before the imaging pulse arrives.

To overcome this difficulty more information is required by the imaging transducer. This can be achieved by subtracting the response of the bubble when there is no imaging wave. This gives the excess pressure generated in response to the imaging wave,

$$\Delta p = \mathcal{F}[p^{(d,i)}] - \mathcal{F}[p^{(d)}], \quad (5.11)$$

where $p^{(d,i)}$ is the pressure emitted when both driving and imaging pulses are incident, and $p^{(d)}$ is the pressure emitted in response to just the driving pulse. The effect of equation 5.11 is shown in Figure 5.5. Most notably we see that the ringing is elimi-

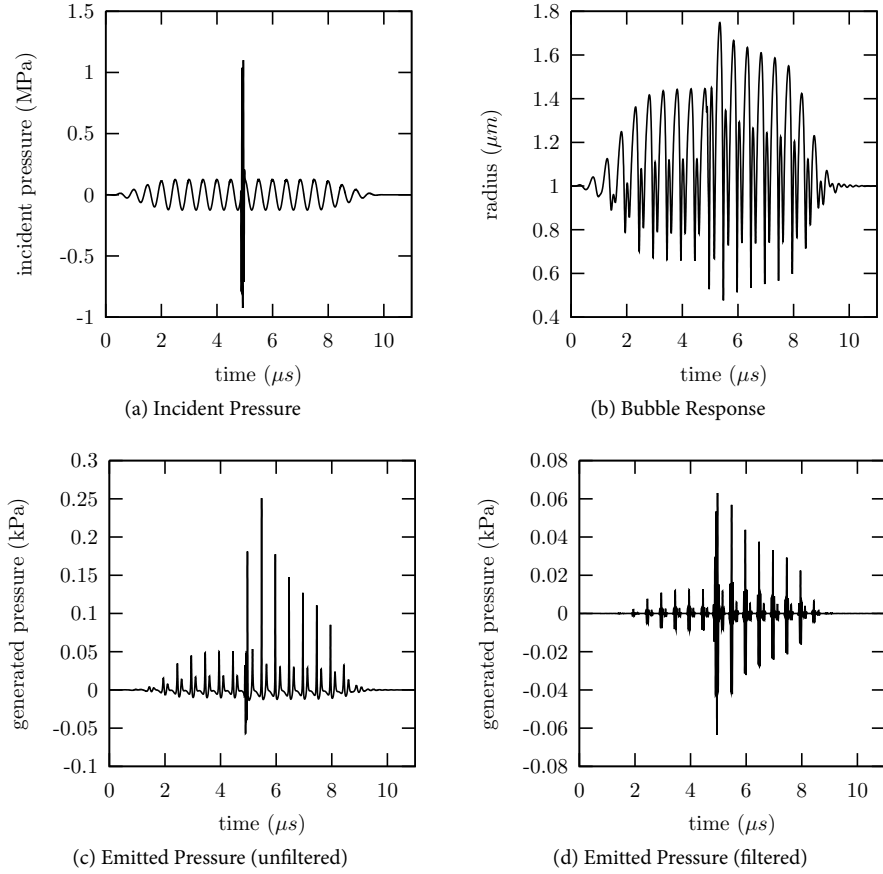


Figure 5.4: In (a) the incident pressure to a $2 \mu\text{m}$ bubble is plotted. It consists of a 20 cycle, 2 MHz driving pulse, driven at 0.125 MPa and a 3 cycle, 20 MHz imaging pulse driven at 1 MPa . The response of the bubble is plotted in (b). The calculated far-field emitted pressure is plotted in (c) and the filtered emitted pressure is plotted in (d). The pressures are evaluated 20 mm from the bubble

nated prior to the arrival of the imaging wave. This is a great improvement because it restores temporal ordering to the high-frequency images. The remaining ringing after the arrival of the imaging wave occurs because the imaging wave perturbs the phase-space trajectory of the bubble into a different orbit. While it still may be misinterpreted as phantom bubbles, it is at least a genuine response to the imaging wave.

It is helpful to summarise the excess pressure plot into a single number. For this purpose

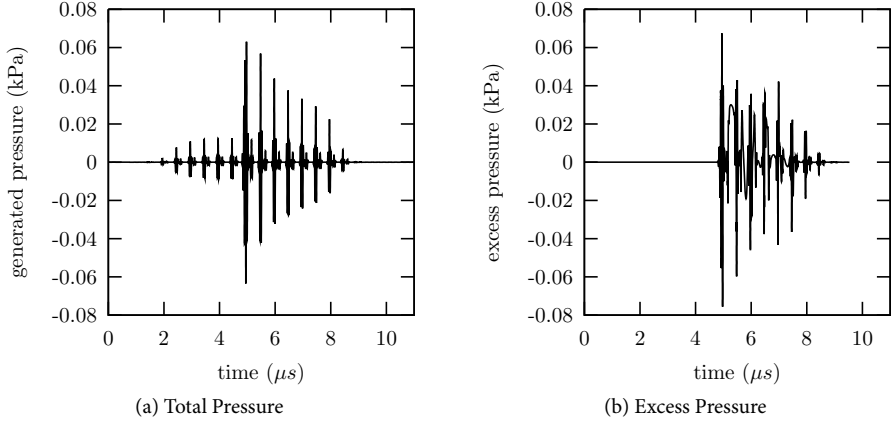


Figure 5.5: A comparison between the total pressure received by the imaging transducer and the excess pressure received. Figure (a) is repeated from Figure 5.4d for convenience

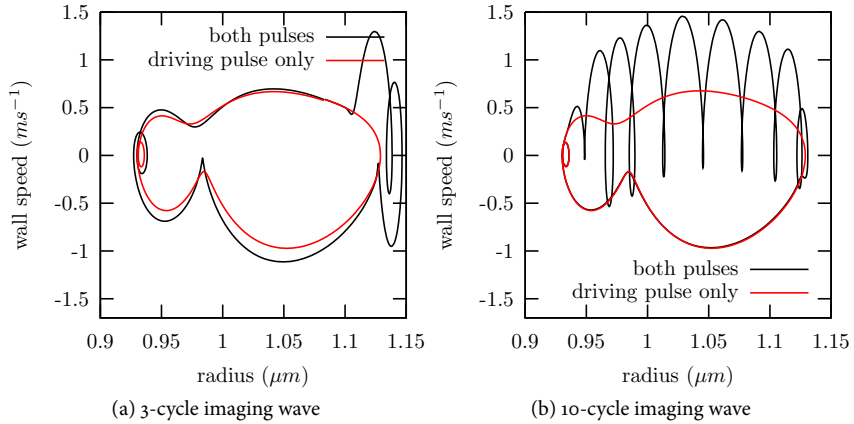


Figure 5.6: The phase-space trajectory of 2 μm -diameter bubble to short and long imaging pulses. The driving pressure is 75 kPa and the imaging wave pressure is 100 kPa.

the excess scattering cross section is defined to be

$$\sigma_{\text{ex}} = 4\pi \frac{\int dt ([\Delta p])^2 a^2}{\int dt p_i^2}. \quad (5.12)$$

σ_{ex} is the measure that we wish to optimise.

5.1.3.1 Reducing the phase-space perturbation in the bubble's response

A perturbation to the bubble's phase-space trajectory manifests itself as a ringing signal when it is filtered by the imaging transducer. This ringing obfuscates the location of the bubble and so it is worthwhile understanding how the perturbation can be reduced.

The perturbation induced by the imaging wave will be small when the imaging pulse expands and contracts the bubble equally. This will be true if the imaging pulse contains many cycles and the response of the bubble to it is linear.

If the pulse is short, however, the tempered tails of the pulse do not average out (Figure 5.1b) and the bubble's expansion will not equal its compression. This is seen in Figure 5.6. In each plot the response of a 2 μm diameter bubble is drawn: first in response to the driving wave alone (in red); and second the response to both the driving and imaging waves (in black). For a 3-cycle imaging wave (Figure 5.6a) it is seen that the two trajectories are quite different, even at this low incident pressure. However, as expected, the longer 10-cycle pulse returns to the unperturbed trajectory (Figure 5.6b).

Similarly, a difference between the expansion and contraction stages of the bubbles oscillation is characteristic of a nonlinear response. As can be seen in Figure 5.4b, for example, the expansion phase is greater both in duration and amplitude. We expect, therefore, that the perturbation in the bubble's phase space trajectory to be greater when a nonlinear response is in its expansion phase - for it is here that the nonlinearity has the time and amplitude to express itself. This phase dependence will be confirmed in section 5.2.2.

In summary, the ringing of the bubble in the excess pressure image can be reduced quite effectively by reducing the time averaged pressure of the imaging wave to zero. This is most easily achieved by increasing the number of cycles of the imaging wave, although this is undesirable as it compromises resolution. Careful synthesis of the imaging pulse to balance compression and rarefaction of the imaging pulse is not in the scope of this thesis, and so we keep the uneven 3-cycle wave. Indeed, experiments in this thesis use a commercial scanner for imaging, and the imaging pulse is not under experimental

control.

5.2 HOW THE PARAMETERS INFLUENCE EACH OTHER

In the introduction we chose six parameters to investigate: the frequencies and amplitudes of the incident driving and imaging waves, f_d , f_i , A_d and A_i ; the time lag between the two waves, ϕ_{d0} ; and the radius of the bubble, a .

The time lag between the imaging and driving waves is the most interesting, as it controls the part of the bubble's phase trajectory that get sampled by the imaging wave. This section investigates how the other parameters change the scattering as a function of ϕ_{d0} .

5.2.1 THE SCATTER AS A FUNCTION OF DRIVING PHASE

We begin by considering the dependence of the excess pressure, a function of the driving phase, ϕ_d , on the dependence of the sampled driving phase, ϕ_{d0} . A grayscale plot of $\sigma_{ex}(\phi_d, \phi_{d0})$ is hard to visually interpret, however, due zero being mid-gray. For this reason, and also due to the familiarity of B-mode images in ultrasound, we plot the Hilbert transform of the excess pressure. This is done in Figure 5.7 for a 2 μm -diameter bubble pulsated with a 150 kPa, 0.5 MHz driving wave, and a 500 kPa, 20 MHz imaging wave. In Figure 5.7 we also plot the excess scattering cross section from equation 5.12 (on the left), and the driving pulse used (on the top).

Figure 5.7 shows that the excess scattering cross section oscillates with the same periodicity as the driving pressure and that the scatter is high when driving pressure is high. If the bubble were responding linearly then the phase with respect to the driving wave would be expected to be -0.18 (Figure 5.3). A high pressure would therefore correspond to a contracted bubble.

In this case, however, the response of the bubble to the driving pulse is far from linear. Figure 5.8d shows the phase-space trajectory of the bubble for the range $8\pi \leq \phi_d < 10\pi$. The mapping between the bubble's phase and the driving phase is plotted in (a). We

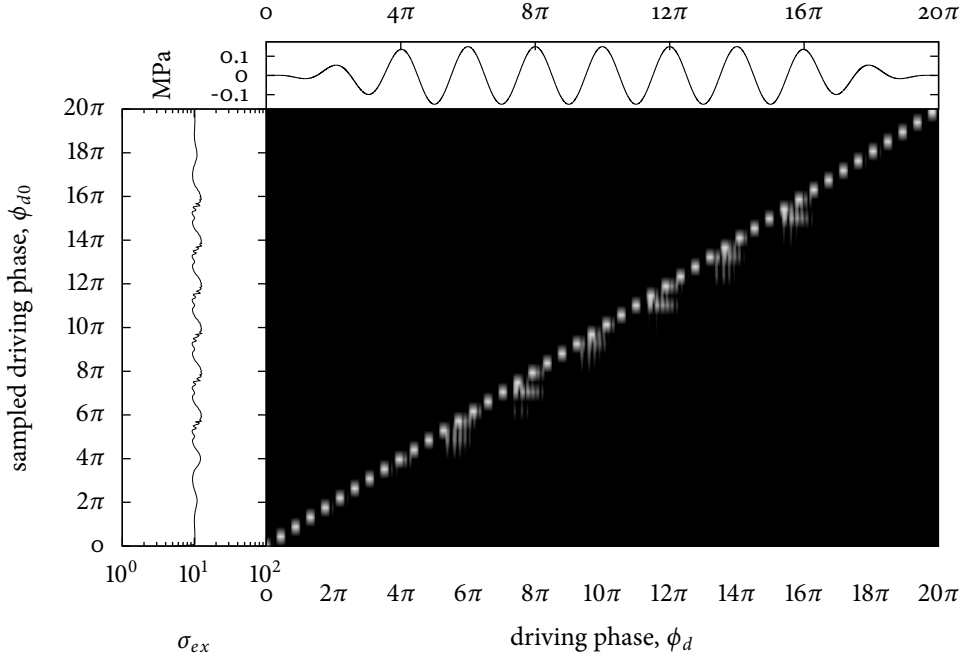


Figure 5.7: The excess pressure and the excess scattering cross section as a function of ϕ_{d0} and ϕ_d for a 2 μm -diameter bubble pulsated with a driving wave of 150 kPa. Also shown is the excess scattering cross section, σ_{ex} , and the driving pulse used.

find that for the 2π change in the driving wave the bubble's phase actually changes by 6π ; the harmonics are already dominating. Nevertheless, it still remains true that the excess scattering cross section is greatest when the bubble is small. This is seen by mapping $\sigma_{\text{ex}}(\phi_d) \rightarrow \sigma_{\text{ex}}(\phi_b)$, which is carried out in by going from Figure (c) to (b) via (a). The scattering is maximal at the bubble phases $-17\pi - 6m\pi$, for integer m , which corresponds to the bubble being small. The arrow in Figure 5.8d indicates the phase-space position when $\phi_b = -17\pi$.

The increase in the scattering when the bubble is shrunk has a simple interpretation. From Figure 5.3 we see that a 300 nm bubble is resonant at about 20 MHz. A 2 μm -diameter bubble is larger than this. However, by shrinking it you are transiently creating a bubble that is closer to its resonance - and therefore increasing its scattering cross

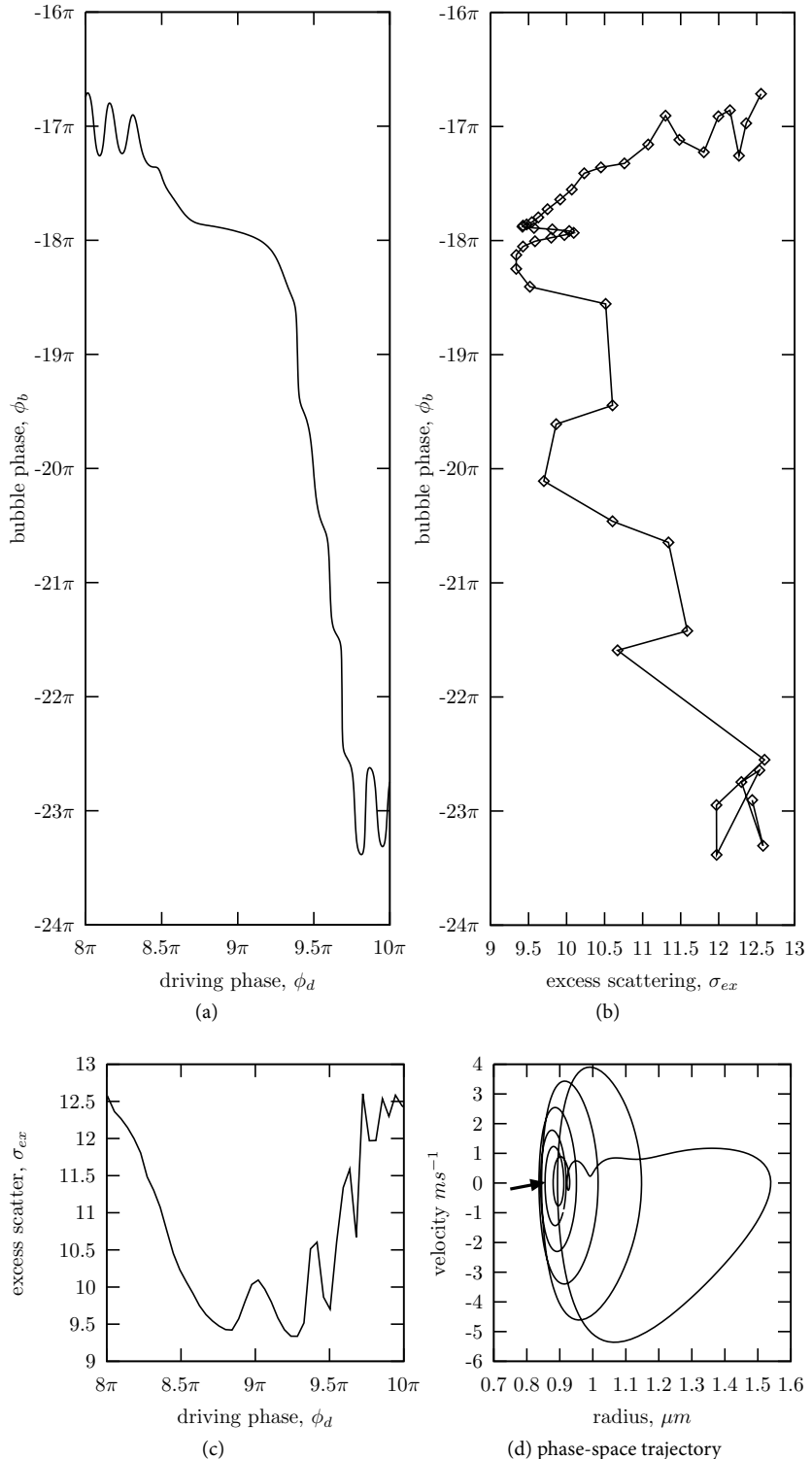


Figure 5.8: The relationship between ϕ_d and ϕ_b from Figure 5.7 is plotted in (a) for a 2π segment. This maps the excess scattering cross section σ_{ex} from being a function of the driving phase in (c) to a function of the bubble's phase in (b). Figure (d) plots the phase-space trajectory of the bubble in response to the driving pulse (without the imaging wave). The arrow indicates the location of the trajectory where the bubble's phase is 17π .

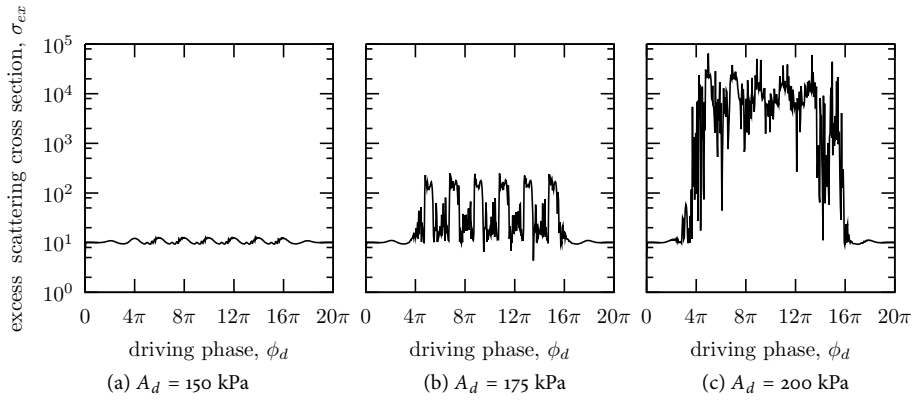


Figure 5.9: The excess scattering cross section for three different pressures. The diameter of the bubble is $2 \mu\text{m}$.

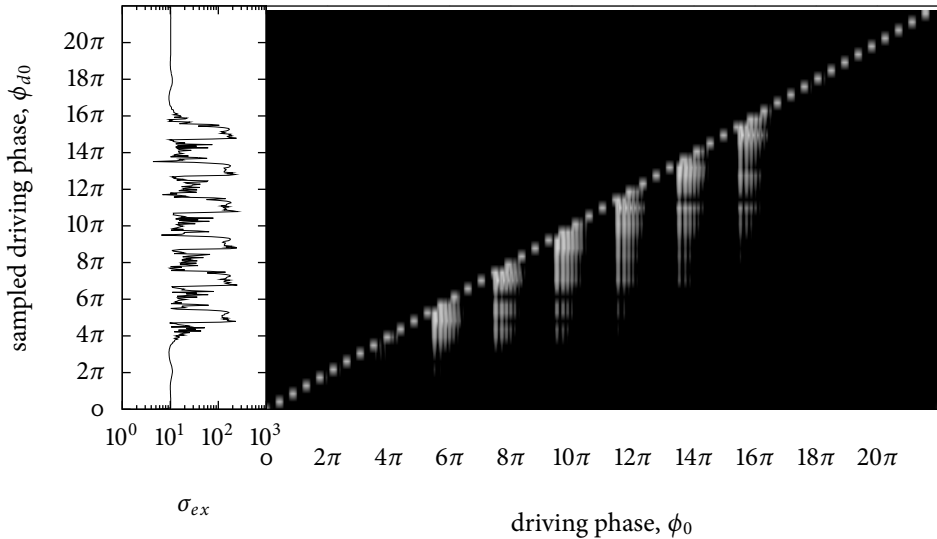


Figure 5.10: The excess pressure and the excess scattering cross section as a function of ϕ_{d0} and ϕ_d for a $2 \mu\text{m}$ -diameter bubble pulsated with a driving pressure of 175 kPa .

section.

5.2.2 THE EXCESS PRESSURE AS A FUNCTION OF THE DRIVING AMPLITUDE

The driving amplitude strongly affects the excess scatter. In Figure 5.9 the excess scattering cross section is plotted a driving wave of 175 kPa, 200 kPa, in addition to the 150 kPa evaluated in section 5.2.1.

At the low pressure of 150 kPa the excess scattering cross section is periodic with a near sinusoid. Even though the response is already harmonic the perturbation to the phase-space orbit rapidly decays, as is seen by the short lived (less than 1 cycle of the driving wave) excess pressure signals in Figure 5.7.

At the higher pressure of 175 kPa the scattering is still periodic but is an order of magnitude greater when the bubble is expanded to when it is compressed. This is not due, unfortunately, to a huge phase-dependence in the scattering of the bubble, but rather due the inclusion of phantom bubbles in σ_{ex} , which seen in Figure 5.10. The preferential appearance of phantom bubbles in the expansion phase was anticipated in section 5.1.3.1.

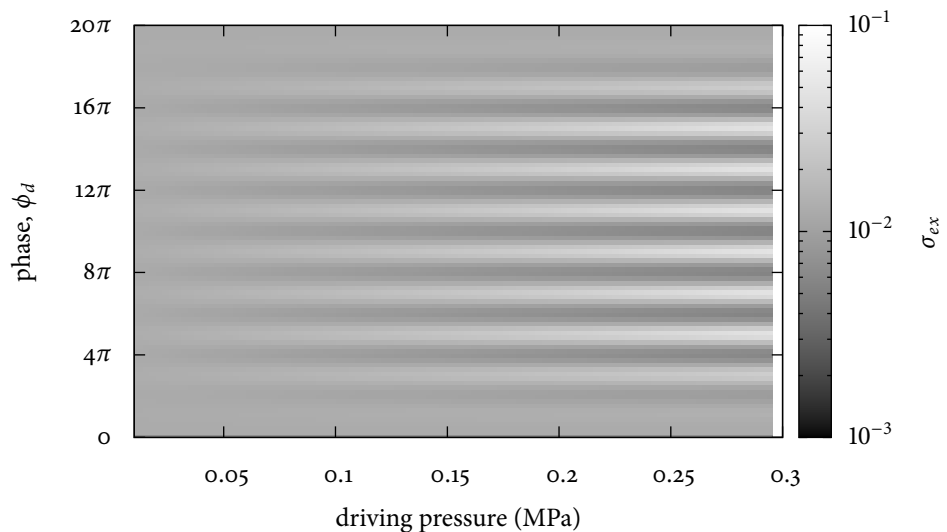
At the higher still pressure of 200 kPa the scattering is swamped by phantom bubbles, and while the scattering is still broadly periodic, it has become somewhat unpredictable, varying widely for very closely related sampled phases.

To understand how the driving amplitude affects the scattering more generally, we plot σ_{ex} as a function of the phase ϕ_{d0} and the driving amplitude. This is calculated for two bubble radii in Figure 5.11. In (a) the radius is $0.1 \mu\text{m}$ and in (b) the radius is $1.0 \mu\text{m}$. For small bubbles the phase relationship of the scattering is both simple and uniform for all driving pressures between 0 and 300 kPa, when driven at 0.5 MHz. However, the situation changes radically at the larger radius in Figure 5.11b.

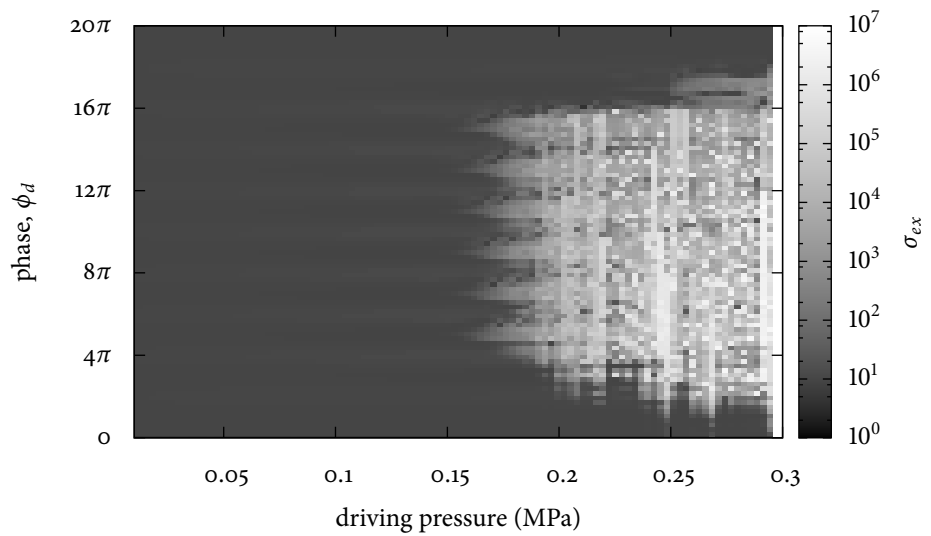
5.2.3 THE EXCESS PRESSURE AS A FUNCTION OF THE RADIUS

To understand the role of the bubble's radius of the excess scattering cross section, σ_{ex} is plotted as a function of ϕ_{d0} and a in Figure 5.12.

The most interesting feature of this plot is the fork in the phase dependence for bubbles



(a) $a = 100 \text{ nm}$



(b) $a = 1 \mu\text{m}$

Figure 5.11: The excess scattering cross section as a function of the driving phase and the driving pressure for two different bubble radii.

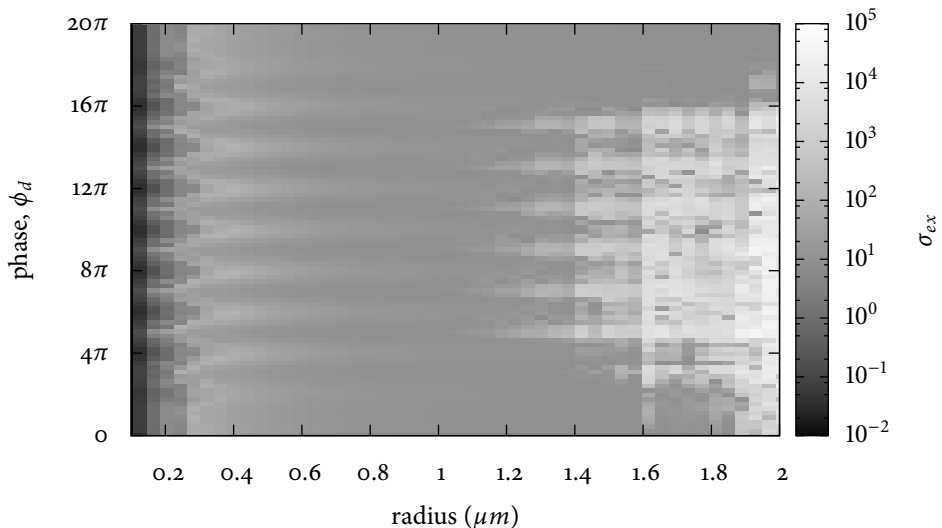


Figure 5.12: The excess pressure scattering as a function of the driving phase and the radius.

with a radius of about $0.3 \mu\text{m}$. Below this radius the scattering is maximal when ϕ_{d0} is an odd multiple of π , or when the bubble is at its largest size. Above $0.3 \mu\text{m}$ the scattering is maximal when ϕ_{d0} is an even multiple of π , or when the bubble is small. Such π radian changes in phase occur at resonance, and we saw in Figure 5.3 that a 300 nm bubble is resonant at 20 MHz . When the bubble is below $0.3 \mu\text{m}$ the scattering increases simply due to the bubble's increased size. Above the resonance the scattering is increased when the bubble is shrunk back towards resonance.

Radii above $1.2 \mu\text{m}$ start to approach the resonance of the driving wave. The phase space trajectories then become less stable to perturbations by the imaging wave and the scattering starts to increase again when the bubble is expanded. Above $2 \mu\text{m}$ the phase response to the driving wave starts to shift with this second resonance, and the phase relation breaks down.

Table 5.2: The bounds for the optimised parameters

	Minimum	Maximum	Step-Size
f_d	0.25 MHz	1 MHz	0.05 MHz
f_i	15 MHz	40 MHz	2 MHz
A_d	0.01 MPa	0.4 MPa	0.05 MPa
A_i	0.5 MPa	1.0 MPa	0.05 MPa
ϕ_{d0}	$2m\pi^a$	$2(m+1)\pi^a$	0.1

^a Where m indexes the central cycle in the driving pulse.

5.3 EXPLORING THE WHOLE PARAMETER SPACE

Hitherto we have been taking two dimensional slices out of a six dimensional parameter space. While the results have so far not been unexpected, general conclusions are difficult to draw - for it could be that for different combinations of the parameters the behaviour is very different.

In this section we explore the parameter space more fully, although we do so only for the 200 nm-diameter bubbles that we hope to nucleate. Since drawing evenly spaced samples from a five dimensional parameter space is computationally prohibitive² we must be selective as to which points are interesting. The points that we wish to preferentially sample are those from regions of high scattering.

To do this we use the Metropolis-Hastings algorithm, a simple Markov-Chain-Monte-Carlo technique, that implements a preferential random walk through the parameter space. After many steps, the probability of the walk being in any location is proportional to the value of the excess scattering cross section.

We are interested in the values of the parameters that are relevant for imaging bubbles that have been nucleated. The random walk is therefore bounded to the ranges given in Table 5.2.

²Each sample takes about 1 s to evaluate on a standard desktop, from which it follows that a coarse $100 \times 100 \times 100 \times 100 \times 100$ grid would take about 3000 years to evaluate.

5.3.1 THE METROPOLIS-HASTINGS METHOD

The Metropolis-Hastings method (as described by MacKay^[69], for example) is a Markov-chain random walk, which means that every new sample is calculated (stochastically) from the previous samples drawn. The excess scattering cross section is function of its position in the parameter space, denoted by the vector $\mathbf{x} = \{f_d, f_i, \dots, \phi_{d0}\}$. The i^{th} sample is at the location \mathbf{x}_i , where i is the position in the sample-chain.

For the random walk to converge to the distribution σ_{ex} , it is necessary for the difference in σ_{ex} between two steps to be balanced by the probability of making the step. If $Q(\mathbf{x}_{m+1}|\mathbf{x}_m)$ is the probability of a step from the position \mathbf{x}_m to \mathbf{x}_{m+1} , and $Q(\mathbf{x}_m|\mathbf{x}_{m+1})$ is the probability of going from \mathbf{x}_{m+1} to \mathbf{x}_m , then the *detailed balance* or *reversible* condition requires that

$$Q(\mathbf{x}_{m+1}|\mathbf{x}_m)\sigma_{\text{ex}}(\mathbf{x}_m) = Q(\mathbf{x}_m|\mathbf{x}_{m+1})\sigma_{\text{ex}}(\mathbf{x}_{m+1}). \quad (5.13)$$

This condition requires that Q be dependent only on its current location.

The Metropolis-Hastings algorithm, at a position \mathbf{x}_m , makes a proposal for \mathbf{x}_{m+1} by drawing a sample at, \mathbf{x}' . To ensure detailed balance, this proposal is accepted (so that $\mathbf{x}_{m+1} = \mathbf{x}'$) with the probability

$$a = \frac{\sigma_{\text{ex}}(\mathbf{x}')}{\sigma_{\text{ex}}(\mathbf{x}_m)} \frac{Q(\mathbf{x}_m|\mathbf{x}')}{Q(\mathbf{x}'|\mathbf{x}_m)}. \quad (5.14)$$

If $a \geq 1$ then the sample at \mathbf{x}' is accepted. If the sample is rejected then the chain doesn't move, with $\mathbf{x}_{m+1} = \mathbf{x}_m$.

5.3.1.1 The distribution $Q(\mathbf{x}|\mathbf{x}^{(m)})$

The simplest distribution from which to draw the next step is a multivariate Gaussian,

$$Q_G(\mathbf{x}|\mathbf{x}_m) = \sqrt{\det(\mathbf{C}/(2\pi)^N)} \exp\left(\frac{1}{2}(\mathbf{x}^T \mathbf{C} \mathbf{x})\right), \quad (5.15)$$

where \mathbf{C} is the inverse of the variance-covariance matrix, of dimension N , and $\det \mathbf{C}$ symbolises the calculation of the determinant. However, this distribution is unsatisfactory because it is impossible to impose the bounds of Table 5.2 upon a Gaussian. Instead of a Gaussian, therefore, we choose a Gaussian shaped distribution that is curtailed to zero outside of our bounds,

$$Q(\mathbf{x}|\mathbf{x}_m) = \begin{cases} \frac{1}{Z} \exp\left(\frac{1}{2} (\mathbf{x}^T \mathbf{C} \mathbf{x})\right) & \text{if } \mathbf{x} \text{ is within bounds} \\ 0 & \text{otherwise} \end{cases} \quad (5.16)$$

The normalisation, Z , has to be evaluated numerically.

Rather than considering the full inverse variance-covariance matrix, we further restrict \mathbf{C} to be diagonal,

$$\mathbf{C} = \begin{pmatrix} \sigma_{f_d}^{-2} & \cdots & 0 \\ \vdots & \ddots & \\ 0 & \cdots & \sigma_{\phi_d}^{-2} \end{pmatrix} \quad (5.17)$$

where σ_{f_d} , etc. are the standard deviation assumed for the scattering cross section along the stated axis. This standard deviation controls the step size of the random walk in that dimension.

Diagonalising \mathbf{C} implies that Q is separable,

$$Q(\mathbf{x}|\mathbf{x}_m) = \frac{1}{Z_{f_d}} \exp\left(\frac{x_{f_d} - f_{d,m}}{2\sigma_{f_d}}\right) \cdots \frac{1}{Z_{\phi_d}} \exp\left(\frac{x_{\phi_d} - \phi_{d,m}}{2\sigma_{\phi_d}}\right) \quad (5.18)$$

where $f_{d,m}$ is the driving frequency of the m^{th} sample and the product runs over all the parameters. The standard deviations must be provided as guesses to the algorithm at the start and the values we chose are given in the final column of Table 5.2. If they are chosen to be too small then the steps taken are mostly accepted but the walk takes a long time to explore the space. If they are too large then the steps too often try to leave a region of high σ_{ex} , and so most steps are rejected, again leading to a slow exploration. The optimum step size leads to an acceptance probability of about 50%.

5.3.1.2 Skilling's Leapfrog Speedup

The Metropolis-Hastings method is a random walk, and so it is slow. The distance explored goes to the square root of the number of samples.

John Skilling proposed a simple ‘leapfrog’ speedup to Markov-Chain-Monte-Carlo methods which is discussed by MacKay^[69]. Rather than follow the trajectory of a single Markov-chain, a set of chains (say 10) are run simultaneously. After a number of steps, chosen here to be 10, the current position of one of the chains chosen at random, $\mathbf{x}_{(1)}$, is invited to leap over the end position of another randomly chosen chain, $\mathbf{x}_{(2)}$.

That is

$$\mathbf{x}'_{(1)} = \mathbf{x}_{(1)} + 2(\mathbf{x}_{(1)} - \mathbf{x}_{(2)}). \quad (5.19)$$

Whether this state is accepted or not is decided once again by the Metropolis rule. When the step size is too small among some of the dimensions the leapfrog helps by enabling exponential growth to expand into the space. This reduction in the random walk behaviour can greatly speed up the exploration of the sample space.

In this thesis the steps of the metropolis part of the algorithm are distributed on a 10 processor cluster so that they are calculated simultaneously.

5.3.2 PROJECTIONS IN PARAMETER SPACE

Of the 20 independent two dimensional projections of a 5 parameter space, we concentrate on the 4 that depend on the driving phase. These are plotted in Figure 5.13. Each of the half-million samples is represented by a dot and the colour depicts the value of the excess scattering cross section, σ_{ex} . The dot size is chosen in an attempt to fill the graph - and reduce their *pointillism*-like appearance. Since the parameter space preferentially selects regions of high σ_{ex} , the background (where no sample has been made) is by default painted to zero (black). Since we are interested in regions of higher σ_{ex} , the samples have been re-ordered so that the brightest get painted at the top, irrespective of the samples depth within the projection.

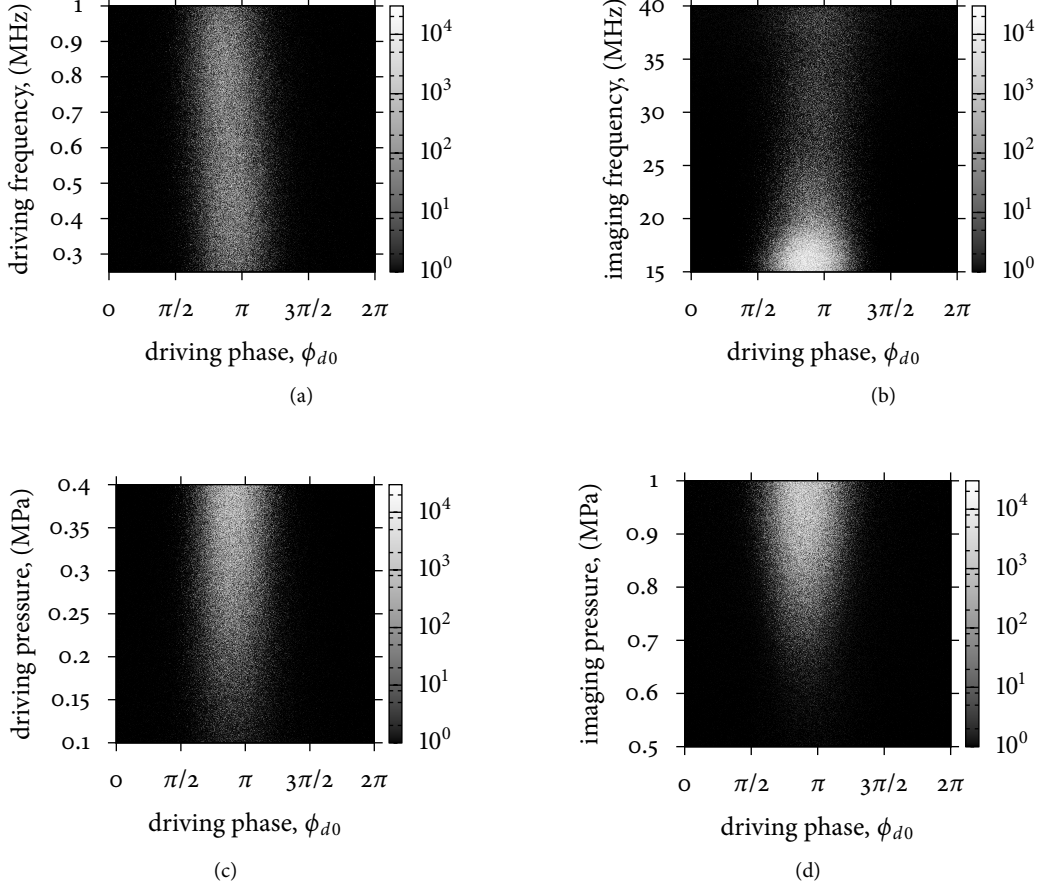


Figure 5.13: Projections of the data from the whole of parameter space. The data is ordered so that higher values of σ_{ex} are drawn above lower values.

The first thing to notice from Figure 5.13 are the values of the excess scattering cross section. For many of the samples they are huge, which in line with section 5.2.2 we interpret as implying the occurrence of phantom bubbles appear in the image. In section 5.1.2 we argued that the phantom bubbles should appear most readily in the expansion phase of the driving wave because this is where the non-linearity in the bubble's expansion should be accentuated. Supposing that the driving wave pulsates the 100 nm-radius bubble linearly, we find from Figure 5.3 that the maximum scatter should occur at $\phi_{d0} = \pi - 0.63 = 2.5$ radians. With the half-million samples plotted this slight asymmetry is easy to see.

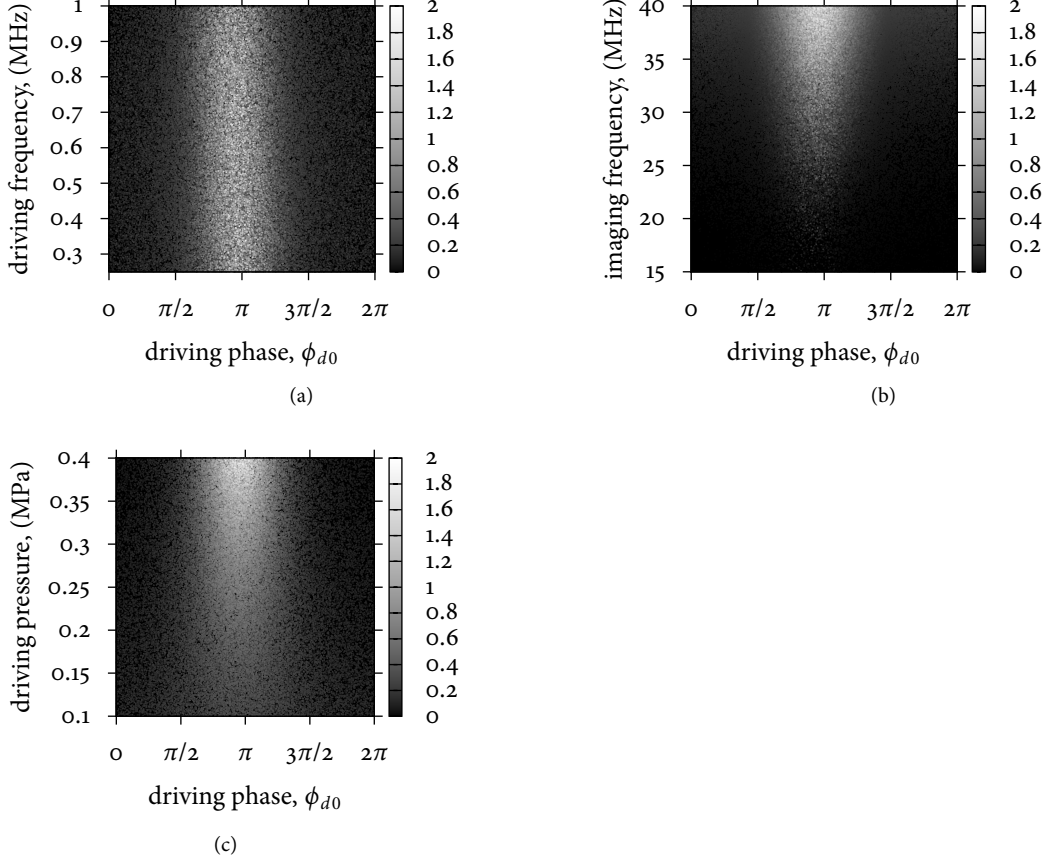


Figure 5.14: Projections of the data from the whole of parameter space. The data is ordered so that higher values of σ_{ex} are drawn above lower values.

The second thing to notice from Figure 5.13 is how remarkably well behaved the parameter space is. The phase dependence of the driving frequency, driving pressure, and imaging pressure is contained, in the projection, no unexpected hot-spots. The only unexpected result is that excess scattering cross section was high for the ‘low’ frequency of 18 MHz (Figure 5.13b). From Figure 5.3 we do not expect the resonance to below 40 MHz. From Figure 5.13d we see that such points occur only at high imaging pressures. One interpretation for (b) is that at these high pressures the bubble responds non-linearly to the imaging wave and perturbs the bubble out of orbit - resulting in the phantom bubbles seen in Figure 5.13.

The huge excess scattering cross sections found in Figure 5.13 dominate the random-

walk. To understand how the scattering is influenced by the in the absence of phantom bubbles we repeat the analysis but this time with the imaging pressure is set to 0.5 MPa. The 3 projections over the 4-dimensional space are shown in Figure 5.14.

The main difference between Figure 5.14 and Figure 5.13 is in the frequency response to the imaging wave. In Figure 5.14c the scattering increases with frequency as expected for a bubble with such a high resonance frequency.

The driving frequency, driving pressure, and imaging pressure all increase when the bubble is expanded, which repeats the result from Figure 5.12 for a 100 nm bubble.

5.3.3 THE OPTIMUM PARAMETERS

To find the optimum parameters for maximising σ_{ex} samples are drawn from the random walk through parameter space. To do so in an unbiased way requires enough time to be given for the Markov-Chains to explore the entire region of high σ_{ex} . For a random walk in 1 dimension, the minimum number of accepted samples, T_{\min} , is found from the length-scale of the region of high scatter, L , and the step size σ ,

$$T_{\min} = \left(\frac{L}{\sigma} \right)^2. \quad (5.20)$$

In N dimension, T_{\min} is found from the dimension with the largest such ratio.

From Figure 5.13 and Table 5.2 we see that largest ratio is the phase direction, with

$$T_{\min} \approx \left(\frac{\pi}{0.1} \right)^2 \approx 1000 \quad (5.21)$$

Since in the simulation only 8% were accepted (the step-sizes, it seems, were a bit large), this means a minimum of 12500 steps must be evaluated between samples to ensure independence.

The Leapfrog speedup reduced the random walk behaviour of the Metropolis-Hastings algorithm. Therefore, this ‘minimum number’ is considered to be acceptable for drawing independent samples. To give the random walk time to ‘burn in’ to the region are

Table 5.3: The optimal parameters (including the imaging pressure amplitude)

		Optimal Value
driving frequency	f_d	$0.5 \text{ MHz} \pm 0.2 \text{ MHz}$
imaging frequency	f_i	$24 \text{ MHz} \pm 7 \text{ MHz}$
driving amplitude	A_d	$0.28 \text{ MPa} \pm 0.11 \text{ MPa}$
imaging amplitude	A_i	$0.91 \text{ MPa} \pm 0.12 \text{ MPa}$
driving amplitude	ϕ_{d0}	2.55 ± 0.81
excess scattering cross section	σ_{ex}	$1500 \mu\text{m}^2 \pm 2900 \mu\text{m}^2$

of high σ_{ex} , 25000 steps are taken before the first sample is drawn.

The average of 27 samples is given in Table 5.3. First notice that our predicted phase angle of 2.5, based on linear response to the driving wave, is centred within the sampled estimate of 2.55 ± 0.81 .

Secondly, the huge standard deviation associated with σ_{ex} is indicative that there are many small pockets of high scattering cross section (where phantom bubbles manifest themselves) in a sea of much lower amplitude. This interpretation suggests that the samples are being drawn from two different distributions, depending whether phantom bubbles are present or not.

Table 5.4: The optimal parameters ($f_d = 0.5 \text{ MPa}$)

		Optimal Value
driving frequency	f_d	$0.65 \text{ MHz} \pm 0.21 \text{ MHz}$
imaging frequency	f_i	$33.0 \text{ MHz} \pm 5.8 \text{ MHz}$
driving amplitude	A_d	$0.25 \text{ MPa} \pm 0.12 \text{ MPa}$
driving amplitude	ϕ_{d0}	3.17 ± 1.36
excess scattering cross section	σ_{ex}	$0.34 \mu\text{m}^2 \pm 0.31 \mu\text{m}^2$

The data taken when the imaging pulse is 0.5 MPa are much better behaved, as are seen

in Figure 5.14. In Table 5.4 the averages from 81 samples are calculated. In this case the asymmetry in the driving phase is less clear, although the predicted phase of 2.5 is still within 1 standard deviation.

5.4 DISCUSSION

This chapter has explored the dynamics of a bubble when imaged with two acoustic waves, where the pulses are of very different frequency and are generated by two transducers with a limited frequency response. We explicitly considered the role of the frequency and amplitude of the two waves, the bubble's radius, and the phase of the driving wave sampled by the imaging wave, ϕ_{d0} . This final parameter is of particular interest to us, as it gives the possibility of the driving wave manipulating the bubble to a particular location in its phase-space in preparation of the imaging wave.

In section 5.1.3 we introduced a two pulse technique to evaluate the excess pressure generated by an imaging wave. The purpose of this was to eliminate the bubble's response to the driving wave that is picked up by the imaging transducer. Temporal ordering was thereby reintroduced into the image phantom bubbles may still be visible after the arrival of the imaging wave.

The ringing occurs when the imaging wave perturbs the bubble's phase-space trajectory sufficiently to change the orbit of the bubble. This effect can be diminished by balancing the expansion and contraction induced in the bubble by the imaging wave, as was found in section 5.1.2. When the bubble is being expanded by the driving wave the nonlinear response is accentuated and the effect of the perturbation is greater, as observed in section 5.2.2

In section 5.2 we explored how the excess scattering cross section varies with incident driving phase, ϕ_{d0} , the driving pressure and the bubble radius. We found that a bubble that is smaller than its resonant radius scatters more strongly when it is grown by the driving wave; a bubble that is larger than its resonant radius scatters more strongly when it is shrunk. For a 100 nm-radius bubble, this behaviour was systematic of the entire the parameter space explored in Table 5.2, as was demonstrated by the projections

in section 5.3.1. We confirmed also that the phase relationship with ϕ_d breaks down when bubble starts to resonate under the influence of the driving wave.

Finally, in section 5.3.1, the optimum parameters for imaging a 100 nm-radius bubble were obtained with a Monte-Carlo technique. The results are summarised in Table 5.3 and Table 5.4. The onset of phantom bubbles can increase the scattering cross section observed by orders of magnitude, however, the exact locations in parameter space where such scattering occurs is very hard to predict.

PART III

EXPERIMENTAL

In part II it was shown, with a computational model, that a low frequency wave can alter the response of a bubble to a higher frequency pulse.

This model is tested experimentally in this part of the thesis. Chapter 6 introduces the methodology of the experiment. Chapter 7 then describes the experiments performed on bubbles induced from the Type III and Type IV nucleation of water.

EXPERIMENTAL DESIGN

6.1 INTRODUCTION

Chapter 5 found that a low frequency wave may be used to tune a bubble's size to best match the characteristics of the imaging wave. The imaging frequency can then be chosen with greater regard for the application rather than being constrained by the resonance frequency, and therefore the size, of the bubble. The constraints of resolution and imaging depth already make for difficult trade-offs, and so decoupling the bubble size from the imaging frequency makes for a powerful enhancement to contrast imaging.

In this chapter the experimental procedure to test the ideas of Chapter 5 is detailed.

6.2 ALIGNMENT OF THE TWO PULSES

This thesis uses two separate ultrasound transducers to generate the cavitating and imaging waves. This brings the advantage of flexibility: the characteristics of the cavitating and imaging waves are completely decoupled. The frequency, pulse-duration, focal depth and duty-cycle of each pulse can be chosen and interchanged independently, and without compromise with regard to a crystal's bandwidth or curvature.

To investigate the phase-relationship between the driving and imaging pulses when incident upon a bubble, the two waves must pass simultaneously through a bubbly fluid situated at the common focus. In principle, the two transducers could be at any angle, ϕ , with respect to each other. However, having the transducers co-axial (where

$\phi = 0^\circ, 180^\circ$) is optimal because the sampling precision in the axial direction is vastly superior. This is because the sampling rate in the axial direction is determined by the rate at which samples can be digitalised, whereas in the orthogonal direction the sampling precision is determined by the beam width of the imaging transducer. Any arrangement other than co-axial will therefore deteriorate the sampling precision by a factor of $\sin(\phi)$.

The two co-axial arrangements both have their advantages and disadvantages. The advantage of having the two transducers facing each other ($\phi = 180^\circ$) is that all phase relationships between the two pulses are explored in a single shot. The disadvantage is that the driving pulse is incident upon the imaging transducer even if no scattering occurs. This directly transmitted signal is not generally dominant, however, so long as the band-widths of the driving and imaging crystals do not greatly overlap.

If the two crystals are interleaved into the same transducer ($\phi = 0^\circ$) then the two pulses traverse with each other. There is no problem with either signal being directly transmitted. However, each phase relation of the two pulses needs to be carried out individually and it is difficult to maintain a population of micron-sized bubbles in a consistent state for any length of time. A further problem is that the phase relationship between the two pulses changes as a function of density; a high frequency pulse *surfing* on a compression of a lower-frequency pulse travels at a greater speed than when timed with a rarefaction. This effect is measurable and is the basis of SURF-imaging^[3]. Finally, interleaving two crystals into the same transducer generally requires bespoke transducers and comes at a considerable cost. For these reasons, the angle $\phi = 180^\circ$ is chosen in this thesis.

6.3 THE SOURCE OF BUBBLES

There are a number of microbubble sources that could be used to test the influence of the low frequency wave on the imaging wave.

A bubble generated from a perfluorocarbon emulsion:

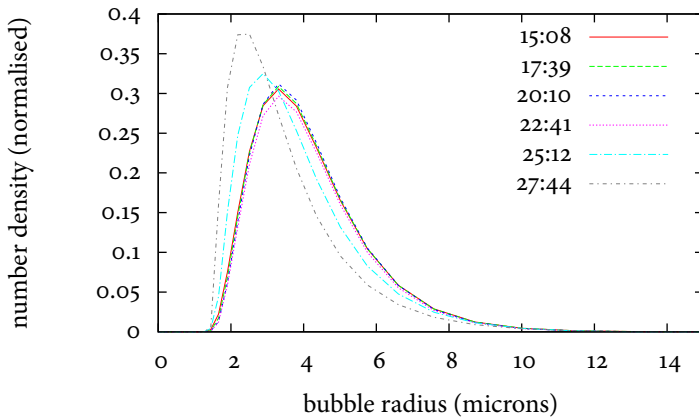


Figure 6.1: SONOVUE distribution at various times after manufacture (in minutes).

It seems likely that perfluorocarbon droplets will eventually be able to leave the blood and be vapourised *in situ* to generate a contrast agent (see chapter 1). Testing two wave imaging using a vapourised perfluorocarbon emulsion would therefore represent a natural end to this research project: the technique tested in the domain in which it is most useful, a cavitating wave acting upon a sub-micron bubble. Perfluorocarbon emulsions do not, however, represent a natural beginning.

The technology in developing such contrast agents is still young. Most of the success so far has been with larger droplet sizes (greater than 400 nm^[14;57;92]) while manufacturing smaller droplet sizes, required for producing an extravascularised bubble of less than 400 nm has remained troublesome^[1;63]). The pressures that have hitherto been used to generate the bubbles are 3 MPa for a 0.5 MHz wave^[94], far in excess of those used in diagnostic applications, with cavitating pulse lengths of 10 s. Such pressures require the emulsion to be prepared in exceptionally clean water to be sure that the bubbles generated by the driving wave are not simply from heterogeneous nucleation of the water. Furthermore, any surfactant used to stabilise the emulsion must be known not to also stabilise any bubble formed in the manufacturing process, or to itself form a nucleating centre. Research is being carried out by other groups^[1;14] to reduce

the pressure required for to cavitate a perfluorocarbon droplet by mixing different perfluorocarbons.

Commercially available microbubbles:

The difficulties resulting from the novelty of perfluorocarbon emulsions are not present for commercial available microbubbles. Microbubble contrast agents have been licensed since 1994^[28], and SONOVUE (Bracco) is currently licenced for clinical use in the EU. Both its size distribution and its resonances are well characterised.

However, the size distribution of commercial microbubbles causes problems in this experiment. Firstly, the mean radius of the bubbles is greater than a micron. This means that the bubbles float, albeit slowly, making a distribution of bubbles that is homogeneous both spatially and temporally difficult to achieve. Even if the bubbles are circulated, the larger bubbles are gradually lost in the experiment. The results of a preliminary experiment showing the size distribution of SONOVUE circulating through a Mastersizer is shown in Figure 6.1. Since microbubbles are highly attenuating to ultrasound the pressure field in the sample changes as the distribution changes, meaning that the response becomes a complicated function of depth.

Secondly, commercial microbubbles have a fairly broad distribution of sizes. This causes problems because the phase offset between the bubble's pulsations and cavitating wave is a function of the bubble's size (see chapter 5). The scale of this problem can be understood from Figure 5.12 on page 114. Not only would we be trying to find the excess scattering cross-section of a bubble in the complicated region corresponding to large bubble radii, we would be trying to perform a weighted average over that region.

Finally, the use of microbubbles forces the experiment away from the domain where a submicron bubble is generated with a high pressure wave.

Heterogeneous nucleation of tap water:

The heterogeneous nucleation of tap water is perhaps the simplest method of

generating bubbles. Indeed, it makes a good control method to the more elaborate techniques above. It is also the method that most closely matches the ideal parameters for cavitating an extravascular contrast agent. With relatively short pulses (less than 10 cycles) at pressures that are achievable with diagnostic ultrasound transducers (less than approximately 1 MPa peak-negative pressure) gas entrapped in stabilised microbubbles and motes can be released^[116].

The critical radius as a function of acoustic pressure for an air bubble in water was estimated in chapter 2. If the negative pressure is 1 MPa then the diameter of the bubble is approximately 300nm (Figure 2.1a on page 19). This is the size that would be expected for extravascular contrast agent, achieved with a pressure that would be desirable for an extravascular contrast agent. Furthermore, tap water is homogeneous and is stable indefinitely once it has reached a stable equilibrium, at least up until the sample has been pulsed with an ultrasound wave.

This thesis uses tap water as a source of bubbles. A full list of the experimental objectives is given in section 6.5 and the experimental methodology designed to meet these objectives is given in section 6.6.2.

6.4 PARAMETERS UNDER EXPERIMENTAL CONTROL

The main experimental parameters that are subject to experimental control are:

1. The relative phase between the low-frequency and imaging wave.
2. The pressures of the two waves.
3. The frequencies of the two waves.
4. The pulse-length of the two waves.

All variables other than the pulse length were investigated computationally in chapter 5

The first parameter is well sampled by virtue of the experimental setup. The two waves pass through each-other and so in *every* image *all* phases between the two waves will be sampled.

Sampling the pressure of the low-frequency wave is also straight-forward by choosing a wide range of driving pulses to vary the peak pressure at the focus. In addition, if a 2 dimensional image is formed with a scanner, then the spatially varying pressure field of the low frequency wave will be imaged in *every* image.

We choose the frequencies of the two waves when choosing the transducers. The choice, however, is not completely free. The high frequency pulse ideally should last for only a small fraction of the period of the low frequency wave. In addition, when the difference in frequency between the low and high frequency transducers becomes small the direct transmission of sound between the transducer's becomes a problem for the anti-parallel setup of the transducers. Imaging frequencies of between 7.5 and 20 MHz were tried in preliminary studies along with low-frequency waves of between 0.5 and 2 MHz. The results presented here were used a 0.5 MHz low frequency wave and a 20 MHz imaging wave.

The pulse length of the imaging wave should be short, although when imaging is achieved with a commercial scanner then this parameter is often fixed. The pulse length of the low frequency transducer is readily set. To avoid bubbles growing (by rectified diffusion), fusing (by Bjerknes forces) and collapsing (by instabilities in the oscillations) the low-frequency pulse should also be short. However, to reduce forward transmission the frequency output of the low frequency wave should not be too broad-band. 10 cycles is used in these experiments.

6.5 EXPERIMENTAL OBJECTIVES

This thesis has four experimental objectives that aim to test the predictions made in the earlier parts of the thesis.

1. Determine whether bubbles can be evacuated from tap water with a driving wave,

and subsequently detected with a higher-frequency pulse.

2. Determine whether an evacuated bubbles can be *imaged by pulse-echo* with a higher-frequency pulse.
3. Determine if the precise location of the bubble can be determined. In particular, can the excess scatter introduced in chapter 5 be shown to have experimental merit?
4. Determine whether the acoustic Keller-Miksis equation derived in chapter 4 improves the modelling of the returned echo.

The objectives are incremental in that the latter depend upon the former. The first is the most straightforward. The generation of bubbles in dirty water is familiar to most practitioners of ultrasound and the only technical difficulty is in timing the imaging gate appropriately to detect the wave.

The second question is much more difficult. For the second question we wish to show that the evacuated bubble interacts acoustically with the imaging wave and that we can detect the high frequency echo. Sound that is radiated when the bubble is generated, or forward scattered from the driving wave, is no longer of interest. The third asks whether the excess pressure technique of chapter 5 is a viable means of locating a bubble, and thereby conclusively demonstrating the acoustic interaction of nucleated bubble with the imaging wave.

The final two questions are the most challenging of all because they require the measurement of bubble specific parameters from within larger population. Such questions will only be answerable if the large spread found in parameters such as the radius (Figure 6.1) is not representative of the spread found in the bubbles that interact acoustically. Since in this thesis the focus is on diagnostic pulses, which are typically limited to being a few cycles long, questions three and four are not expected to yield good results. The range of frequencies contained in the pulses are too great to hope for narrow resonance characteristics in the population of generated bubbles.

6.6 EXPERIMENTAL PROTOCOL

The broad design of the experiments to test these objectives are now presented.

In section 6.6.1, a preliminary study is discussed that answers question 1 in the affirmative. It is found, however, that the preliminary study is not capable of determining the answer to the second question, namely, whether the high frequency transducer actively imaging the generated bubbles or whether it is simply passively detecting high harmonics of bubbles oscillating due the driving wave. This prompts some changes in experimental design that are discussed in section 6.6.2.

6.6.1 PRELIMINARY STUDY: THE GENERATION AND DETECTION OF BUBBLES IN DIRTY WATER

The primary goal of the preliminary study is to determine whether bubbles can be evacuated from motes in tap water with a low frequency wave, and whether evidence for this can be detected with a high frequency transducer.

For this purpose a 0.5 MHz transducer (TMS, focal length: 50 mm) was chosen to evacuate the gas from the water, and a 20 MHz (Panametrics, focal length: 20 mm) transducer was used for imaging. These transducers were chosen for a number of reasons:

1. It was hoped that the frequency ratio of 40 between these transducers would help eliminate direct transmission from the driving wave to the imaging transducer.
2. 0.5 MHz was chosen for the driving wave because it is below the principle resonances of the bubbles that are expected to be evacuated in the fluid (Figure 5.3). The motivation for being below the principle resonance comes from chapter 5 where it was found that the interactions between the driving and imaging waves become hard to interpret at resonance.
3. 20 MHz was chosen for the imaging wave because 20 MHz should resonate free gas bubbles of about 300 nm (Figure 5.3). This is approximately the size of bubble that we ultimately wish to image.

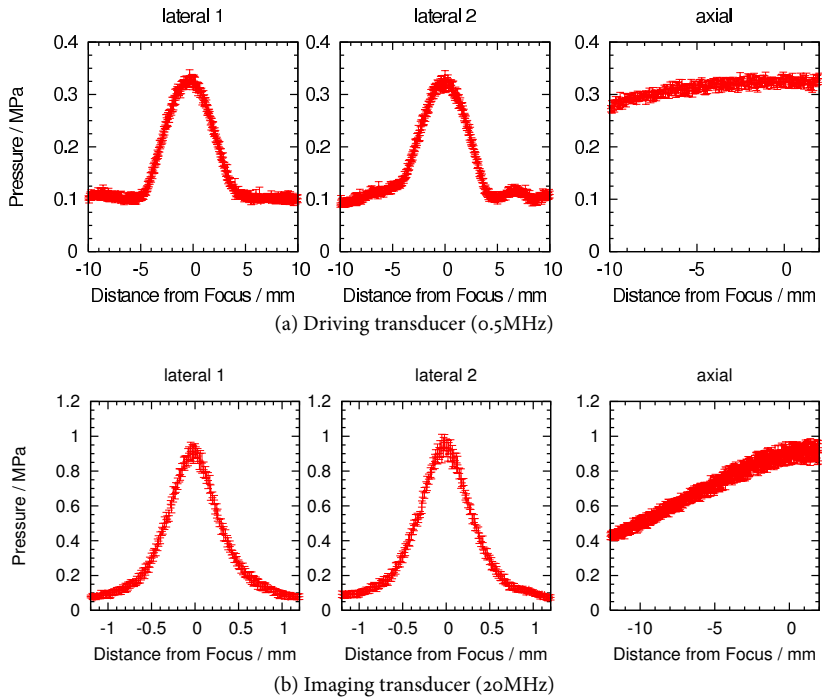


Figure 6.2: The profile along the two lateral and axial direction for the imaging and pumping transducer measured with a membrane hydrophone.

4. Both transducers are focussed. Firstly, this results in an imaging volume that is well located. Secondly, higher driving and imaging pressures can be obtained at the focus than would be possible if the transducers were flat. A plot of the focal widths is provided in Figure 6.2.
5. The 20 MHz transducer was a spare taken from a Cortex Skin Scanner. The transducer can therefore be fixed to obtain M-mode images, or mounted on a pendulum scan-head to obtain B-mode images.

The two transducers were clamped together in a custom made sample holder which ensured that the mechanical focus of the two transducers was coincident. Two mounts for the imaging transducer were made, one that fixed the imaging transducer on axis with the driving transducer, and one that attached to a modified Cortex scanner, enabled the imaging transducer to swing for B-Mode imaging. The cofocus was designed so that it stood in the middle of a sampling volume that could be separated from the

transducer standoffs with Mylar film.

B-mode imaging was chosen for the preliminary study so as to maximise the view of the two wave interaction. The modified Cortex scanner gives output to the frame trigger output, the A-line trigger output, the swing direction of the transducer and the RF data. It has a slow frame rate of approximately 3-4 Hz. The cortex also has a curious although very useful pulse sequence, with two A-line-pulses in rapid (100 microsecond) succession, followed by a large (millisecond scale) interval. This is illustrated in Figure 6.3.

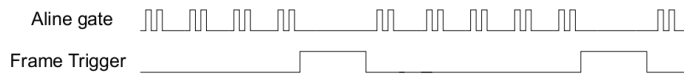


Figure 6.3: The cortex fires two A-lines in quick succession before repeating the sequence after a relatively large pause.

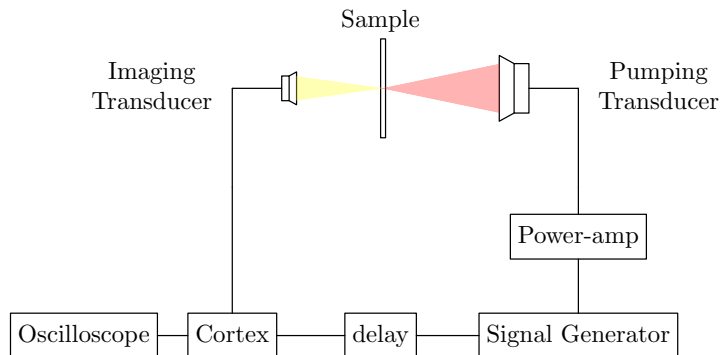


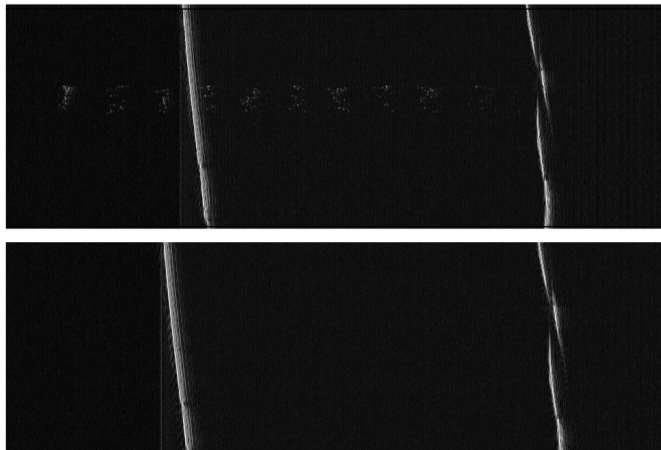
Figure 6.4: Electronic arrangement of the preliminary experiment

Unfortunately the Cortex scanner cannot be triggered, only providing an output to an internal trigger. However, since the focal length of the low frequency transducer is longer than that of the Cortex transducer, the driving transducer needs to be triggered earlier in order for both signals to reach the sample at the same time. The two pulses from the Cortex scanner enable this problem to be overcome. The first pulse of the Cortex A-line doublet is used to trigger a timer delay for the low frequency transducer. The delay is chosen so that the first low frequency pulse arrives at the sample at the same time as the second high frequency pulse. In this way one generates two interleaved images, with adjacent A-lines imaged with the pulse off, and then the pulse on. The

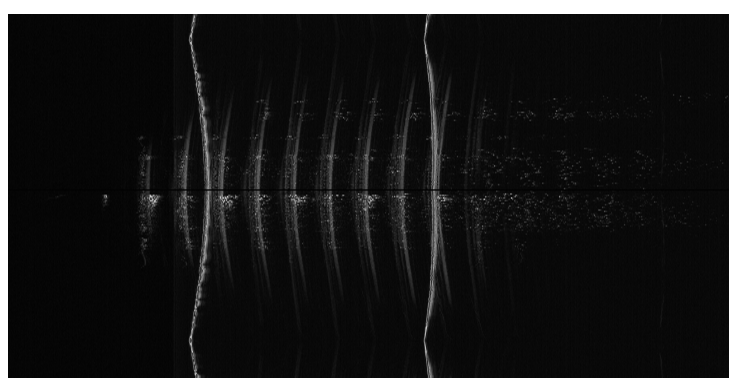
second low frequency pulse (triggered from the second A-line doublet) is ignored. The electronic arrangement of the preliminary experiment is summarised in Figure 6.4.

The pressures were measured with a PA08038 0.5mm SN1328 (Precision Acoustics) needle hydrophone up to a pressure of 0.5 MPa. The measurements were made in degassed water (6.2mg oxygen per litre) at 23 degree Celsius. Above this threshold the pressures were extrapolated from the driving voltage. This was to protect the hydrophone from possible cavitation damage.

6.6.1.1 Results of the preliminary study



(a) Water sample driven at 0.4 MPa. Both the imaging and driving wave are on in the top image. Only the imaging wave is on in the lower image



(b) Water sample driven at 2.2 MPa. Both the imaging and the driving waves are on

Figure 6.5: The Hilbert transform of the imaging radio-frequency data, recovered when the imaging transducer is swung on a pendulum. Please refer to the sub-caption as to whether the pulsing wave was on or not.

Figure 6.5a shows two plots. The images are the Hilbert transform of the RF data along the A-lines obtained from the Cortex scanner. The top image is generated when both the driving wave and the imaging waves are on, when the driving wave is 0.4 MPa. The two lines are the front and rear of the Mylar film, as imaged by the high frequency wave. The lower plot is the same sample but when just the imaging wave is on.

In the top plot of Figure 6.5a one can see banded specks that coincide with the passing driving wave. The temporal interval between the bands is consistent with the frequency of the driving wave. These signals are not present when the driving wave is off.

At 0.4 MPa such signals are common but by no mean ubiquitous. Often such signals are present in only few A-lines (grouped together, as above), sometimes only for a single A-line in the image, and often none are visible at all. At the lower pressure of 0.3 MPa you get such signals but with a lower frequency, at greater pressures they become more common. The 0.4 MPa signal has the property that you see the bubbles at gains that do not pick up the directly transmitted sound. This gives the images its ‘clean’ appearance.

Figure 6.5b plots the image that is obtained with a driving pressure of 2.2 MPa. Regular banding is evident in addition to the stochastic events observed in Figure 6.5a.

6.6.1.2 Interpretation

The regular banding in Figure 6.5b is very stable. It is present only when the driving wave is on, increases in amplitude with the driving wave, and is of the same wavelength as the driving wave. The most natural interpretation is that this portion of the image is the direct transmit of the driving wave arriving on the imaging wave.

The signal from the direct transmit is useful because it indicates the sampling of the compression and rarefaction cycles of the driving wave by the imaging wave. While it must be remembered that the imaging transducer is filtering the frequencies of the received pulse, thereby distorting them in the image, the broad phase of the driving wave is nevertheless evident in Figure 6.5b. Bright pixels indicate a compression in the driving wave.

The bright and stochastic signals that are seen on top of the direct transmission are interpreted as resulting from bubbles in the solution. It is seen that their greatest intensities come in at the beginning of the rarefaction phase of the driving wave - the rebound after the compression. The lack of coherence between adjacent alines indicate that the bubbles are short lived (milliseconds). This is expected from the analysis of chapter 2.

Both Figure 6.5a and Figure 6.5b were driven with a 10 cycle burst from the driving transducer. In Figure 6.5b, however, 16 bands can be counted in the signal. This suggest that the generated bubble survives through for the duration of the driving pulse (microseconds) and interacts with the ringdown of the transducer after its burst. It suggests that the bubbles are not destroyed and reborn on every cycle of the driving wave.

6.6.1.3 *What remains ambiguous?*

Unfortunately a number of questions are not answered by the Figure 6.5a and Figure 6.5b.

The location of the scattering bubble(s): The location of the bubble(s) within the sample is not clear in the experiment.

The signal detected by the imaging wave could result from one bubble, generating an acoustic output with every cycle of the driving wave. Its location, however, could be anywhere along the axis between the two transducers. The interacting bubble is more likely at the focus of the driving wave, due to the greater pressures that exist there, but Figure 6.2a shows that the fall off in axial pressures is quite gradual. The excess pressure technique cannot be applied in this experiment to help determine the location of the bubble. This is because the because the imaging transducer is moving between adjacent alines, and because the imaging transducer fires for every A-line.

Alternatively, the generated signal could be a superposition from many bubbles, again not necessarily at the imaging depth of the high-frequency transducer.

However, Figure 6.5a does provide some evidence contrary to this at low pressures. The 'all or nothing' characteristic evident in that figure suggests that there are not many bubbles contributing to the signal.

The role, if any, of the imaging wave: The more serious ambiguity concerns the role of the imaging wave. It is not clear as to whether the backscatter from the imaging wave is contributing to the images at all.

If the signal is just forward scatter then the experiment is simply doing passive cavitation detection via an overly complicated harmonic imaging setup. In this case there is little relation to the computational analysis of chapter 5 and there is no new technology at work. The result would then be "If you use a sufficiently high pressure you can pulsate a small bubble to generate higher-frequency harmonics".

If, on the other hand, the signal is a combination of forward-scatter and backscatter then it would be a very interesting result for it opens the possibility of manipulating the bubble's acoustic output. We need a way of separating out 'interesting' backscatter from 'dull' forward scatter. This was an issue discussed at length in chapter 5. The way to do this is to subtract an image generated when only the driving wave is present (providing the forward scatter and direct transmit) from an image containing both waves. Then you are left with the contribution from the imaging wave. However, this is impossible with the current experimental setup. Since the driving wave is further from the cofocus than the imaging wave, it must be the driving wave that fires first and triggers the experiment. The Cortex scanner cannot be triggered in this way. Additionally, the technique relies upon both repetitions imaging the same bubble population. The pendulum motion of the Cortex scan head is also therefore inappropriate.

The problem with the preliminary setup, therefore, is that it is impossible to distinguish an interesting result (the driving wave and imaging wave interacting) from a result that contributes very little (harmonic imaging).

6.6.2 THE FINAL EXPERIMENTAL DESIGN

To enable the excess pressure to be plotted one needs:

1. a fixed imaging transducer,
2. a pair of driving pulses, of which one triggers the imaging wave,
3. a way of rapidly switching the imaging transducer from pulse-receive into receive-only mode (the imaging mode)

The first of these is achieved by removing the imaging transducer from the Cortex scanner and fixing it statically in the sample holder.

Controlling the triggering and imaging mode of the two transducers required a considerable change in the electronic arrangement of the experiment.

6.6.2.1 *Delay between the two pulses*

The delay between the pulse doublet was controlled by an Analogic 2045 arbitrary waveform generator. The Analogic generator produced a pulse doublet that triggers both the imaging wave, the driving wave, and the oscilloscope. The time recorded on the oscilloscope is genuinely a pulse-echo-time since the oscilloscope is triggered with the same pulse as the imaging wave.

The trigger for the imaging wave and oscilloscope is set to be higher than for the driving wave. Therefore, by setting the Analogic's voltage between these values the driving wave can be triggered alone. The driving wave is triggered by detecting a falling edge, and so the duration of the triggering pulse controls the delay between the driving and imaging waves. The Analogic can therefore be programmed to determine on which pulse the high frequency image should intercept and the delay that occurs between the two waves, and the delay that occurs between the two pulses.

The Analogic is chosen because it has the fastest clock of all the pulsers / pulser delays available. The jitter from the analogic is 5-10ns, which was an order of magnitude better than the other pulsers available.

The time delay and the interval between the doublet on the Analogic generator is controlled remotely via serial connection.

6.6.2.2 Driving wave

The driving wave is generated from an Agilent 33220A waveform generator that is controlled remotely by a LAN connection. It is triggered the trailing edge of the Analogic and produces a sine burst of 10 cycles. The output of the Agilent was amplified by a Tomco power-generator (gain of 50 dB) which then drove the 0.5 MHz TMS transducer used in the preliminary study. The gate to the Tomco was connected to the 'sync out' of the Agilent driving wave generator.

6.6.2.3 Imaging wave

The imaging wave is generated from the custom ordered Panometrics 20 MHz transducer used in the preliminary study. The pulse/receive electronics is controlled with a JSR ULTRASONICS DPR500 dual pulser-receiver with a RPL2 pulser-receiver.

The imaging voltage was 300 V and the combined imaging gain of the pre-amplifier and DPR500 is 50 dB. To help reduce the contribution of the direct transmit / forward scatter of the driving wave, a high pass filter (-3 dB at 7.5 MHz) is used.

The DPR500 may be controlled via a serial connection, with the firing voltage, the gain, and the imaging mode all available options.

6.6.2.4 Summary of arrangement

The full arrangement is given in Figure 6.6. The library to control the equipment was written by the author of this thesis and is available on [github](#)^[96].

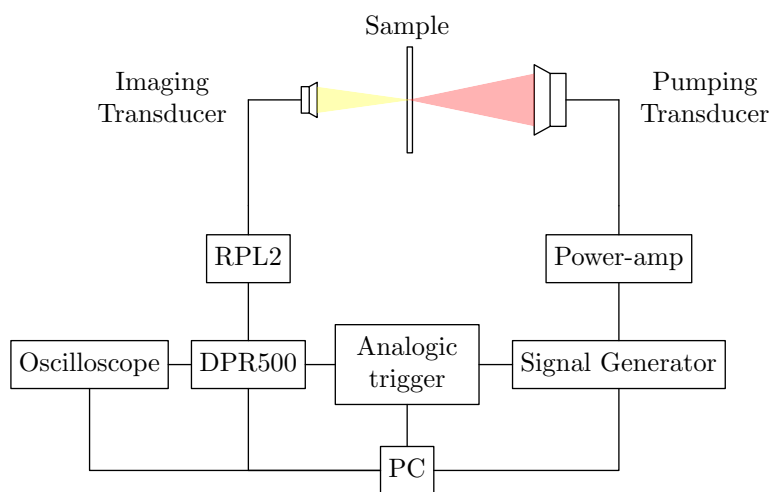


Figure 6.6: The final experimental arrangement

CAVITATION OF WATER

7.1 INTRODUCTION

This chapter presents the results of the experiment designed in chapter 6. The experiment was designed to find the excess pressure received at the imaging transducer. A difference in excess pressure

1. provides strong evidence of high frequency back-scatter from the generated bubbles (rather than just for high-frequency forward scatter generated from the driving wave),
2. enables the location of the scattering bubble (if there is only one) to be determined.

The results for the excess pressure are presented in section 7.2. It is found that the average excess pressure does exhibit a high frequency component indicative of back-scattering the imaging wave. However, the signals are not significantly above the level of noise and so the results are only partially convincing.

Section 7.3 then completes the objectives of chapter 6 by attempting to characterise the bubbles generated. This is done by trying to infer the model's parameters by fitting the acoustic Keller-Miksis equation to the received signal. The assumption is that the signal is generated from a single bubble.

7.1.1 THE BAYESIAN APPROACH

Probability distributions can be used to represent our knowledge of the world. For example, the value of a experimentally obtained variable will in general fluctuate around its average. If different runs of the experiment are independent then the distribution of obtained values fully describes the experiment.

What is learnt from a given experiment is then characterised with how the probability distributions that represent our knowledge change. If a hypothesis, \mathcal{H} , is that a set of experimental data, $\mathbf{x} = \{x_n | n = 1, \dots, N\}$, should conform to a model with a set of parameters, $\mathbf{w} = \{w_i | i = 1, \dots, I\}$, then our full knowledge of the system is given by the joint probability distribution

$$P(\mathbf{x}, \mathbf{w}, \mathcal{H}). \quad (7.1)$$

Of greater importance than 7.1, however, is to determine how our knowledge of the model changes when we collect the experimental data. This can be found from 7.1 by splitting the joint distribution into its conditional probabilities.

$$P(\mathbf{x}, \mathbf{w}, \mathcal{H}) = P(\mathbf{w}|\mathbf{x}, \mathcal{H}) P(\mathbf{x}|\mathcal{H}) = P(\mathbf{x}|\mathbf{w}, \mathcal{H}) P(\mathbf{w}|\mathcal{H}). \quad (7.2)$$

from which it follows that

$$P(\mathbf{w}|\mathbf{x}, \mathcal{H}) = \frac{P(\mathbf{w}|\mathbf{w}, \mathcal{H}) P(\mathbf{w}|\mathcal{H})}{P(\mathbf{x}|\mathcal{H})}. \quad (7.3)$$

Equation 7.3 is Bayes Theorem. It states that the probability of the model's parameters, *given the data*, can be determined from the probability of the data when the parameters are known, and the a probability of parameters *before the data was known*. It describes exactly the process of inference.

The term $P(\mathbf{x}|\mathbf{w}, \mathcal{H})$ is the likelihood function. It evaluates the degree to which the model with a given set of parameters agrees with the experimental data. If it is assumed that every data point is independent, and that each datum should agree with

the prediction of the model, t_n , to within Gaussian noise then the likelihood function would be,

$$P(\mathbf{x}|\mathbf{w}, \mathcal{H}) = \prod_{n=1}^N \sqrt{\frac{\gamma}{2\pi}} e^{-0.5\gamma(x_n - t_n)^2}. \quad (7.4)$$

The variable γ is the precision - the inverse of the variance - and is one of the set $\{w_i\}$.

The term $P(\mathbf{w}|\mathcal{H})$ in 7.3 is independent of the experimental data $\{x_n\}$. It represents our knowledge of the parameters before the experiment was carried out. It could be that the parameters are already known to great precision - in which case the probability distribution would tend towards a delta function. Alternatively, it could be that the a priori knowledge of the precision, say, does not extend beyond the requirement that the precision is positive definite. In this case the prior distribution would be represented by a scale invariant positive definite distribution. One such example is the Gamma distribution,

$$P(\gamma|s, c) = \frac{1}{\Gamma(s)c} \left(\frac{x}{s}\right)^{c-1} \exp\left(-\frac{x}{s}\right), \quad (7.5)$$

in the limit such that $sc = 1$ and $c \rightarrow 0$ ^[68].

The hypothesis, \mathcal{H} , encompasses all of the assumptions that go into the inference. These include the choice of the model that is fitted to the data, the prior probabilities assigned to the model variables and the noise model described by the likelihood function. These assumptions are inevitable - they reflect the uncertainty that prompts the experiment in the first place. However, since many different hypotheses can be dreamt up, it is important to be able to evaluate how each is supported by the experimental data. For this, Bayes Theorem can be applied a second time: the probability of the hypothesis, given the data, is

$$P(\mathcal{H}|\mathbf{x}) = \frac{P(\mathbf{x}|H) P(\mathcal{H})}{P(\mathbf{x})}. \quad (7.6)$$

Since the probability of the data, $P(\mathbf{x})$, is independent of the hypothesis it can be elim-

inated when comparing two hypotheses, \mathcal{H}_1 and \mathcal{H}_2 ,

$$\frac{P(\mathcal{H}_1|\mathbf{x})}{P(\mathcal{H}_2|\mathbf{x})} = \frac{P(\mathbf{x}|\mathcal{H}_1)}{P(\mathbf{x}|\mathcal{H}_2)} \frac{P(\mathcal{H}_1)}{P(\mathcal{H}_2)}. \quad (7.7)$$

The second of the ratios on the right-hand-side of 7.7 give an opportunity, if desired, to prefer one model over another irrespectively of any data collected. The first quotient is determined from the experimental data. The term $P(\mathbf{x}|\mathcal{H})$ is called the evidence and it is the partition function of 7.6.

A model that is highly constrained will be inflexible in the range of predictions it can make, whereas a model that has many free parameters will be able to predict a vast number of possible outcomes. The more constrained model will therefore have a smaller set of likely outcomes, but each of these will have a much greater probability than the many possible outcomes of the less constrained model. The right-hand-side of 7.7 therefore directly and quantitatively embodies Occan's razor, the rule of thumb that states that 'simpler' models should be favoured over more complicated models. For a more detailed discussion of model comparison and Occan's razor see^[68].

To evaluate the evidence the numerator in equation 7.3 must be integrated over the entire parameter space,

$$P(\mathbf{x}|\mathcal{H}) = \int_{\mathbf{w}} d\mathbf{w} P(\mathbf{w}|\mathbf{w}, \mathcal{H}) P(\mathbf{w}|\mathcal{H}) \quad (7.8)$$

In general this cannot be done analytically. However, it is often the case that the probability density tightly peaked about the maximum. In this case the evidence may be evaluated by approximating the peak with a Gaussian, which can be integrated. This is the saddle point approximation. Expanding the logarithm of the unnormalised probability distribution, P^* , around the maximum, \mathbf{x}_0 , gives

$$\ln P^* = \ln P^*(\mathbf{x}_0) - \frac{1}{2} (\mathbf{x} - \mathbf{x}_0)^T \mathbf{A} (\mathbf{x} - \mathbf{x}_0) \quad (7.9)$$

where

$$\mathbf{A} = A_{ij} = \frac{\partial^2}{\partial x_i \partial x_j} \ln P^*(\mathbf{x}_0) \quad (7.10)$$

is the Hessian matrix. The right-hand-side of equation 7.3 is therefore approximated by the multidimensional Gaussian

$$P(\mathbf{w}|\mathbf{x}, \mathcal{H}) = P^*(\mathbf{x}_0) \exp\left(-\frac{1}{2} (\mathbf{x} - \mathbf{x}_0)^T \mathbf{A} (\mathbf{x} - \mathbf{x}_0)\right) \quad (7.11)$$

for which the normalisation constant, the evidence, is

$$P^*(\mathbf{x}_0) \sqrt{\frac{(2\pi)^K}{\det \mathbf{A}}} \quad (7.12)$$

7.2 THE EXCESS PRESSURE

To find the excess pressure requires the bubbles to be excited twice in quick succession by the driving wave. For one of driving doublets the imaging wave is in receive-only mode. This then records the contribution of the directly transmitted signal and of forward scatter. The imaging transducer is in pulse echo mode for the other signal of the doublet, with the high frequency pulse coincident both spatially and temporally with its respective driving wave. This pulse then records the directly transmitted driving wave, forward scatter, and the high frequency back scatter. By subtracting the signals of the doublet, only the contribution from the back scatter should remain.

For the method to work the sample population of bubbles must be imaged for both driving waves, so that the forward scatter is the same each time. To test this assumption the driving doublets were first both imaged in receive only mode. The resultant signals in this control study should be identical.

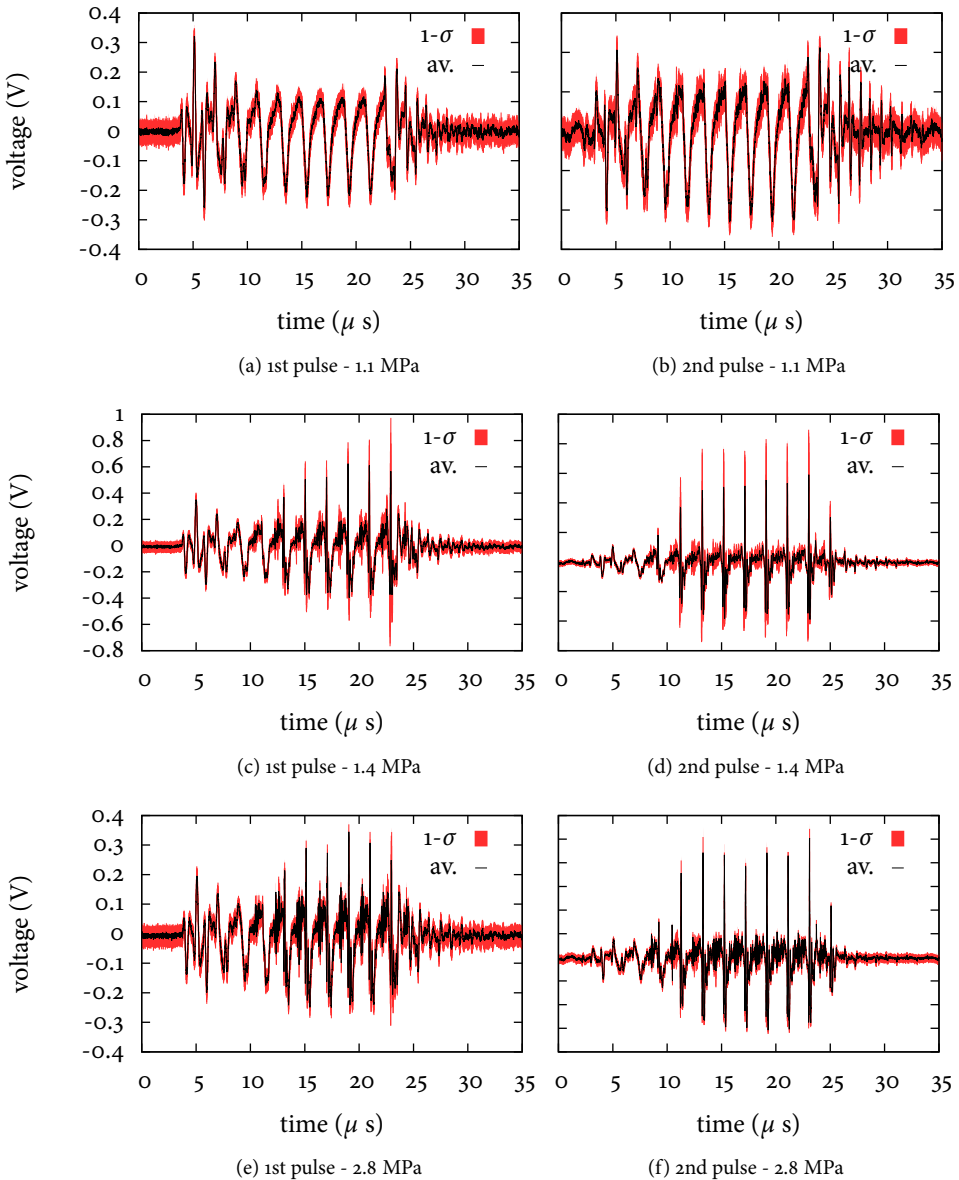


Figure 7.1: The pressure received by the imaging transducer when the driving wave is on but the imaging wave is off (receive-only). The second pulse (d) is received 100 μ s after the first (c). Each image is the average of 49 images, the first standard-deviation error bars are indicated. Three different pressures are shown below each sub-figure.

7.2.1 CONTROL STUDY: RECEIVE ONLY IMAGING

Figure 7.1 plots control data for three different pressures. On the left hand side (images (a), (c) and (e)) shows the forward transmit received from the first pulse. The right

hand side (images (b), (d) and (f)) shows the forward transmit from the second pulse, which occurred 100 μ s after the first.

There are a number of important things to notice in Figure 7.1:

1. At the higher pressures (Figure 7.1c-(f)) a strong and narrow response is observed over and above the more sinusoidal response found at the lower pressures of Figure 7.1a and (b). Qualitatively Figure 7.1c-(f) bear a strong resemblance to the simulated bubble pulsations of chapter 5. The pressure dependence of these signals provide strong evidence for the generation of bubbles by the driving wave.
2. The received pressure for the first and second pulse are not the same. In general the forward transmit from the second pulse is stronger than from the first. This further supports the interpretation of the strong peaks in Figure 7.1c-(f) as forward scatter from the driving wave. This is because the difference between the two pulses suggests a temporal lifespan of the generated bubbles of greater than the 100 μ s relaxation time.
3. The noise in each image is fairly low. While the first and second pulse at each pressure are different, for each repetition of the experiment the pulses are fairly consistence. The indicates that after the second pulse the bubble population relaxes back to its original state before the first pulse of the next test. The passage of an acoustic wave does not seem to fundamentally alter the sample.

The difference in scatter between the first and second pulse represents both a problem and an opportunity. It is a problem because the excess pressure method requires the response of both driving wave to be the same. It is, after all, to be subtracted away.

It is an opportunity because it gives a means of sizing the generated bubbles. Varying the interval between the pulses until they become stable provides an upper bound on the lifetime (and therefore radius) for the generated bubbles.

In Figure 7.2 the interval between the pulses is examined for the pressure of 1.4 MPa. This pressure is chosen because it is one of the more moderate pressures for which

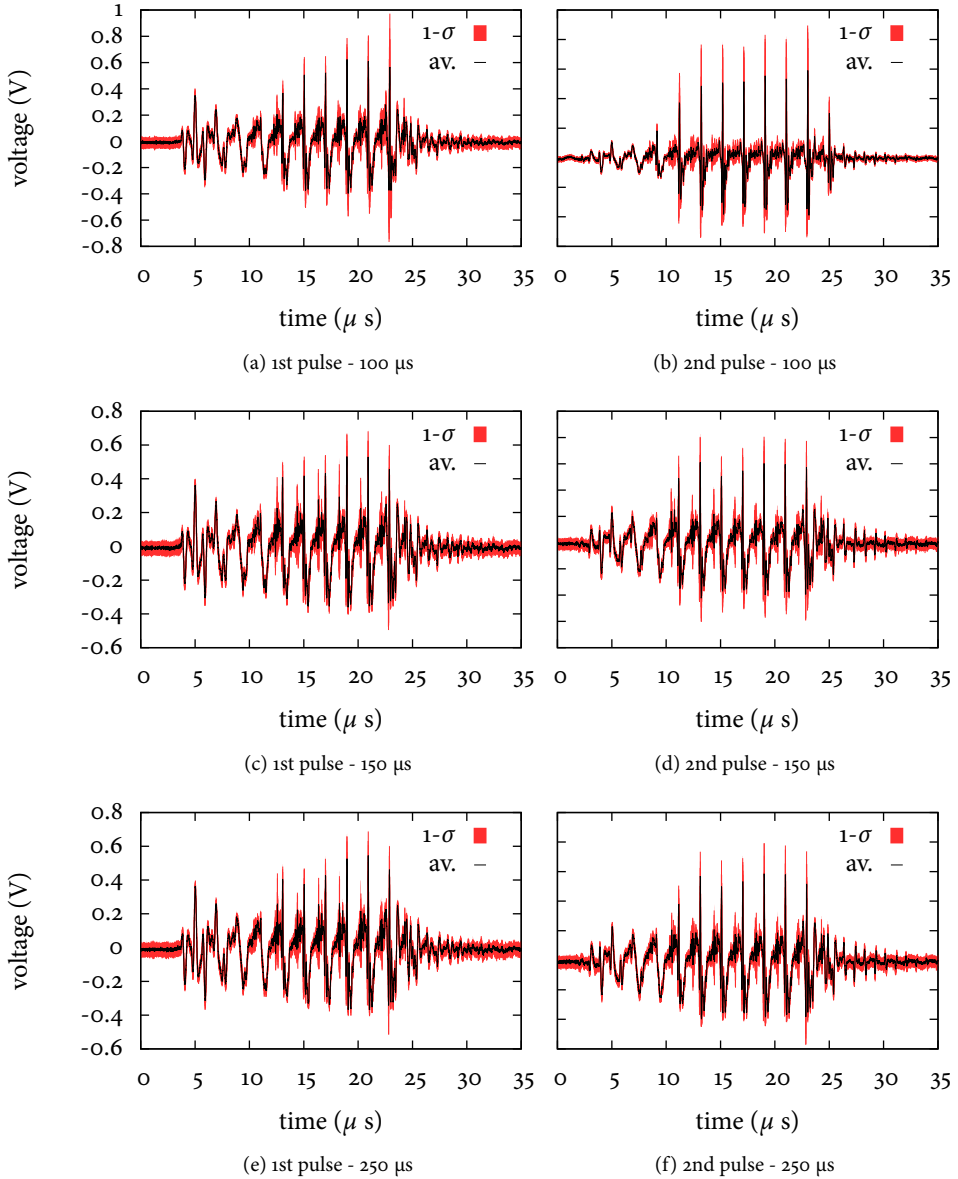


Figure 7.2: The pressure received by the imaging transducer when the driving wave is on but the imaging wave is off (receive-only). Each image is the average of 49 images, the first standard-deviation error bars are indicated. The time interval for each pair of images is indicated. The driving pressure is 1.4 MPa in all cases.

Figure 7.1c-(d) demonstrates significant bubble interaction.

The forward scattering for when the time lag between driving pulses is between 100 μ s and 250 μ s (Figure 7.2a-(f)) are similar. In all cases the interaction with the second pulse is stronger than the first, but when each of the respective second pulses are com-

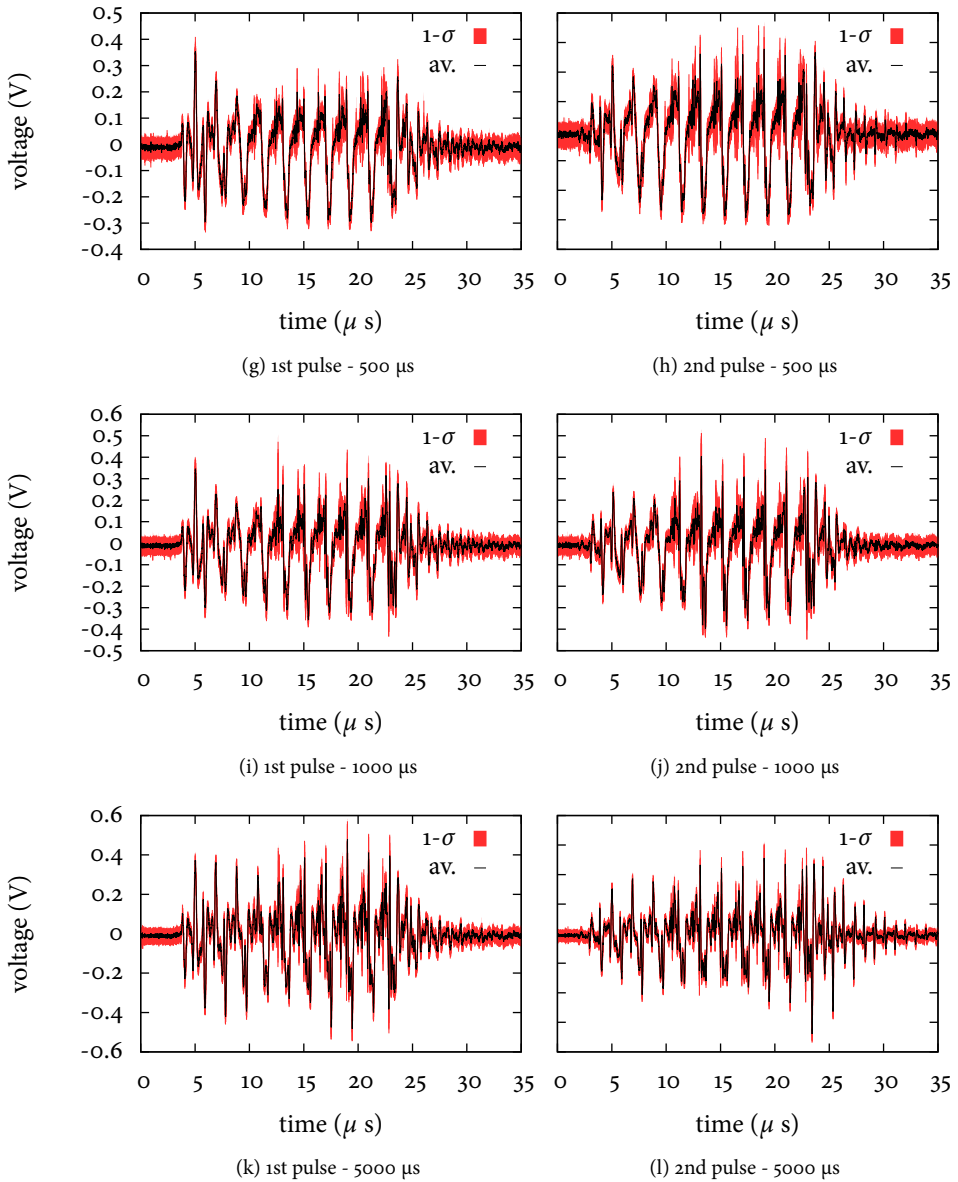


Figure 7.2: (continued) The pressure received by the imaging transducer when the driving wave is on but the imaging wave is off (receive-only). Each image is the average of 49 images, the first standard-deviation error bars are indicated. The time interval for each pair of images is indicated. The driving pressure is 1.4 MPa in all cases.

pared no temporal effects are obvious. The temporal durations of 150 μ s and 250 μ s look particularly similar.

For the larger durations of Figure 7.2g-(l) a much depleted interaction is found for both the first and second pulse. While dissolution of a generated bubble would account for

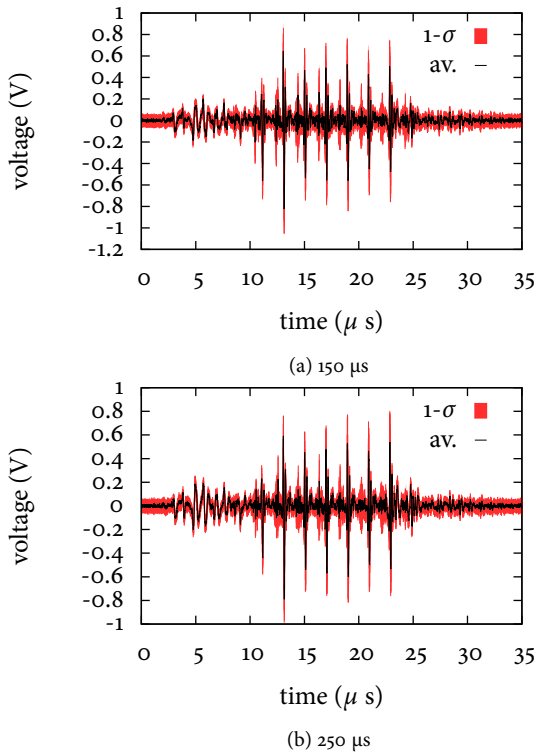


Figure 7.3: The difference image for the pressure received by the imaging transducer when the driving wave is on but the imaging wave is off (receive-only).

a reduced interaction in the second pulse, the interaction with the first pulse should be the same in all cases. Figure 7.2g-(l) is therefore most likely to result from a gradual change in the fundamental bubble population of the sample.

For each temporal offset three experiments are carried out. First the control where the imaging transducer is in receive mode only. Secondly when the imaging transducer coincides with the first driving pulse at the focus, and then finally when the imaging transducer is timed to coincide with the second driving pulse. Each of these experiments are repeated 50 times, meaning that the driving pulse fires 300 times for every temporal offset. It seems that the bubble population remains fairly constant over the first thousand or so driving pulses, but loses bubbles by the time the longer pulsations are investigated.

For the excess pressure to be evaluated the receive only scatter from the two pulses needs be the same. The time lags of 150 μ s and 250 μ s between driving pulses look from

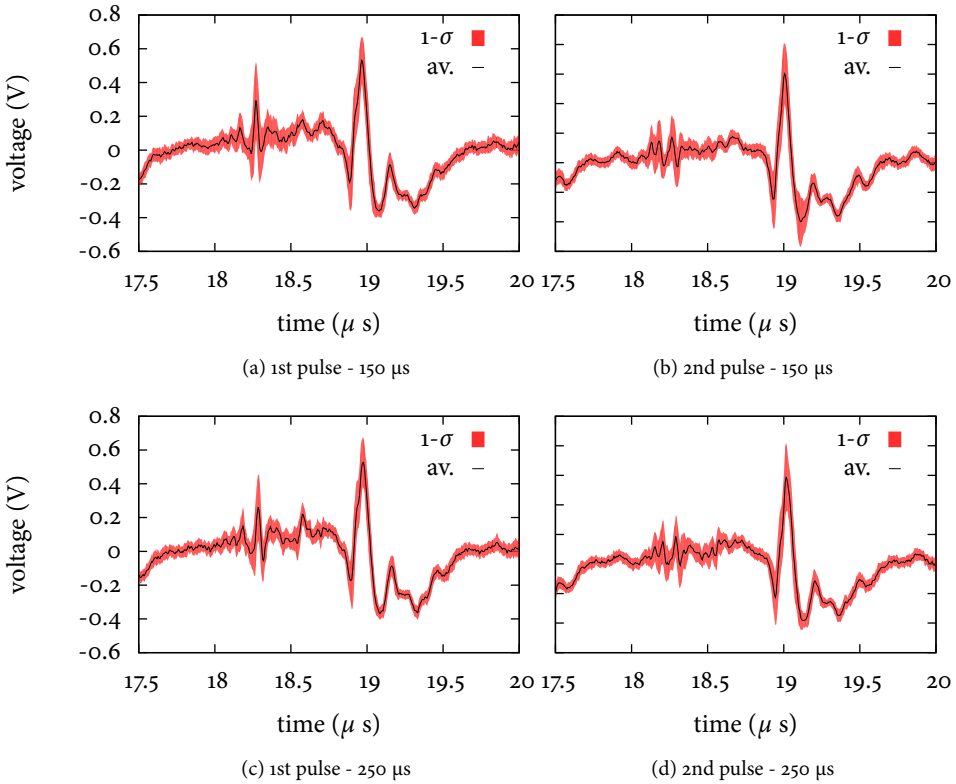


Figure 7.4: The receive only plots of Figure 7.2 in greater detail.

Figure 7.2 to be the most promising in this regard. The difference image - evaluated by subtracting the second received pulse image from the first - is plotted in Figure 7.3.

The results are somewhat disappointing. The two driving pulses do not cancel as hoped. Rather, the strong scatter from the bubble has been accentuated. To understand why, Figure 7.2 is plotted in greater detail in Figure 7.4. It is seen in Figure 7.4 that the second pulse, although similar in shape to the first, is shifted in phase by a small fraction of a microsecond. The phase shift makes it possible to estimate the change in the bubble environment between adjacent pulses, but we do not pursue this here. Instead, we will modify our approach to excess imaging slightly. Rather than subtracting the second pulse from the first, where the bubble populations are demonstrably different, we will group the experimental results from the first pulse and the second pulse separately. That is, the receive only image for the first driving pulse will be compared to the pulse-echo image of the first driving pulse. Likewise, the receive-only image for the second

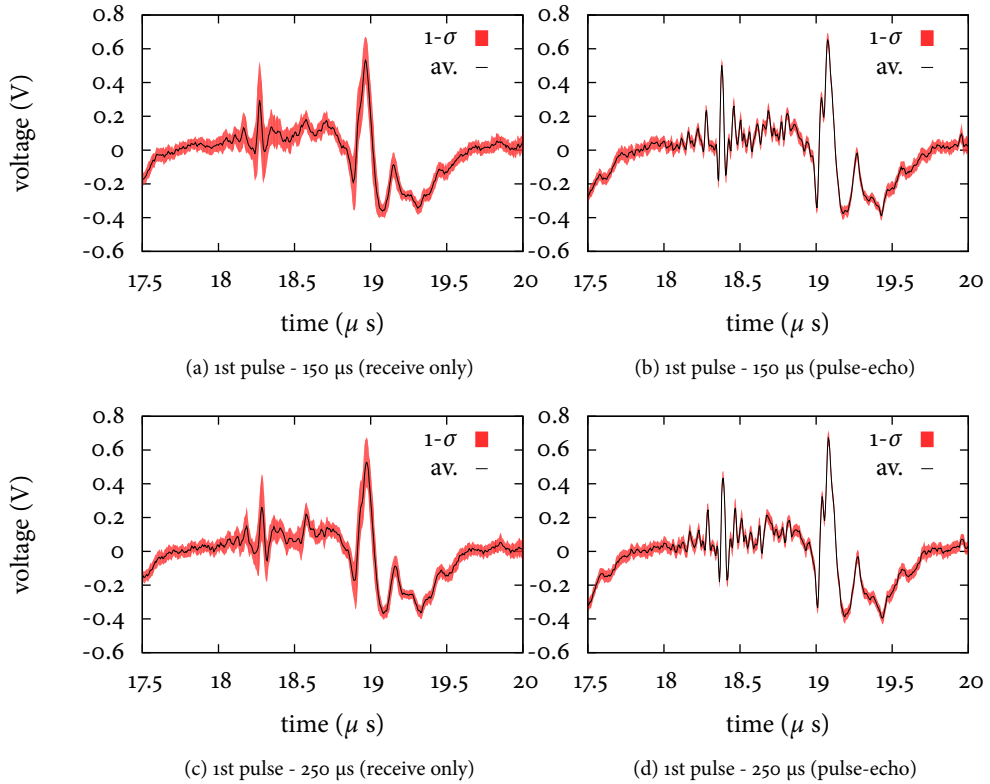


Figure 7.5: Comparison of the receive only signal from the first pulse of the control experiment, with the pulse-echo signal of the first pulse. All signals are averaged over 49 repetitions, and are taken for the pressure 1.4 MPa. The delay between the two pulses is shown.

pulse will be compared with the pulse echo image that samples that second pulse.

7.2.2 PULSE-ECHO IMAGING OF THE FIRST DRIVING PULSE

Figure 7.5 compares the first pulse from the control experiment (Figure 7.4) with the signal from when both the driving and imaging waves are on. The signals for a delay of 150 μ s and 250 μ s are shown. The two pulses are very similar. The most notable differences are:

1. the doublet in the principle pulse at approximately 19.2 μ s,
2. the phase of the two signals. There is again a phase shift with the pulse-echo image occurring slightly later than the receive only trace. Unlike Figure 7.4, how-

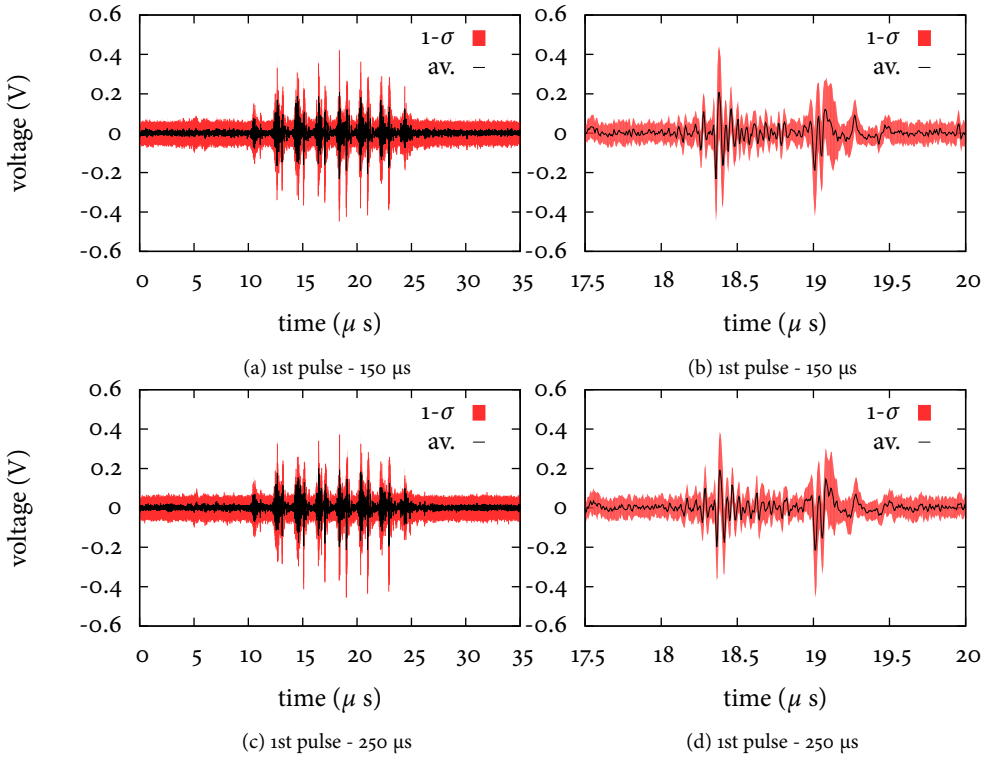


Figure 7.6: The excess pressure evaluated for the first pulse. The pressure received when only the driving wave has been on has been subtracted from the pressure received when both the imaging and driving transducers were transmitting. The phase difference between the two images has been removed in a processing step by cross-correlation.

ever, the rest of the image, including the feature at approximately 18.3 μ s is very similar between the two pulses.

3. the signal to noise ratio of the pulse-echo image. The reason for an improved signal to noise ratio in pulse-receive mode over receive only mode in the DPR500 is not clear. However, it seems to be a feature across experiments.

To account for the change in phase between the pulse-echo and receive only images, a lag is added to the receive only image in a processing step so that the images overlap as best they can. This is achieved by means of maximising the cross-correlation between the traces. The results are shown in Figure 7.6. For both time lags the results are very similar. It is seen that the transmit features of the image (such as those around 5 μ s) have been successfully removed, leaving a high frequency signal on top of a flat baseline.

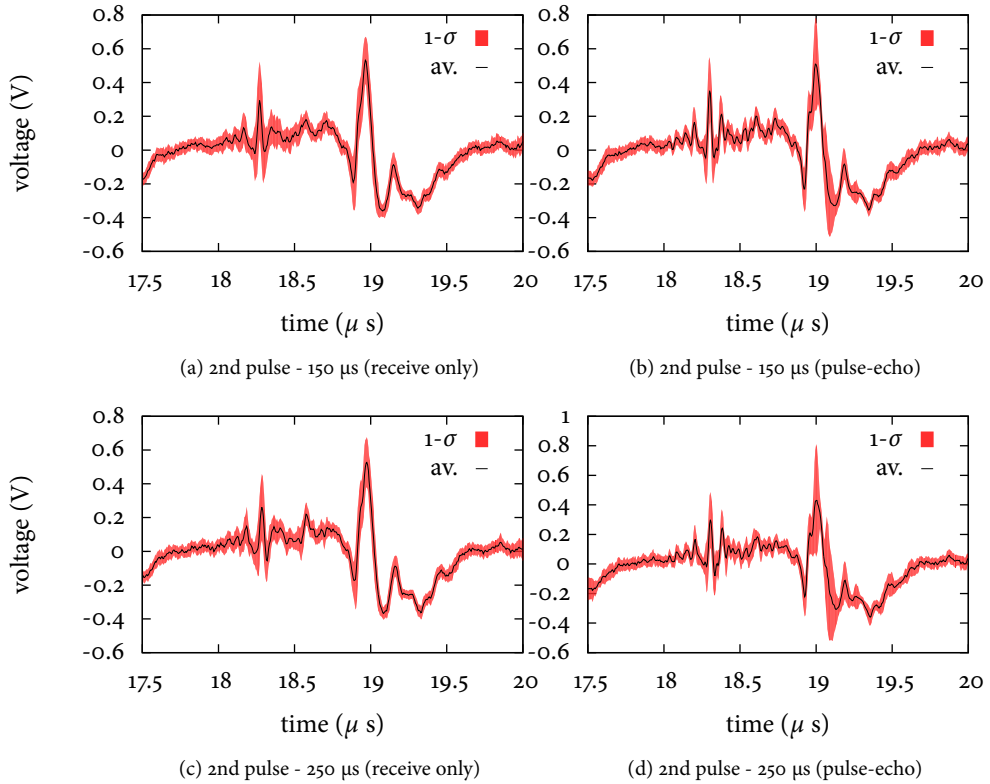


Figure 7.7: Comparison of the receive only signal from the second pulse of the control experiment, with the pulse-echo signal of the second pulse. All signals are averaged over 49 repetitions, and are taken for the pressure 1.4 MPa. The delay between the two pulses is shown.

7.2.3 PULSE-ECHO IMAGING OF THE SECOND DRIVING PULSE

To check results of Figure 7.6 we repeat the analysis for when the imaging wave is coincident with the second driving wave. The results should be qualitatively similar, although there could be differences in detail due to the different bubble environments that exist between the first and second pulse (as is reflected in Figure 7.2).

The detail of the pulse echo image for the second pulse is drawn in Figure 7.7. The subtraction image (again with the phase difference removed by a cross correlation processing step) is shown in Figure 7.8.

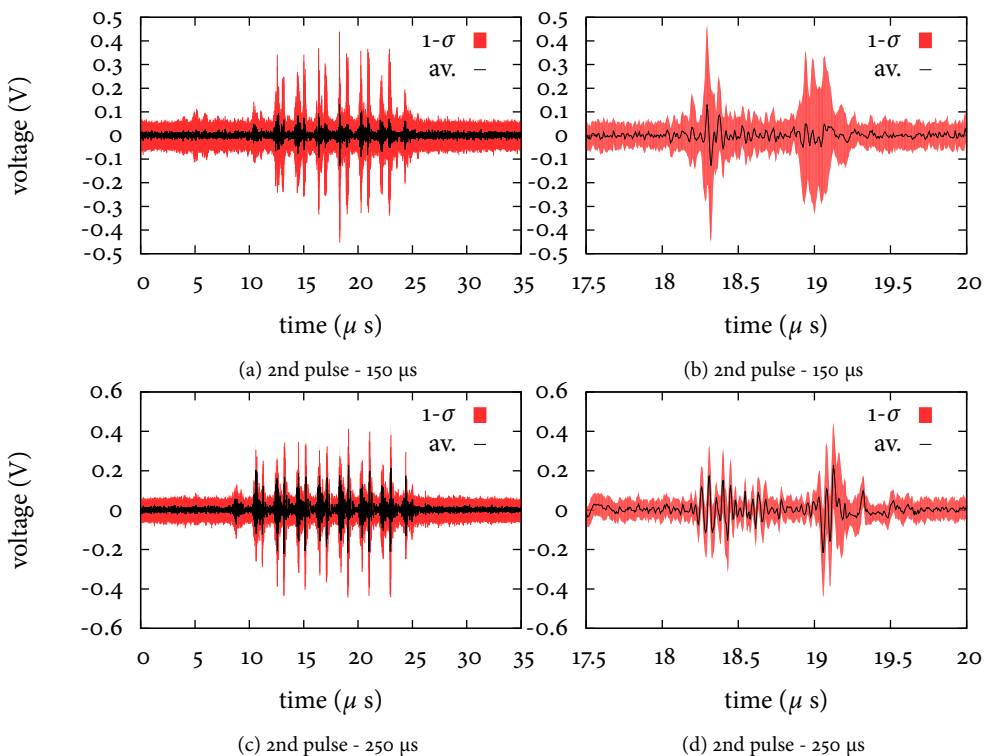
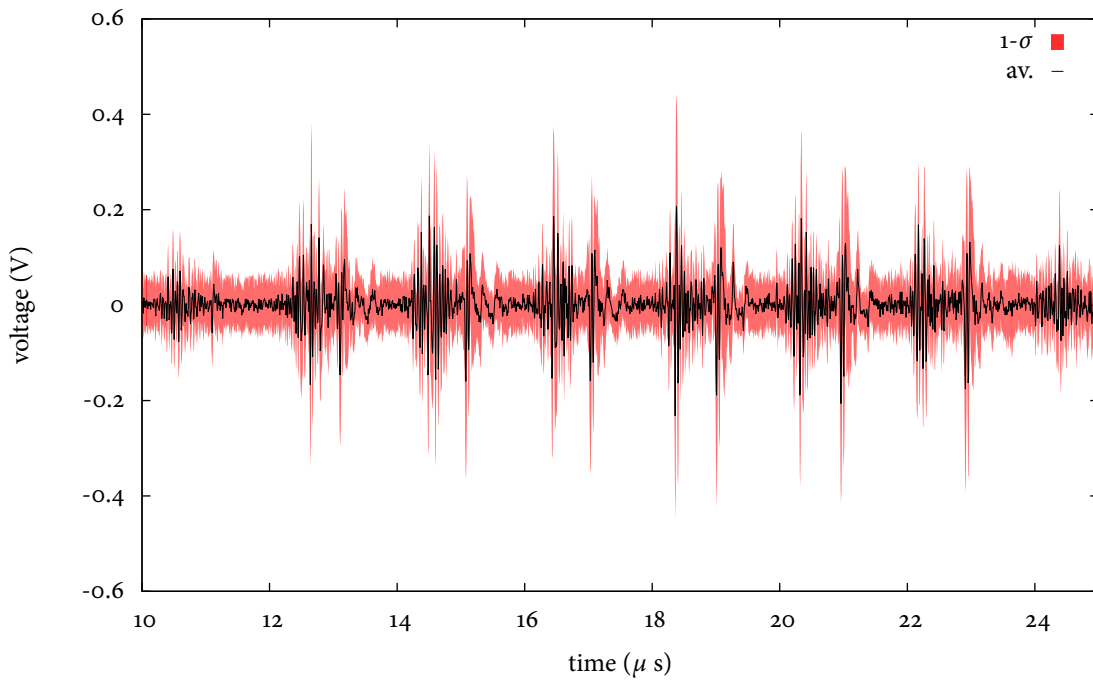


Figure 7.8: The excess pressure evaluated for the first pulse. The pressure received when only the driving wave has been on has been subtracted from the pressure received when both the imaging and driving transducers were transmitting. The phase difference between the two images has been removed in a processing step by cross-correlation.

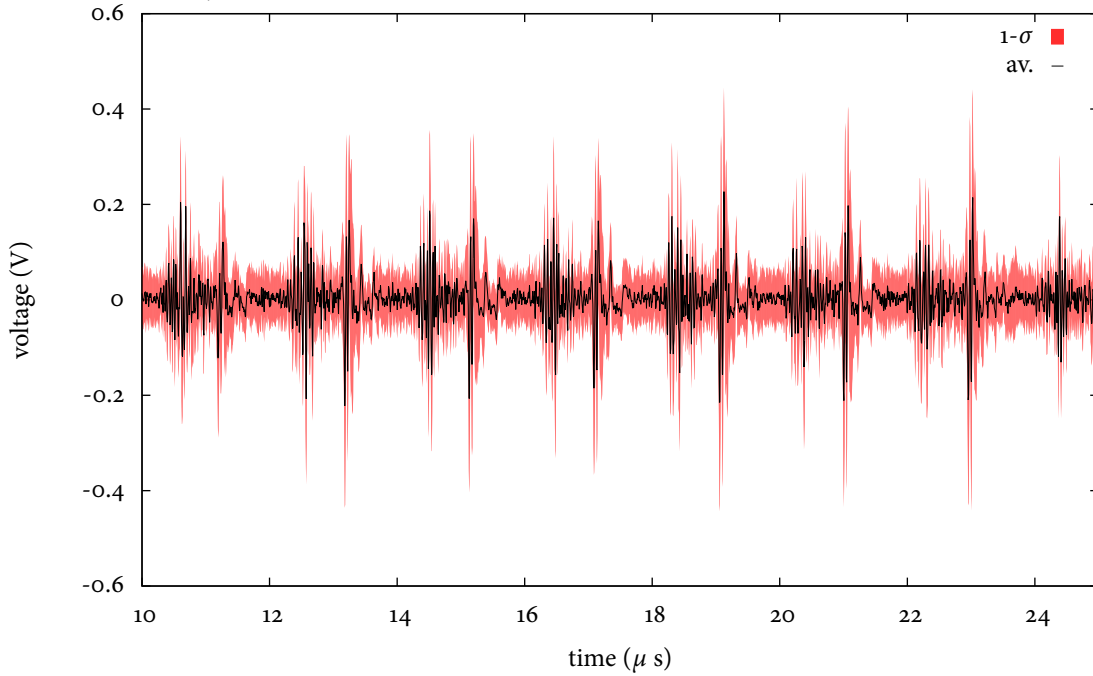
7.2.4 DISCUSSION

Both Figure 7.6 and Figure 7.8 indicate the presence of a high frequency excess pressure.

To compare these more closely, they are re-plotted adjacent to each other in Figure 7.9.



(a) The first pulse when the imaging transducer is on, subtracted from the first pulse when the imaging wave is not on - 150 μ s



(b) The second pulse when the imaging transducer is on, subtracted from the second pulse when the imaging pulse wave is not on - 250 μ s

Figure 7.9: An expanded view of Figure 7.9 showing the excess pressure for direct comparison.

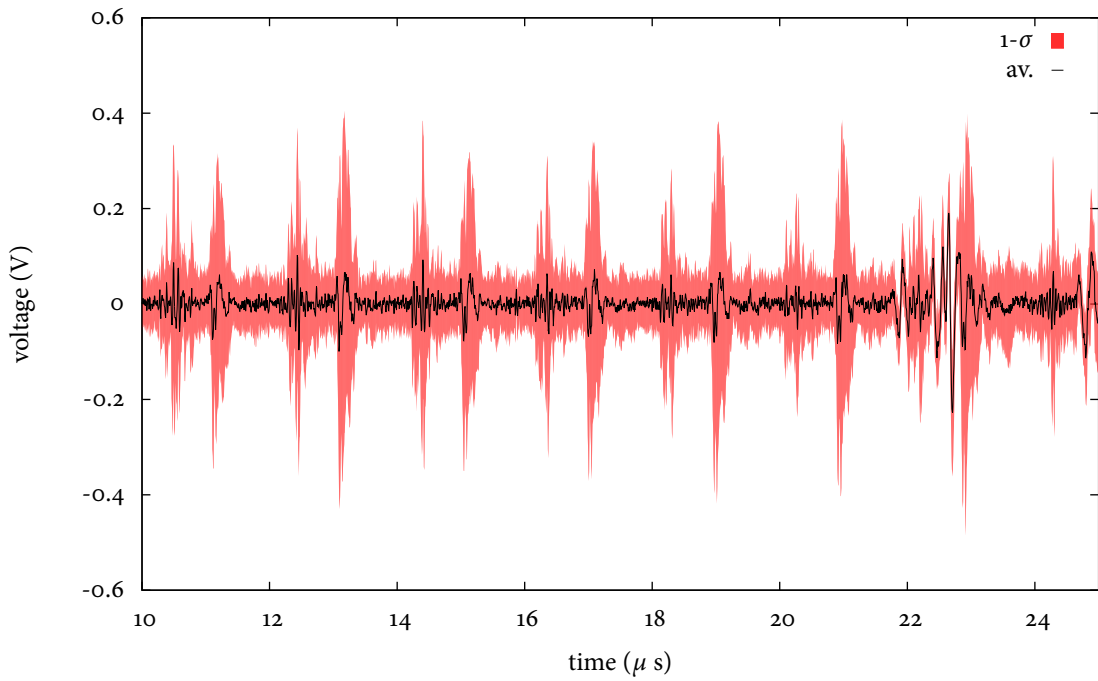
As a control, we also plot in Figure 7.10 what should be the null result. In Figure 7.10 the excess pressure from the respective receive only pulses are evaluated. Since the imaging wave is not fired, the signals should cancel.

By comparing Figure 7.9 and Figure 7.10 it is seen that

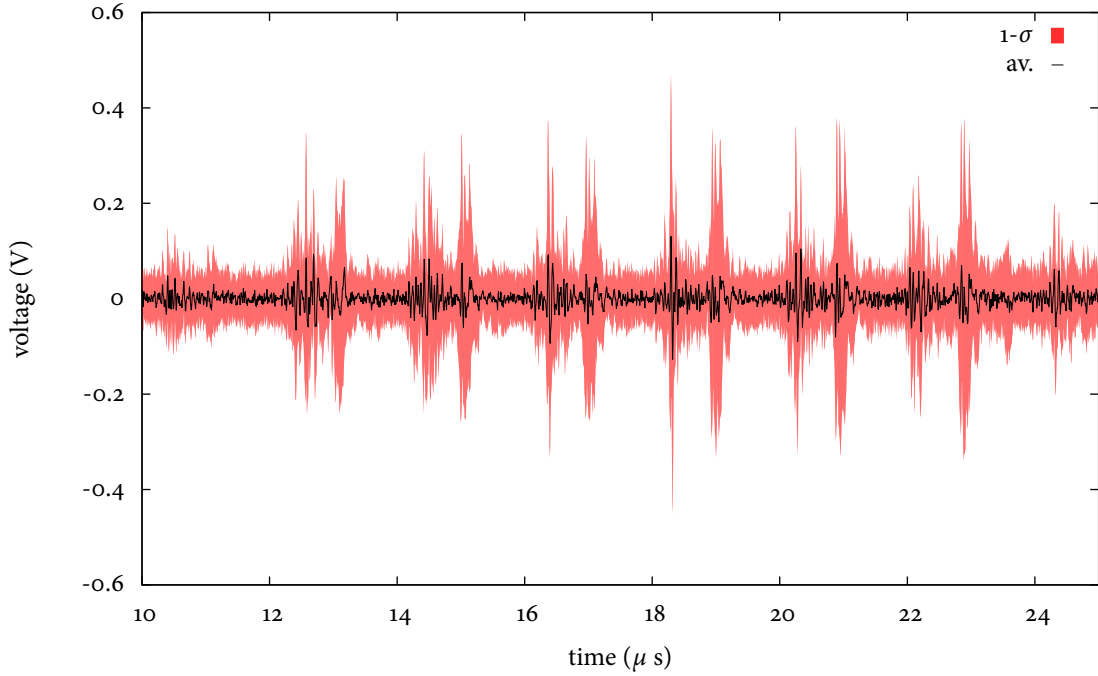
1. The excess pressure plots do exhibit a greater signal strength than the null plots.
2. In excess pressure is not greatly above the level of noise. This means that the signal features in the null plots are (while lower) not dissimilar to the plots from the excess pressure.

The results are therefore suggestive, but are not conclusive.

The reason for the phase shift in the second pulse has not been entirely determined by the experiment. It is likely that the bubble's state has altered in some way from the first pulse to the second. There are a number of mechanisms by which this will occur, and lacking experimental evidence to support one over another, we resist the temptation to speculate.



(a) The second pulse when the imaging transducer is off, subtracted from the first pulse when the imaging wave is not on - 150 μ s



(b) The second pulse when the imaging transducer is off, subtracted from the first pulse when the imaging wave is not on - 150 μ s

Figure 7.10: The excess pressure evaluated when the imaging wave is not on. The two images should subtract to zero. The phase difference between the two images has been removed in a processing step by cross-correlation.

7.3 INFERRING THE BUBBLE SIZE

In this section we attempt to characterise the bubbles by fitting their acoustic response to the acoustic-Keller-Miksis model of chapter 5.

A simple (if slightly optimistic) model for the pulsations of the bubble is constructed by assuming

1. the pressure wave emanates from a bubble (or set of mono-disperse bubbles). A free parameter in the model is therefore the equilibrium bubble radius.
2. the pressure wave is $\frac{1}{2}$ MHz sinusoid of 13 cycles that is truncated by a cosine function. The free parameters are then the peak amplitude, the fraction of the wave truncated by the sinusoid, and the offset of the sinusoid in time.
3. The noise is Gaussian white noise with a standard deviation that is modelled.
4. The voltage generated by the transducer is equal to the far-field pressure to within a (modelled) multiplicative factor. (I.e. we are assuming infinite bandwidth of the transducer and receive electronics).

The likelihood that we maximise is that

$$P(\mathbf{x}|\mathbf{w}, \mathcal{H}) = \prod_{t=0}^T \mathcal{G}(x_t; \mu_t, \gamma) \quad (7.13)$$

where

$$\mathcal{G}(x; \mu, \gamma) = \sqrt{\frac{\gamma}{2\pi}} e^{-0.5\gamma(x-\mu)^2} \quad (7.14)$$

is a Gaussian distribution of mean μ and precision γ . Each data point recorded is denoted x_t and the modelled point (given the parameters) the mean μ_t . The bubble radius, noise precision, pressure and offset and truncation ratio are all positive quantities which we model with Gamma distributions. However, to enforce positivity during the iterative numerical updates we re-parametrise the gamma distribution of equation 7.5

such that $l = \ln(x)$. It follows that

$$P(l) = P(x(l)) \left| \frac{\partial x}{\partial l} \right| = \frac{1}{\Gamma(c)} \left(\frac{x(l)}{s} \right)^c \exp(-x(l)/s). \quad (7.15)$$

For the time being we assume that the priors are non-informative, such that $sc = 1$ and $c \rightarrow 0$, from which it follows that 7.15 is flat. To find the most likely parameters of the model, equation 7.3 tells us that in this case we must maximise the likelihood.

Since the model is non-linear, maximising the likelihood with a gradient approach is impossible. Therefore, to maximise 7.13 we use the simplex minimisation of Nelder and Mead^[75] to minimise the negative of the log likelihood. The implementation that is used is that of the Gnu Scientific Library.

The simplex approach of Nelder and Mead^[75] starts from an initial position \mathbf{x}_i and constructs a further N points from a initial step-size in each dimension that is provided on initialisation. At each iteration a new simplex is constructed that is closer to a minimum.

One slight complication with the simplex approach is in approximating the Hessian matrix that is required for model comparison. Since (and quite deliberately) this minimisation method does not rely on derivatives, no Hessian matrix can be directly evaluated. An approach for doing this was provided in Nelder and Mead's original article^[75].

7.3.0.1 Results

We test the model on a single trace obtained at a pressure of 1.4 MPa. Three runs of the minimisation were taken. The initial position and the found minima are displayed in Table 7.1 and Table 7.2 respectively, and the predicted bubble oscillations are drawn in Figure 7.11

Qualitatively, the fits displayed in Figure 7.11 are convincing. The fits displayed in Figure 7.11 have converged to very similar plots. This can be seen by visual inspection, but also by examining the log likelihood per data point that is displayed in Figure 7.12a. The model captures the main features of the experimental data and has correctly mod-

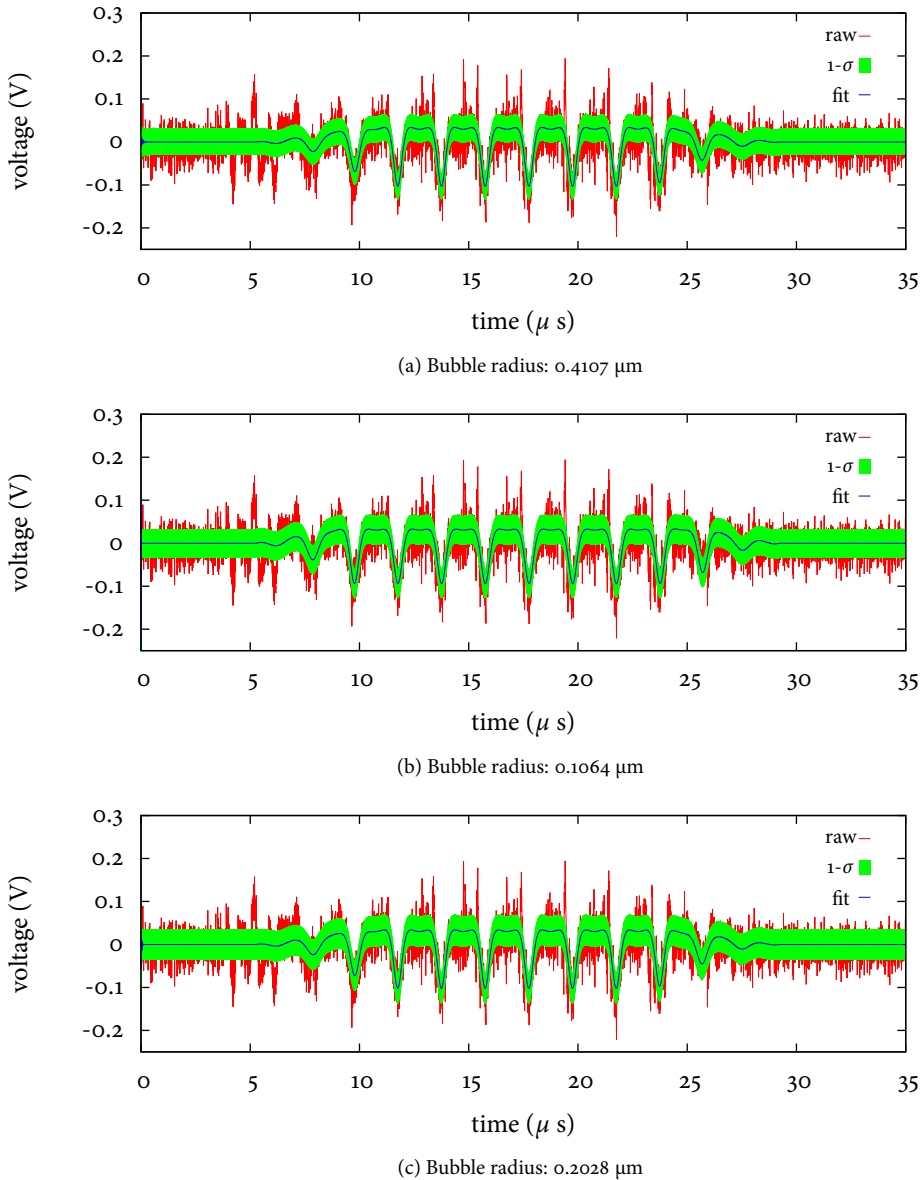


Figure 7.11: Fits of single traces to a bubble model of the given initial radius. The trace was taken at a pressure of 1.4 MPa and at an interval of 150 μ s.

elled the noise so that approximately two thirds of data points are within one-standard-deviation of the fit. However, the actual fitted parameters in each plot are very different. This can be seen by comparing the equilibrium bubble radii. This suggests that the likelihood is not a sharply peaked distribution, and that it might even be multimodal. This would imply that the estimates for the evidence given in Table 7.2 are unreliable.

Table 7.1: Initial parameters for Figure 7.11a

Parameter	Initial 1	Initial 2	Initial 3
scale factor	3000	3000	3000
standard-deviation	0.03 V	0.03 V	0.03 V
bubble radius	0.5 μm	1.3 μm	0.2 μm
pulse amplitude	0.1 MPa	0.1 MPa	0.1 MPa
pulse offset	29.2 μs	29.2 μs	29.2 μs
pulse tempered ratio	0.5	0.5	0.5

Table 7.2: Fitted parameters for Figure 7.11a

Parameter	Fitted 1	Fitted 2	Fitted 3
scale factor	345.7	5729	1472
standard-deviation	0.03034 V	0.03371 V	0.03561 V
bubble radius	0.4107 μm	0.1064 μm	0.2028 μm
pulse amplitude	0.1290 MPa	0.3448 MPa	0.2185 MPa
pulse offset	29.25 μs	29.24 μs	29.25 μs
pulse tempered ratio	0.53	0.40595	0.5189
log (evidence)	-18908.29097	-19128.52276	-19209.08907

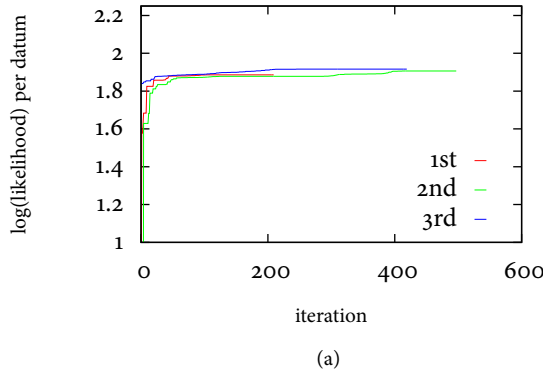
7.3.1 USING AVERAGES

The noise in the first model was too great, which meant that the fits were too permissive.

A large range of models could produce the same results.

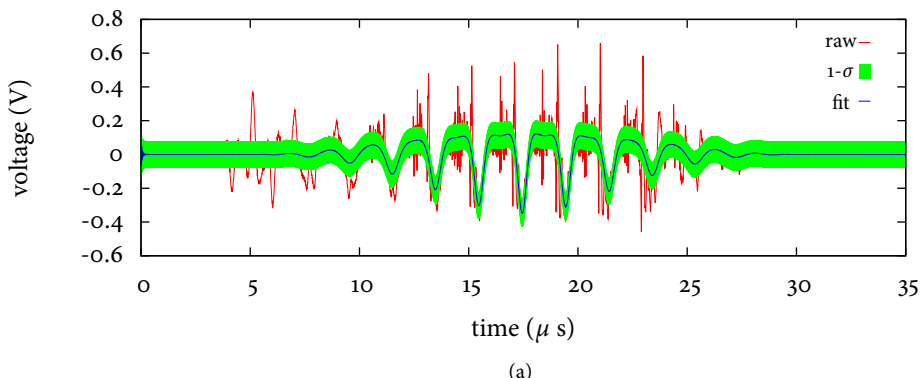
To improve the test of the modelling we repeat the same model but this time with the average of 49 A-lines. (so that the noise should be reduced by a factor of 7).

The results of the model when fit to the average is displayed in Table 7.3 and is drawn in Figure 7.13a. The inferred model is similar to that given previously, but in this case, due the reduced noise of the experimental data the fitted model is not convincing. The model does not capture the high frequency detail in the bubble's oscillation, and this



(a)

Figure 7.12: The log likelihood per data point for each of the three models of Figure 7.11



(a)

Figure 7.13: Fits of the average trace. The trace was taken at a pressure of 1.4 MPa and at an interval of 150 μs

forces the modelled noise to be much greater than it should be. The reduction in the quality of the fit is indicated by the poor evidence evaluation.

Additionally, Figure 7.14b still indicates a problem with metastable states and converging to differing bubble radii, even when the likelihood is similar, as is seen in Figure 7.14a.

7.3.2 IMPROVING THE MODEL

There are a number of improvements that can be made to the model.

First we try to improve the model of the driving wave. This can be done by increasing the number of subcomponents of the driving wave, so that we have a set of n superposing waves, each with their own amplitude and offset, with the frequencies taken as

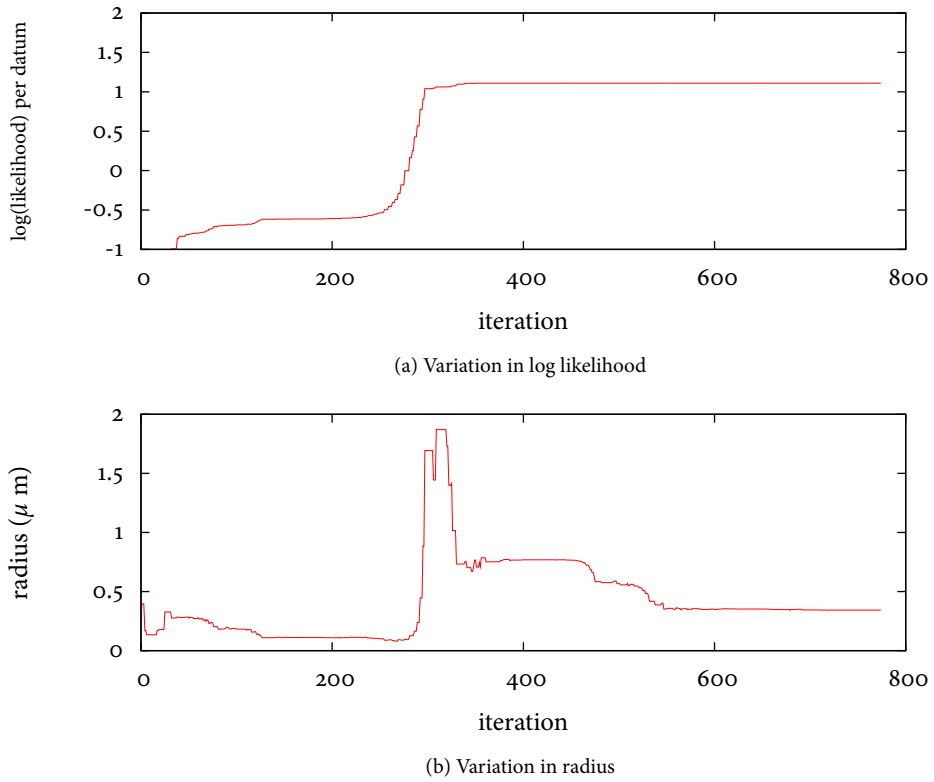
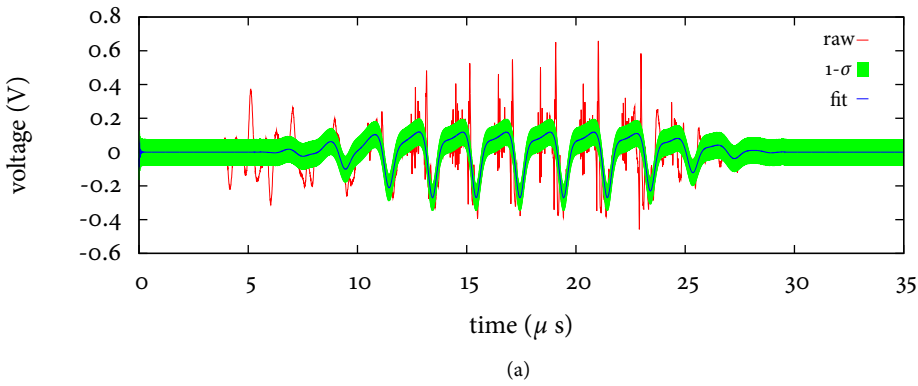


Figure 7.14: Variation in parameters with iteration number for the fit of Figure 7.13a

Table 7.3: Parameters for Figure 7.11a

Parameter	Initial 1	Fitted 1
scale factor	3000	1980
standard-deviation	0.03 V	0.07973 V
bubble radius	0.5 μm	0.3426 μm
pulse amplitude	0.1 MPa	0.1357 MPa
pulse offset	29.2 μs	29.55 μs
pulse tempered ratio	0.5	1.0
log (evidence)		-11181.21526

harmonics of the original 0.5 MHz wave. An illustration is provided in Figure 7.15a for two waves, and Figure 7.16a for three waves. It is seen that the bubble is really quite sensitive to the driving wave. The number of parameters increases and the fit improves, but



(a)

Figure 7.15: Fit when the driving wave is a superposition of two pulses

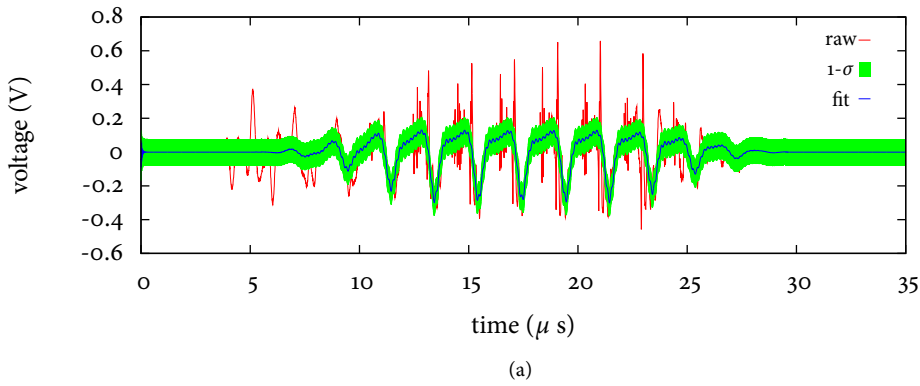
Table 7.4: Parameters for Figure 7.15a

Parameter	Initial 1	Fitted 1
scale factor	3000	1980
standard-deviation	0.07973 V	0.07910 V
bubble radius	0.3426 μm	0.2959 μm
pulse 1 amplitude	0.1357 MPa	0.1334 MPa
pulse 1 offset	29.55 μs	29.51 μs
pulse 1 tempered ratio	0.5	0.65021
pulse 2 amplitude	0.01 MPa	0.0070827 MPa
pulse 2 offset	29.3 μs	29.254 μs
pulse 2 tempered ratio	0.5	0.50386
log (evidence)		-11443.50021

from the evidence value it is seen that the quality of the model decreases. The reason is that the parameters space that can be explored grows faster than the improved fitness of the model.

Secondly we can attempt to model the limited bandwidth of the imaging transducer. We Fourier filter the model and multiply the frequency spectrum with a Gaussian. The free parameters of the filter are

1. central frequency,



(a)

Figure 7.16: Fit when the driving wave is a superposition of three pulses

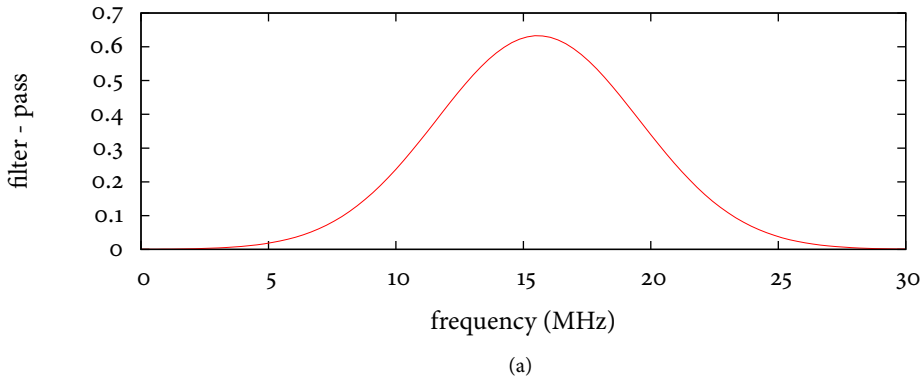
Table 7.5: Parameters for Figure 7.16a

Parameter	Initial 1	Fitted 1
scale factor	2447	2507.1
standard-deviation	0.07910 V	0.07910 V
bubble radius	0.2959 μm	0.2932 μm
pulse 1 amplitude	0.1334 MPa	0.1295 MPa
pulse 1 offset	29.51 μs	29.51 μs
pulse 1 tempered ratio	0.65021	0.66728
pulse 2 amplitude	0.0070827 MPa	0.007957 MPa
pulse 2 offset	29.254 μs	29.23 μs
pulse 2 tempered ratio	0.50386	0.51508
pulse 3 frequency	10.0 MHz	6.1037 MHz
pulse 3 amplitude	0.0001 MPa	0.007137 MPa
pulse 3 offset	29.3 μs	29.27 μs
pulse 3 tempered ratio	0.5	0.74246
log (evidence)		-11582.22102

2. amplitude

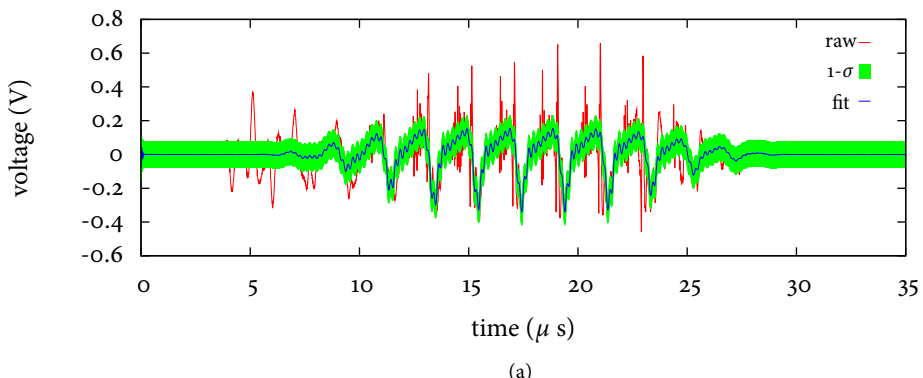
3. width

The filter is shown in Figure 7.17a and the effect of the filter is shown in Figure 7.18a.



(a)

Figure 7.17: The filter used in the fit



(a)

Figure 7.18: The resultant fit when the pressure has been Fourier filtered, 1.4 MPa

Unsurprisingly filtering the pulse accentuates the higher frequency oscillations in the modelled signal. It does not however, model the short peaks that are seen in the experimental result.

Attempts to model multiple waves did not help. The peaks are a small section of the imaging wave and do not contribute much to the likelihood at the give levels of noise. A model that treats the bubble interaction as noise results has higher probability.

7.4 DISCUSSION

This chapter has presented an experimental attempt to find the high frequency back scatter of a generated bubble. This was attempted by means of finding the excess pressure.

Table 7.6: Parameters for Figure 7.18a

Parameter	Initial 1	Fitted 1
scale factor	2447	3490
standard-deviation	0.07910 V	0.079354 V
bubble radius	0.2959 μm	0.2854 μm
pulse 1 amplitude	0.1334 MPa	0.15067 MPa
pulse 1 offset	29.51 μs	29.48 μs
pulse 1 tempered ratio	0.65021	0.69596
pulse 2 amplitude	0.0070827 MPa	0.014243 MPa
pulse 2 offset	29.254 μs	29.30 μs
pulse 2 tempered ratio	0.50386	0.66594
pulse 3 frequency	10.0 MHz	4.5867 MHz
pulse 3 amplitude	0.0001 MPa	0.00024382 MPa
pulse 3 offset	29.3 μs	29.12 μs
pulse 3 tempered ratio	0.5	0.65243
Fourier frequency	20 MHz	18.771 MHz
Fourier variance	5 MHz	11.389 MHz
Fourier amplitude	1.0	7.2076e+00
log (evidence)		-11845.16088

It is worth now revisiting the objectives of chapter 6 and discussing what has been achieved and what tasks remain.

Determine whether bubbles can be evacuated and detected This objective has been convincingly achieved. Both the preliminary study of chapter 6 and the spiked response of Figure 7.1 in this chapter demonstrate the characteristics of bubble imaging modelled in chapter 5.

Determine whether an evacuated bubbles can be *imaged by pulse-echo* Figure 7.9 is strongly suggestive that the nucleated bubbles are responding to the high fre-

quency imaging wave. The response is not strong, however, which suggests that the generated bubbles are far from resonance.

Determine if the precise location of the bubble can be determined. The excess pressure plots of Figure 7.9 do not locate the echo of a particular bubble. There are two possible causes. The first is that there is a population of bubbles that are interacting with the acoustic wave. This possibility seems likely when Apfel's^[4] molar density of 10^5 cm^{-3} is remembered. Secondly, Figure 7.9 is evaluated with average traces. Even if the returned scatter really were coming from a single bubble, its location would be smeared in the average.

Determine whether the acoustic Keller-Miksis predicts the echo As was anticipated in chapter 6, the attempt to fit a bubble model to the returned signal was not successful. There are too many undetermined parameters in our experimental setup, with the population of generated bubbles being the most chaotic. To test the acoustic model a single, well characterised bubble is needed. It is not appropriate to attempt its test when generating a short lived bubble acoustically.

To improve the results of this chapter a more systematic study of the acoustic medium is needed. Once the size of the bubbles that are generated is better understood, a more careful tuning can be carried out for selecting optimal driving and acoustic pulses.

The lifetime of the generated bubbles is an effective method for determining their radius. This method was attempted in this thesis, but unfortunately it was carried out too slowly. The gas in the solution was not sufficiently stable to prevent the gas leaving the medium after a few thousand pulses.

PART IV

DISCUSSION

DISCUSSION

The goal of this thesis was to address the restriction of medical contrast ultrasound to imaging the vasculature. The starting premise was that to achieve this goal a contrast agent - be it a bubble or an agent that can assist in the generation of a bubble - needs to be an order of magnitude smaller in size than what is currently available commercially. Since small bubbles are typically short lived, we concentrated in this thesis on the task of acoustically generating a bubble and then immediately imaging it. We considered the direct cavitation of water and the cavitation of perfluorocarbon emulsions.

While other groups^[17;25;63;92;95;98] have made great progress with the creation and experimental nucleation of perfluorocarbon emulsions, in this thesis we concentrated on the acoustic process of generating and imaging a small bubble. This thesis has introduced a two wave imaging technique - designed to generate and then immediately image a bubble - and developed it from its theoretical foundation through to experiment.

The key themes are:

1. The nucleation of a bubble (chapter 2).
2. The response of the bubble contrast agent to an acoustic wave as *measured by ultrasound* (chapter 4).
3. The response of a bubble to the two acoustic waves, the cavitation (driving) wave and the imaging wave (chapter 5).

The acoustic nucleation of a bubble was discussed in chapter 2. There the capillary approximation was used to test the applicability of the technique. It was found that type I nucleation, even of chemicals with low boiling points such as the perfluorocarbons, was likely to be beyond the capabilities of diagnostic ultrasound. Not wanting to diverge from the technological norms of diagnostic imaging prompted the consideration of type III nucleation of water in our experimental chapters.

The validity of the capillary approximation was also considered in chapter 2. It was found to fall short in the case of the perfluorocarbons, where the distance over which vapour becomes medium is a significant fraction of the bubble's critical radius. Calculating this density profile demonstrated that a density functional approach would have much to offer the theoretical understanding of the acoustic nucleation of perfluorocarbon bubbles. In particular, the high solubility of the perfluorocarbons to gasses such as carbon dioxide suggest that a study of the nucleation of these gases would be fruitful future work.

The low frequency wave that is used to initiate bubble formation will also influence the response of the bubble to a higher frequency imaging pulse. It does so, as was determined in chapter 5, by altering the size of the bubble so that it is either closer or further from its resonance frequency. This has implications for bubble imaging when the bubble is long standing and is generated by other means. One such application would be high frequency contrast imaging for small animals. Chapter 5 also introduced a two pulse technique to remove ambiguities in the echo location of bubbles that can exist when using two acoustic waves. It was found that significant excess pressure can be generated when using a driving wave and imaging wave of around 0.5 MHz and 20 MHz. The response to the high frequency wave occurs at a lower frequency than would be expected from the calculated resonance due to the altered phase space orbit of the bubble's response to the driving wave.

Finally, chapter 6 and chapter 7 presented the design and then results of the two wave imaging technique of chapter 5. The results, if not conclusive, are certainly suggestive of the techniques success and warrant further study and refinement. Ambiguities regard-

ing the bubble population would need to be resolved to move forward experimentally. The changing population of bubbles meant that the two wave technique of chapter 5 was difficult to apply.

And so where have we come in the goal of extending medical contrast imaging? Firstly, the view of the author is that this thesis greatly complements the experimental work of other groups in the field. This thesis has argued the need for a density functional approach to understanding the nucleation of the contrast agents currently being investigated by others. Secondly, with the analysis of the phase-space interactions between the driving wave and imaging wave, a degree of intuition is possible as to the degree of ringing that would be expected from a given driving and imaging wave profile. Such intuition is vital for designing experimental tests. Thirdly, while there were difficulties in applying the two wave technique introduced in this thesis to a cloud of bubbles, the author still believes that it has much to offer when applied to single bubble experiments.

By far the most significant achievement of this thesis is found in chapter 3. Ultrasound physicists have since the very beginning of their subject propagated the curious error of defining their spatial and temporal coordinates with light. When sound is used, as it should be for an acoustic measurement technology, one finds that acoustics is a relativistic subject where the speed of sound has a privileged role. It follows that ultrasound cannot measure a bubble wall collapsing at faster than the speed of sound, and in chapter 4 a new bubble model that has this property was derived. Further, an exact correspondence between acoustics and electromagnetism exists. As a direct consequence of this result it follows that

1. sound is a transverse wave of vorticity and Coriolis acceleration,
2. sound has helicity that corresponds to the hydrodynamic helicity. Sound has integer spin.
3. There exists an acoustic current that is conserved.
4. The acoustic current obeys an acoustic analogue to the Lorentz force law.

The importance of these observations should not be underestimated.

Given the existence of an *acoustic spin*, and a conserved *acoustic charge*, that obeys an *acoustic Lorentz force law*, it does not seem to far fetched to ask whether there exists an *acoustic electron*. Such an idea, of course, revives the very old theories of Bjerkness^[9], Maxwell^[71] and Thomson^[109]. All that we say on the matter is to note that Hick's spherical vortex, the favoured model of many in the nineteenth century, has a conserved angular momentum^[80;81] and a conserved spin^[73;74] when measured acoustically.

Finally, we have shown that there is nothing intrinsically special to light. The significance of the speed of light results from its role in the measurement process. It is privileged if we believe only what we see. There is much to understand in the world if we are prepared to be more open minded.

PART V

APPENDICES

A

TENSOR DERIVATION TO MAXWELL'S EQUATIONS

A.1 INTRODUCTION

In chapter 3 Geometric Algebra was used for the derivations. Since Geometric Algebra is not of widespread use in the physics community, this appendix repeats the derivation using Tensor Algebra. The same equation numbers will be used in this appendix so the derivations can be easily compared. Doing so makes a good advert for the economy of expression afforded by Geometric Algebra.

A.2 THE ACOUSTICS ANALOGUE TO MAXWELL'S RELATION

The energy-momentum tensor of an ideal fluid is^[60;108]

$$T^{ij} = (\varepsilon + p)u^i u^j - g^{ij}p \quad (3.13)$$

where, $\varepsilon \equiv \varepsilon(p)$ is the barotropic total energy density, p is the pressure, g^{ij} is a diagonal metric tensor with $g^{00} = 1$ and $g^{ii} = -1$ for $i = 1, 2, 3$, and u is the velocity vector of the spacetime path, with the parametrisation chosen such that $u^2 = u^i u_i = 1$. That is, the units of length and time are chosen so that velocity of sound is set to unity.

The speed of sound, c , given at constant entropy density, σ , is^[60;108]

$$c^2 = \left. \frac{\partial p}{\partial \varepsilon} \right|_{\sigma}. \quad (3.14)$$

This is the same as the non-relativistic expression except that the energy density has replaced the mass density. The speed of sound equals the speed of light (unity) if

$$\varepsilon(p) = p. \quad (3.15)$$

This equation of state was first introduced by Taub^[108].

Applying 3.15 to 3.13 simplifies the energy momentum tensor,

$$T^{ij} = p(2u^i u^j - g^{ij}) \equiv \frac{\Xi_0^2}{2}(A^i A^j - A^k A_k g^{ij}/2) \quad (3.16)$$

where the vector potential, A , satisfies

$$A^i = 2\frac{1}{\Xi_0} p^{1/2} u^i = 2\frac{1}{\Xi_0} \varepsilon^{1/2} u^i. \quad (3.17)$$

The constant scale-factor, Ξ_0 , is determined from the ambient proper number density of the fluid, n_0 , and the ambient pressure, p_0 , as follows,

$$\Xi_0 = \frac{n_0}{\sqrt{p_0}}. \quad (3.18)$$

The motivation for introducing the 4-vector A is that it represents a potential flow. To demonstrate this, we first note that the relativistic generalisation to the velocity potential, ψ , is defined^[60] by

$$\partial_i \psi \equiv -\frac{\varepsilon + p}{n} u_i = -\frac{2p}{n} u_i, \quad (3.19)$$

where $\partial_j \equiv \frac{\partial}{\partial x^j}$ and n is the proper particle number density of the fluid. Equation 3.15 has been used to obtain the second equality. To show that this is equal to the negative of the potential A , we use a thermodynamic argument given by Taub^[108]. The internal energy density, ε , is equal to the sum of the rest mass and the internal energy per

particle^[60;108], e ,

$$\varepsilon(p) = nm(1 + e(p)), \quad (3.20)$$

where m is the particle mass at rest. From the isentropic thermodynamic relation $mde = -pd\left(\frac{1}{n}\right)$ it follows that

$$nd\varepsilon = \varepsilon dn - n^2 pd\left(\frac{1}{n}\right) = (\varepsilon + p) dn. \quad (3.21)$$

Applying equation 3.15 and integrating we obtain

$$n = \Xi_0 \sqrt{p}, \quad (3.22)$$

where Ξ_0 is the constant introduced in 3.18. With the aid of equation 3.15 it follows that

$$A_i = 2\frac{1}{\Xi_0} \sqrt{p} u_i = \frac{\varepsilon + p}{n} u_i = -\partial_i \psi, \quad (3.23)$$

as asserted.

In the absence of external fields, the equations of motion are obtained by setting the divergence of the energy momentum tensor (equation 3.16) to zero. By projecting the divergence of 3.16 along the timelike component we find

$$u_i \partial_j T^{ij} = \frac{1}{2} \Xi_0^2 u_i A^i \partial_j A^j = 0. \quad (3.24)$$

Since, from 3.17, the vector A is parallel to u it follows that

$$\partial_j A^j = 0 \quad (3.25)$$

and so the vector potential A is conserved. The spacelike projection, $\partial_j T^{kj} -$

$u^k u_i \partial_j T^{ij}$, gives in turn,

$$u_j \left(\partial^j A^k - \partial^k A^j \right) = 0. \quad (3.26)$$

The relativistic vorticity tensor, F^{jk} , is the exterior derivative of the vector potential,

$$F^{jk} \equiv \partial^j A^k - \partial^k A^j \quad (3.27)$$

and so 3.26 implies that the vorticity tensor is orthogonal to the velocity.

By taking the divergence of 3.27 and using 3.25 it follows that

$$\partial_i \partial^i A^j = \partial_i F^{ij}. \quad (3.28)$$

The left-hand-side of equation 3.28 is a wave equation and so we interpret the right-hand-side as an acoustic source, a 4-current, J . Therefore

$$\partial_i F^{ij} \equiv J^j. \quad (3.30a)$$

Furthermore, from 3.27 we have

$$\varepsilon_{ijkl} \partial^j F^{kl} = \varepsilon_{ijkl} \partial^j \left(\partial^k A^l - \partial^l A^k \right) = 0, \quad (3.30b)$$

which follows due to the use of the repeated differential with the Levi-Civita permutation tensor, ε_{ijkl} . The two equations of 3.29 constitute Maxwell's relation and equation 3.25 has specified the Lorenz gauge.

CLASSICAL NUCLEATION THEORY

B.1 INTRODUCTION

In section 2.2.2 the derivation of classical nucleation theory was very briefly sketched. To help this thesis be self contained we fill in the details here.

B.1.1 THE POYNTING CORRECTION

The bubble is in thermodynamic equilibrium when it is at its critical radius,

$$a^* = \frac{2\gamma}{p_v - p_L}. \quad (2.4)$$

Then the chemical potentials are equal

$$\mu_v(p_v^*) = \mu_L(p_L). \quad (2.7)$$

However, due to the curvature of the bubble, the critical pressure within the bubble, p_v^* , is not the same as the equilibrium vapour pressure. At a flat interface the vapour pressure is p_∞ (where the ∞ denotes the radius of the bubble for a flat interface). The flat interface is therefore at equilibrium when

$$\mu_v(p_\infty) = \mu_L(p_\infty). \quad (B.1)$$

Equations 2.7 and B.1 are related by the Gibbs-Duhem relation,

$$d\mu = -s dT + \nu dp, \quad (\text{B.2})$$

where s and ν are the entropy and volume per molecule and T is the temperature.

Choosing an adiabatic path for the chemical potential of the vapour gives

$$\mu_v(p_v) - \mu_v(p_\infty) = \int_{p_\infty}^{p_v^*} \nu dp. \quad (\text{B.3})$$

Similarly for the liquid we have

$$\mu_L(p_L) - \mu_v(p_\infty) = \int_{p_\infty}^{p_L} \nu dp. \quad (\text{B.4})$$

Assuming the gas is ideal, so that $p\nu = k_B T$, B.3 gives

$$\mu_v(p_v^*) - \mu_v(p_\infty) = k_B T \ln\left(\frac{p_v^*}{p_\infty}\right). \quad (\text{B.5})$$

Using equations 2.7 and B.1 we may equate equations B.3 and B.4 to obtain

$$p_v^* = p_\infty \exp\left(\int_{p_\infty}^{p_L} dp \frac{V}{RT}\right) \quad (\text{B.6})$$

where V is the molar volume. Equation B.6 is known as the Poynting correction. If the fluid is incompressible with number density N_L (per mole) then we may write

$$p_v^* = p_\infty \exp\left(\frac{(p_L - p_\infty)}{N_L RT}\right), \quad (\text{B.5})$$

which is the result quoted in section 2.2.2

An alternative derivation is to start from Kelvin's equation,

$$\ln\left(\frac{p_v}{p_\infty}\right) = -\frac{2\gamma}{aN_L RT}, \quad (\text{B.7})$$

which more directly relates pressure and curvature. (see Skinner's review^[101] for

derivation and general discussion). Equation 2.5 follows immediately by substituting 2.4 into B.7.

BIBLIOGRAPHY

- [1] *Convertible Liquid Droplets for Ultrasound Contrast*, Rotterdam, The Netherlands, January 2010. 15th European Symposium on Ultrasound Contrast Imaging.
- [2] R.G.W. Anderson. Caveolae - where incoming and outgoing messengers meet. *Proceedings of the National Academy of Sciences of the United States of America*, 90(23):10909–10913, Dec 1993.
- [3] B. Angelsen and R. Hansen. Surf imaging – a new method for ultrasound contrast agent imaging. pages 531–541. IEEE Ultrasonics Symposium Proceedings, 2007.
- [4] R.E. Apfel. Acoustic cavitation inception. *Ultrasonics*, 22(4):167 – 173, 1984. ISSN 0041-624X. doi: DOI: 10.1016/0041-624X(84)90032-5.
- [5] A. A. Atchley and A. Prosperetti. The crevice model of bubble nucleation. *Acoustical Society of America Journal*, 86:1065–1084, September 1989. doi: 10.1121/1.398098.
- [6] B. Ballou, B.C. Lagerholm, L.A. Ernst, M.P. Bruchez, and A.S. Waggoner. Non-invasive imaging of quantum dots in mice. *Bioconjugate Chemistry*, 15(1):79–86, 2004.
- [7] Carlos Barceló, Stefano Liberati, and Matt Visser. Analogue gravity. *Living Reviews in Relativity*, 8:12, 2005. arXiv:gr-qc/0505065v2.
- [8] Charles Baudelaire. The painter of modern life. In Jonathan Mayne, editor, *The Painter of Modern Life and Other Essays*. London: Phaidon Press, 1995.
- [9] Vilhelm Bjerknes. *Fields of Force: Supplementary lectures, applications to meteorology*. Cornell University Library, 1991, 1905.

- [10] S.H. Bloch, R.E. Short, K.W. Ferrara, and E.R. Wisner. The effect of size on the acoustic response of polymer-shelled contrast agents. *Ultrasound in Medicine and Biology*, 31(3):439–444, Mar 2005.
- [11] Bram M. Borkent, Stephan M. Dammer, Holger Schönherr, G. Julius Vancso, and Detlef Lohse. Superstability of surface nanobubbles. *Phys. Rev. Lett.*, 98(20):204502, May 2007. doi: 10.1103/PhysRevLett.98.204502.
- [12] Bram M. Borkent, Stephan Gekle, Andrea Prosperetti, and Detlef Lohse. Nucleation threshold and deactivation mechanisms of nanoscopic cavitation nuclei. *Physics of Fluids*, 21(10):102003, 2009. doi: 10.1063/1.3249602.
- [13] CGPM Comptes Rendus of the Conférence Générale des Poids et Mesures. The 17th conférence générale des poids et mesures, 1984, 20, 25.
- [14] Oliver Couture, Peter D. Bevan, Emmanuel Cherin, Kevin Cheung, Peter N. Burns, and F. Stuart Foster. Investigating perfluorohexane particles with high-frequency ultrasound. *Ultrasound in Medicine and Biology*, 32(1):71–82, 2006.
- [15] R. T. Cox. Probability, frequency and reasonable expectation. *American Journal of Physics*, 14(1):1–13, January–February 1946.
- [16] Can F. Delale, Jan Hruby, and Frantisek Marsik. Homogeneous bubble nucleation in liquids: The classical theory revisited. *The Journal of Chemical Physics*, 118(2):792–806, 2003. doi: 10.1063/1.1525797.
- [17] Alexander A. Doinikov, Paul S. Sheeran, Ayache Bouakaz, and Paul A. Dayton. Vaporization dynamics of volatile perfluorocarbon droplets: A theoretical model and in vitro validation. *Medical Physics*, 41(10):102901, 2014. doi: <http://dx.doi.org/10.1118/1.4894804>.
- [18] Carl E. Dolby and Stephen F. Gull. On radar time and the twin ‘paradox’. *American Journal of Physics*, 69(12):1257–1261, October 2001.
- [19] Chris Doran and Anthony Lasenby. *Geometric Algebra for Physicists*. Cambridge University Press, 2003.

- [20] A. Einstein. Zur elektrodynamik bewegter körper. *Annalen der Physik*, 17:891–921, 1905. English translation available in *The Principle of Relativity*, Dover, 1952.
- [21] P. S. Epstein and M. S. Plesset. On the stability of gas bubbles in liquid-gas solutions. *Journal of Chemical Physics*, 18(11):1505–1509, 1950.
- [22] Lina Du et al. Ultrasound-triggered drug release and enhanced anti-cancer effect of doxorubicin-loaded poly(d,l-lactide-co-glycolide)-methoxy-poly(ethylene glycol) nanodroplets. *Ultrasound in Medicine and Biology*, 37(8):1252–1258, 2011.
- [23] Natalya Rapoport et al. Cavitation properties of block copolymer stabilized phase-shift nanoemulsions used as drug carriers. *Ultrasound in Medicine and Biology*, 36:419–429, 2007.
- [24] R Evans. Density functionals in nonuniform fluids. In D Henderson, editor, *Fundamentals of Inhomogeneous Fluids*, pages 85–175. Marcel Dekker, Inc, 1992.
- [25] Mario L. Fabiilli, Kevin J. Haworth, Ian E. Sebastian, Oliver D. Kripfgans, Paul L. Carson, and J. Brian Fowlkes. Delivery of chlorambucil using an acoustically-triggered perfluoropentane emulsion. *Ultrasound in Medicine & Biology*, 36(8):1364 – 1375, 2010. ISSN 0301-5629. doi: DOI: 10.1016/j.ultrasmedbio.2010.04.019.
- [26] P. Favvas and A. Ch. Mitropoulos. What is spinodal decomposition? *Journal of Engineering Science and Technology Review*, 1:25–27, 2008.
- [27] Katherine Ferrara, Rachel Pollard, and Mark Borden. Ultrasound microbubble contrast agents: Fundamentals and application to gene and drug delivery. *Annual Review of Biomedical Engineering*, 9(1):415–447, 2007. doi: 10.1146/annurev.bioeng.8.061505.095852.
- [28] L. M. Fisher. Company news; f.d.a. approves compound for heart scans. *New York Times*, 09 August 1994.
- [29] M. Foucault. What is enlightenment. In P. Rabinow, editor, *The Foucault Reader*. Penguin Books, 1984, 1978.

- [30] Y. Fukumori and H. Ichikawa. Nanoparticles for cancer therapy and diagnosis. *Advanced Powder Technology*, 17(1):1–28, 2006.
- [31] M. S. Garrido. Note sur la mécanique relativiste des fluides incompressibles. *Il Nuovo Cimento*, 68B(2):252–260, Apr 1982.
- [32] T. Giesecke and K. Hynynen. Ultrasound-mediated cavitation thresholds of liquid perfluorocarbon droplets in vitro. *Ultrasound in Medicine and Biology*, 29(9):1359–1365, Sep 2003.
- [33] Peter Goldreich, Sanjoy Mahajan, and Sterl Phinney. *Order-of-Magnitude Physics: Understanding the World with Dimensional Analysis, Educated Guesswork, and White Lies*. unpublished, 1999.
- [34] Gennady Yu. Gor, Anatoly E. Kuchma, and Fedor M. Kuni. Gas bubble growth dynamics in a supersaturated solution: Henry’s and sievert’s solubility laws. *JINR Dubna*, pages 213–233, 2011. arXiv:1205.5471 [physics.chem-ph].
- [35] H. Hashizume, P. Baluk, and S. Morikawa et al. Openings between defective endothelial cells explain tumor vessel leakiness. *American Journal of Pathology*, 156(4):1363–1380, Apr 2000.
- [36] Edvard A. Hemmingsen. Cavitation in gas - supersaturated solutions. *Journal of Applied Physics*, 46(1):213–218, 1975. doi: 10.1063/1.321323.
- [37] Eric Herbert, Sébastien Balibar, and Frédéric Caupin. Cavitation pressure in water. *Phys. Rev. E*, 74(4):041603, Oct 2006. doi: 10.1103/PhysRevE.74.041603.
- [38] D. Hestenes. Spacetime physics with geometric algebra. *American Journal of Physics*, 71(7):691–714, July 2003.
- [39] David Hestenes and Garret Sobczyk. *Clifford Algebra to Geometric Calculus: A Unified Language for Mathematics and Physics*. D. Reidel Publishing Company, Kluwer Academic Publishers Group, 1984.
- [40] S.K. Hobbs, Wayne L. Monsky, Fan Yuan, W. Gregory Robertspur, Linda Grifithdagger, Vladimir P. Torchilin, and Rakesh K. Jain. Regulation of transport

- pathways in tumor vessels: Role of tumor type and microenvironment. *Proceedings of the National Academy of Sciences of the United States of America*, 95(8):4607–4612, Apr 1998.
- [41] L Hoff. *Acoustic Characterisation of Contrast Agents for Medical Ultrasound Imaging*. Kluser Academic Publishers, 2001.
 - [42] M. S. Howe. *Acoustics of Fluid-Structure Interactions*. Cambridge Monographs on Mechanics. Cambridge University Press, 1998.
 - [43] M. S. Howe. *Theory of Vortex Sound*. Cambridge Texts in Applied Mathematics. Cambridge University Press, 2003.
 - [44] J.A. Copland JA, M. Eghitedari, V.L. Popov VL, N. Kotov, N. Mamedova, M. Mamedi, and A.A. Oraevsky AA. Bioconjugated gold nanoparticles as a molecular based contrast agent: Implications for imaging of deep tumors using optoacoustic tomography. *Molecular Imaging and Biology*, 6(5):341–349, Sep-Oct 2004.
 - [45] Thomas J. Jarvis, Marc D. Donohue, and Joseph L. Katz. Bubble nucleation mechanisms of liquid droplets superheated in other liquids. *Journal of Colloid and Interface Science*, 50(2):359–368, 1975. ISSN 0021-9797. doi: DOI: 10.1016/0021-9797(75)90240-4.
 - [46] E. T. Jaynes. Where do we stand on maximum entropy? In R. D. Levine and M. Tribus, editors, *The Maximum Entropy Formalism*, page 15. M.I.T. Press, Cambridge, MA, 1979.
 - [47] Edwin T. Jaynes. The well-posed problem. *Foundations of Physics*, 3:477–493, 1973.
 - [48] Bruce D. Johnson and Robert C. Cook. Generation of Stabilized Microbubbles in Seawater. *Science*, 213(4504):209–211, 1981. doi: 10.1126/science.213.4504.209.
 - [49] S. F. Jones, G. M. Evans, and K. P. Galvin. Bubble nucleation from gas cavities – a review. *Advances in Colloid and Interface Science*, 80(1):27 – 50, 1999. ISSN 0001-8686. doi: DOI: 10.1016/S0001-8686(98)00074-8.

- [50] JL Katz. Homogeneous nucleation theory and experiment - a survey. *Pure and applied chemistry*, 64(11):1661–1666, Nov 1992. ISSN 0033-4545. 7TH International conference on surface and colloid science, Compiegne, France, JUL 07-13, 1991.
- [51] Joseph L. Katz and Milton Blander. Condensation and boiling: Corrections to homogeneous nucleation theory for nonideal gases. *Journal of Colloid and Interface Science*, 42(3):496–502, 1973. ISSN 0021-9797. doi: DOI: 10.1016/0021-9797(73)90035-0.
- [52] Joseph B. Keller and Michael Miksis. Bubble oscillations of large amplitude. *Journal of the Acoustical Society of America*, 68(2):628–633, Aug 1980.
- [53] I.A. Khalil, K. Kogure, and H. Akita et al. Uptake pathways and subsequent intracellular trafficking in nonviral gene delivery. *Pharmacological Reviews*, 58(1):32–45, Mar 2006.
- [54] C.S. Kiang, D. Stauffer, G.H Walker, O.P. Puri, J.D Wise, and E.M. Patterso. Re-examination of homogeneous nucleation theory. *Journal of the atmospheric sciences*, 28(7):1222–&, 1971. ISSN 0022-4928.
- [55] Kevin H. Knuth. Lattice duality: The origin of probability and entropy. *Neurocomputing*, 67:245–274, 2005.
- [56] Kevin H. Knuth and John Skilling. Foundations of inference. *Axioms*, 1(1):38–73, 2012.
- [57] O. D. Kripfgans, J. B. Fowlkes, D. L. Miller, O. P. Eldevik, and P. L. Carson. Acoustic droplet vaporization for therapeutic and diagnostic applications. *Ultrasound in Medicine and Biology*, 26(1177-1189), 2000.
- [58] O.D. Kripfgans, J.B. Fowlkes, M. Woydt abd O.P. Eldevik, and P.L. Carson. In vivo droplet vaporization for occlusion therapy and phase aberration correction. *IEEE Transactions on Ultrasonics Ferroelectrics and Frequency Control*, 49(6):726–738, Jun 2002.

- [59] O.D. Kripfgans, M.L. Fabiilli, P.L. Carson, and J.B. Fowlkes. On the acoustic vaporization of micrometer-sized droplets. *Journal of the Acoustical Society of America*, 116(1):272–281, Jul 2004.
- [60] L.D. Landau and E.M. Lifshitz. *Fluid Mechanics*. Number 6 in Course of Theoretical Physics. Elsevier Butterworth Heinemann, 2nd edition, 1987.
- [61] A.N. Lasenby, C.J.L. Doran, and S.F. Gull. A multivector derivative approach to lagrangian field theory. *Foundations of Physics*, 23(10):1295–1327, 1993.
- [62] M. J. Lighthill. On sound generated aerodynamically. i. general theory. *Proc. R. Soc. Lond. A*, 211(1107):564–587, 20 March 1952.
- [63] Chung-Yin Lin and William G. Pitt. Acoustic droplet vaporization in biology and medicine. *BioMed Research International*, 2013. doi:10.1155/2013/40436.
- [64] P.J. Linstrom and W.G. Mallard, editors. *NIST Chemistry WebBook, NIST Standard Reference Database*. Number 69. National Institute of Standards and Technology, Gaithersburg MD, 20899, 2010.
- [65] Stig Ljunggren and Jan Christer Eriksson. The lifetime of a colloid-sized gas bubble in water and the cause of the hydrophobic attraction. *Colloids and Surfaces A: Physicochemical and Engineering Aspects*, 129-130:151 – 155, 1997. ISSN 0927-7757. doi: DOI: 10.1016/S0927-7757(97)00033-2. Prof. B. W. Ninham.
- [66] S. D. Lubetkin. The fundamentals of bubble evolution. *Chem. Soc. Rev.*, 24:243–250, 1995. doi: 10.1039/CS9952400243.
- [67] Jacques Lusseyran. *Against the pollution of the I.* Morning Light Press, 2006. Essay entitled: The Blind in Society.
- [68] D.J.C. MacKay. *Information Theory, Inference & Learning Algorithms*. Cambridge University Press, 2003.
- [69] D.J.C. MacKay. *Information Theory, Inference & Learning Algorithms*. Cambridge University Press, 2003.

- [70] Haralabos Marmanis. *Analogy between the Electromagnetic and Hydrodynamic Equations: Application to Turbulence*. PhD thesis, Brown University, 2000.
- [71] J. C. Maxwell. On physical lines of force. *The London, Edinburgh and Dublin Philosophical Magazine and Journal of Science*, pages 161–175, March 1861.
- [72] G.M. Lanza MD, P.M. Winter, S.D. Caruthers, A.M. Morawskia, A.H. Schmiedera, K.C. Crowder, and S.A. Wickline. From bench to imaging: Magnetic resonance molecular imaging with nanoparticles. *Journal of Nuclear Cardiology*, 11(6):733–743, 2004.
- [73] H. K. Moffatt. The degree of knottedness in tangled vortex lines. *Journal of Fluid Mechanics*, 35(1):117–129, 1969.
- [74] H. K. Moffatt. Generalised vortex rings with and without swirl. *Fluid Dynamics Research*, 3:22–30, 1988.
- [75] J. A. Nelder and R. Mead. A simplex method for function minimization. *Computer Journal*, 7:308–313, 1965.
- [76] R.M. Nyquist, V. Talanquer, and D.W. Oxtoby. Density-functional theory of nucleation - a semiempirical approach. *Journal of Chemical Physics*, 103(3):1175–1179, JUL 15 1995. ISSN 0021-9606.
- [77] David W. Oxtoby. Nucleation. In D Henderson, editor, *Fundamentals of Inhomogeneous Fluids*, pages 407–442. Marcel Dekker, Inc, 1992.
- [78] David W. Oxtoby and R. Evans. Nonclassical nucleation theory for the gas–liquid transition. *The Journal of Chemical Physics*, 89(12):7521–7530, 1988. doi: 10.1063/1.455285.
- [79] Hong-Chul Park, Ki-Taek Byun, and Ho-Young Kwak. Explosive boiling of liquid droplets at their superheat limits. *Chemical Engineering Science*, 60(7):1809 – 1821, 2005. ISSN 0009-2509. doi: DOI: 10.1016/j.ces.2004.11.010.
- [80] C. L. Pekeris. A relativistic spherical vortex. *Proceedings of the National Academy of Sciences of the United States of America*, 73(3):687–691, March 1976.

- [81] C. L. Pekeris. Relativistic axially symmetric flows of a perfect fluid. *Proceedings of the Royal Society of London. Series A, Mathematical and Physical Sciences*, 355 (1680):53–60, Jun. 30 1977.
- [82] Y.G.A Pierseaux. Einstein’s quantum clocks and poincaré’s classical clocks in special relativity. arXiv:quant-ph/0101146v1, 2001.
- [83] Yves Pierseaux. Special relativity: EinsteinâŽs spherical waves versus poincaré ellipsoidal waves. *Annales de la Fondation Louis de Broglie*, 30(3-4):353–379, 2005.
- [84] Henri Poincaré. La mesure du temps. *Revue de mÃltaphysique et de morale* 6, 1898. English translation used: The Foundations of Science (The Value of Science) 1913, New York: Science Press, Translator: George Bruce Halsted.
- [85] Henri Poincaré. *Science and Hypothesis*. English translation used: The Walter Scott Translation Co. Ltd. 1905, 1902.
- [86] Henri Poincaré. Sur la dynamique de l’électron. *Rendiconti del Circolo Matematico di Palermo*, 21:129–175, 1906. English translation for part 1 (used here) available from H.M. Schwartz, American Journal of Physics, November 1971, Volume 39, 1287–1294.
- [87] Henri Poincaré. La dynamique de l’électron. *Revue gÃlnÃlrale des sciences pures et appliquÃlles*, 19:386–402, 1908.
- [88] Henri Poincaré. *The Foundations of Science (Science and Method: Book2)*. Science and Education. New York: Science Press, 1913. Translator: George Bruce Halsted.
- [89] Karl Popper. *The Logic of Scientific Discovery*. Routledge Classics, 2002, 1934.
- [90] Antonio F. Rañada. Topological electromagnetism. *J. Phys. A: Math. Gen.*, 25: 1621, 1992. doi: DOI: 10.1088/0305-4470/25/6/020.
- [91] Antonio F. Rañada and José Trueba. Topological electromagnetism with hidden nonlinearity. In Myron W. Evans, editor, *Modern Nonlinear Optics, Part III*, volume 119 of *Advances in Chemical Physics*, pages 197–253. John Wiley & Sons, Inc., 2nd edition, 2002.

- [92] Natalya Rapoport, Zhonggao Gao, and Anne Kennedy. Multifunctional nanoparticles for combining ultrasonic tumor imaging and targeted chemotherapy. *J. Natl. Cancer Inst.*, 99:1095–1106, 2007.
- [93] K. Sarkar, A. Katiyar, and P. Jain. Growth and dissolution of an encapsulated contrast microbubble: effects of encapsulation permeability. *Ultrasound in Medicine and Biology*, 35(8):1385–1396, Aug 2009.
- [94] Kelly C Schad. Characterization of perfluorocarbon droplets for focused ultrasound therapy. Master’s thesis, University of Toronto, 2009.
- [95] Paul S Sheeran, Terry O Matsunaga, and Paul A Dayton. Phase-transition thresholds and vaporization phenomena for ultrasound phase-change nanoemulsions assessed via high-speed optical microscopy. *Physics in Medicine and Biology*, 58(13):4513, 2013. URL <http://stacks.iop.org/0031-9155/58/i=13/a=4513>.
- [96] T.H. Shorrock. hardware. Available on <https://github.com/thshorrock>, 2012.
- [97] T.H. Shorrock. Dft. Available on <https://github.com/thshorrock>, 2012.
- [98] Oleksandr Shpak, Laura Stricker, Michel Versluis, and Detlef Lohse. The role of gas in ultrasonically driven vapor bubble growth. *Physics in Medicine and Biology*, 58(8):2523, 2013. URL <http://stacks.iop.org/0031-9155/58/i=8/a=2523>.
- [99] V.A. Shutilov. *Fundamental Physics of Ultrasound*. Gordaon and Breach Science Publishers, 1988.
- [100] John Skilling. Fundamentals of maxent in data analysis. In B. Buck and V. A. Macaulay, editors, *Maximum Entropy in Action: A Collection of Expository Essays*. Oxford University Press, 1991.
- [101] L.M Skinner and J.R Sambles. The kelvin equation-a review. *Journal of Aerosol Science*, 3(3):199 – 210, 1972. ISSN 0021-8502. doi: DOI: 10.1016/0021-8502(72)90158-9.

- [102] S. Sridhar. Turbulent transport of a tracer: An electromagnetic formulation. *Physical Review E*, 58(1):522–525, July 1998.
- [103] HPV Robust Summaries and Test Plan. Cas #86508-32-1 pefluoro compounds, c5-c18, including cas#311-89-7 perfluorotributyl amine. CAS.
- [104] V. Talanquer and D. W. Oxtoby. A density-functional approach to nucleation in micellar solutions. *The Journal of Chemical Physics*, 113(16):7013–7021, 2000. doi: 10.1063/1.1288271.
- [105] V. Talanquer and D.W. Oxtoby. Nucleation of Bubbles in Binary Fluids. *Journal of Chemical Physics*, 102(5):2156–2164, Feb 1 1995. ISSN 0021-9606.
- [106] V Talanquer and DW Oxtoby. Nucleation in the presence of an amphiphile: A density functional approach. *Journal of Chemical Physics*, 106(9):3673–3680, MAR 1 1997. ISSN 0021-9606.
- [107] V Talanquer, C Cunningham, and DW Oxtoby. Bubble nucleation in binary mixtures: A semiempirical approach. *Journal of Chemical Phsyics*, 114(15):6759–6762, APR 15 2001. ISSN 0021-9606.
- [108] A. H. Taub. Relativistic fluid mechanics. *Annual Reviews in Fluid Mechanics*, 10 (301–332), 1978.
- [109] J. J. Thomson. On the analogy between the electromagnetic field and a fluid containing a large number of vortex filaments. *Phil. Mag. S.*, 12(80):1057–1063, November 1931.
- [110] José Trueba and Antonio F. Rañada. The electromagnetic helicity. *The European Journal of Physics*, 17:141–144, 1996.
- [111] José Trueba and Antonio F. Rañada. Helicity in classical electrodynamics and its topological quantization. *Apeiron*, 7(1-2):83–88, January-April 2000.
- [112] David Turnbull. Kinetics of solidification of supercooled liquid mercury droplets. *The Journal of Chemical Physics*, 20(3):411–424, 1952. doi: 10.1063/1.1700435.

- [113] S. Webb, editor. *The Physics of Diagnostic Imaging Second Edition*. CRC Press (Institute of Physics Publishing(, 1988.
- [114] J. H. Weijs, James R. T. Seddon, and D Lohse. Diffusive shielding stabilizes bulk nanobubble clusters. *ChemPhysChem*, 13:2197–2204, 2011.
- [115] Wen-Yang Wen and John A. Muccitelli. Thermodynamics of some perfluorocarbon gases in water. *Journal of Solution Chemistry*, 8:225–246, 1979. ISSN 0095-9782. doi:10.1007/BF00648882.
- [116] G. W. Willard. Ultrasonically induced cavitation in water: a step by step process. *The journal of the acoustical society of america*, 25(4):669–686, July 1953.
- [117] Ludwig Wittgenstein. *Tractatus Logico-Philosophicus*. Routledge Classics, 2002, 1921. Translated by D.F. Pears and B.F. McGuinness.
- [118] Boguslaw Wolniewicz. *Logic and metaphysics. Studies in Wittgenstein's ontology of facts*. Warsaw: Polskie Towarzystwo Semiotyczne, 1999.
- [119] Zhanwen Xing, Jinrui Wang, Hengte Ke, Bo Zhao, Xiuli Yue, Zhifei Dai, and Jibin Liu. The fabrication of novel nanobubble ultrasound contrast agent for potential tumor imaging. *Nanotechnology*, 21(14):145607, 2010.
- [120] Jonathan S. Yedidia. An idiosyncratic journey beyond mean field theory. In D. Saad and M. Opper, editors, *Advanced Mean Field Methods - Theory and Practice*. MIT Press, 2000.
- [121] David E. Yount. Skins of varying permeability: A stabilization mechanism for gas cavitation nuclei. *The Journal of the Acoustical Society of America*, 65(6):1429–1439, 1979. doi: 10.1121/1.382930.
- [122] H.R. Zheng, S. Mukdadi, and R. Shandas. Theoretical predictions of harmonic generation from submicron ultrasound contrast agents for nonlinear biomedical ultrasound imaging. *Physics in Medicine and Biology*, 51(3):557–573, Feb 2006.